PLASMONIC METAMATERIALS FOR SENSING APPLICATIONS

Kristof LODEWIJKS

Dissertation presented in partial fulfillment of the requirements
for the degree of Doctor in Engineering

June 2012

Members of the
Examination Committee:

Prof. Dr. Ir. H. Neuckermans	KU Leuven	(Chairman)
Prof. Dr. Ir. R. Mertens	KU Leuven / imec	(Promoter)
Prof. Dr. G. Borghs	KU Leuven / imec	(Promoter)
Prof. Dr. V. Moshchalkov	KU Leuven	(Assessor)
Prof. Dr. Ir. G. Vandenbosch	KU Leuven	(Assessor)
Dr. Ir. W. Van Roy	imec	(Assessor)
Prof. Dr. Ir. L. Lagae	KU Leuven / imec	
Dr. Ir. P. Van Dorpe	KU Leuven / imec	
Prof. Dr. A. Dmitriev	Chalmers University	

In collaboration with:

imec

© 2012 Katholieke Universiteit Leuven, Groep Wetenschap en Technologie, Arenberg Doctoraatsschool, W. de Croylaan 6, 3001 Heverlee, België.

Alle rechten voorbehouden. Niets uit deze uitgave mag worden vermenigvuldigd en/of openbaar gemaakt worden door middel van druk, fotokopie, microfilm, elektronisch of op welke andere wijze ook zonder voorafgaande schriftelijke toestemming van de uitgever.

All rights reserved. No part of the publication may be reproduced in any form by print, photoprint, microfilm, electronic or any other means without written permission from the publisher.

ISBN 978-94-6018-520-5
D/2012/7515/56

For my parents

Twenty years from now
you will be more disappointed
by the things that you didn't do
than by the ones you did do.
So throw off the bowlines.
Sail away from the safe harbor.
Catch the trade winds in your sails.
Explore. Dream. Discover.

- Mark Twain -

Acknowledgements

The past 5 years have really flown by, and today I am very proud to present to you the work that *we* conducted. The work presented in this thesis is the result of the joint effort of many people, which deserve a major thank you at this point.

I started my journey at imec almost 6 years ago with a master thesis project under the supervision of Dr. Wim Van Roy and Dr. Zhen Li. I was very happy when Wim and our group leader Prof. Liesbet Lagae offered me the opportunity to conduct Ph.D. research in the functional nanosystems group. Soon after I started Dr. Pol Van Dorpe returned from his Post-Doc at Stanford University and from that day onwards he has been my guide into the exciting field of plasmonics.

I am very greatful to my Promotor Prof. Robert Mertens and Co-Promotor Gustaaf Borghs for the inspiring discussions and the invaluable advice they provided in order to keep my work on track.

At this point I would also like to thank all the jury members for their keen eye while reviewing this thesis and for their valuable comments. So thank you Prof. Herman Neuckermans, Prof. Viktor Moschalkov, Prof Guy Vandenbosch and Prof. Alexandre Dmitriev.

As I mentioned in the beginning, the work that I present to you here was realized with the help of many people in the FNS group. As we are a rather diverse and large research group with different research directions, it speaks for itself that I didn't collaborate to the same extent with all of you, but over the years, many of the nice colleagues also became good friends. Back in the old days when doing my master thesis research, I was working in the exciting field of spintronics, which gradually crumbled down over the years within FNS, but is now getting a second life in the newly founded MRAM group. A big thank you to all hard-core spintronic/magnetic colleagues: Sven, Mauricio, Celso, Reinier, Chengxun, Koen and Koen, Xavier, Jan, Zhen, Frederik, Jesse and Ruben. During my Ph.D. the focus of my project changed entirely as I entered the field of plasmonics. The initial steps into this field at imec were made by Iwijn and Pol, which triggered the blooming of a lot of plasmonic activities in our group. I truely enjoyed working in our plasmonaut team with Niels, Pieter, Jian, Chang, Dries, Sarp and Jiacky. Obviously, as I was working towards a biological sensor, we also had to focus on the interfacing with bio-molecules through surface chemistry and to this end I received a lot of help from Jef, Hilde, Karolien, and Tim and Tim. One day “bio” will work on my samples as well, don’t worry! Furthermore I would like to thank all current and former members of the FNS group for the joyfull time we had together!

A special word of thanks goes out to Koen, Paul, Pieter and Ajay, the master students that I guided through their projects as a daily supervisor, as their contributions are very significant to the work presented in this thesis.

Over the last 3 years, it was a true pleasure to be involved in a collaborative project between imec and Panasonic, which was a nice change from the more accademic work that I conducted for this Ph.D. thesis. A major thank you goes out to the panasonic residents Masahiko and Yasuaki and their Japanese colleagues with whom we all enjoyed many nice workshops.

Much of the work that we conducted couldn’t be realized without the support of the III/V-area technicians and the different people thato perform service work for us. Thank you Johan, Erwin, Peter, Steve, Kim and Stijn. I spent many enjoyable hours together with Jos Moonens who thought me all the details about e-beam lithography and who gave me the most punctual training to perform e-beam exposures. For all the administrational details I could always count on the support of Inge and Chantal at imec, and Lut at ESAT, thank you!

I am very greatful to IWT Flanders for the financial support which made this doctoral project possible.

Last but not least, I want to thank my family, for always being there whenever needed. First of all I want to thank my parents for offering me the opportunity to pursue my dreams, and to allow me to study almost endlessly. Next to my parents, I would also like to thank my grandparents, my brother and his girlfriend for their unconditional support and for being there whenever needed.

Kristof Lodewijks
June 2012

I just try to have fun, it’s about having a good time.

- Lemmy Kilmister -

Contents

Acknowledgements **i**

Abstract **v**

Samenvatting **vii**

Curriculum Vitae **ix**

Scientific contributions **xi**

List of acronyms **xv**

List of symbols **xvii**

1 Introduction **1**
- 1.1 General introduction 1
- 1.2 Thesis outline 2

2 Theoretical background **7**
- 2.1 Electromagnetic waves 7
  - 2.1.1 Basic properties 8
  - 2.1.2 Polarization states 11
  - 2.1.3 Wave propagation in different media 15
- 2.2 Plasmonics 21
  - 2.2.1 Localized and propagating surface plasmons 22
  - 2.2.2 Plasmon excitation mechanisms 25
  - 2.2.3 Tunability of plasmon resonances 27
  - 2.2.4 Phase and amplitude of plasmon resonances 30
- 2.3 Metamaterials 32
  - 2.3.1 Negative Index Materials (NIMs) 33
  - 2.3.2 Effective material parameters 38
  - 2.3.3 Plasmonic metamaterial building blocks 41
- 2.4 Plasmonic biosensors 42

2.4.1 Surface Plasmon Polariton (SPP) sensing 43
2.4.2 Localized Surface Plasmon Resonance (LSPR) sensing 44
2.4.3 Characterization of sensor performance 45
2.4.4 Surface functionalization 46
2.4.5 Other types of plasmonic biosensors 46
2.5 Spectroscopic ellipsometry 46
2.5.1 Measured quantities 47
2.5.2 Mathematical description of polarized light 49
2.5.3 Rotating analyzer/polarizer ellipsometry 55
2.5.4 Photo-Elastic Modulator (PEM) based ellipsometry 57
2.6 Electromagnetic simulations 59
2.6.1 Lumerical FDTD 59
2.6.2 Comsol multiphysics 59
2.6.3 Comparison of the two solvers 60

3 Self-assembled negative index materials 69
3.1 Introduction 69
3.2 Sample fabrication 71
3.2.1 Self-assembly samples 71
3.2.2 E-beam samples 73
3.3 Optical characterization 73
3.3.1 NSL samples 73
3.3.2 EBL samples 76
3.3.3 Simulations and effective parameter retrieval 78
3.4 Conclusions 78

4 Phase-sensitive measurements of LSPRs for improved sensing applications 83
4.1 Introduction 83
4.2 Sample fabrication 84
4.2.1 Self-assembled monolayers of PS beads 84
4.2.2 Gold nanorings 85
4.2.3 Gold nanodisks 86
4.3 Results and discussion 87
4.3.1 Optical characterization 88
4.3.2 Simulations of ellipsometric parameters 91
4.3.3 Inter-particle coupling mechanism 91
4.3.4 Refractive index sensing 93
4.4 Conclusions 95

5 The interaction of localized and propagating surface plasmons in sensing applications 101
5.1 Introduction 101
5.2 Sample fabrication 102
5.3 Results and discussion 103
5.3.1 Basic optical characterization 103
5.3.2 Phase-sensitive spectroscopic ellipsometry 111
5.3.3 Refractive index sensing 114
5.4 Conclusions 117

6 Conclusions and Outlook 121

Abstract

Metamaterials are man-made artificial materials of which the optical properties can be engineered to generate the desired response to an incident electromagnetic wave. They consist of sub-wavelength sized structures which can be thought of as the atoms in conventional materials. The collective response of a randomly or periodically ordered ensemble of such meta-atoms defines the properties of the metamaterial, which can be described in terms of effective material parameters such as the permittivity, permeability, refractive index and impedance. Here we show how these metamaterials can be exploited for sensing experiments in the visible and near-infrared wavelength ranges of the electromagnetic spectrum. The meta-atoms used in this work consist of nanostructures defined in gold and silica, which are both very stable and biocompatible materials. At the interface between nano-sized noble metal particles and dielectric media, collective oscillations of the electron cloud in the metal particles can be resonantly excited, which are known as plasmon resonances. In this work we deal with two types of plasmon resonances: localized surface plasmon resonances (LSPRs) and propagating surface plasmon polaritons (SPPs).

The investigated sample structures are manufactured by combining conventional lithography (top-down) and self-assembly based colloidal lithography (bottom-up) protocols with standard microprocessing techniques. In that way, we fabricated a self-assembled version of the widely studied double fishnet negative refractive index metamaterials and benchmarked this structure to e-beam lithography based reference structures. We proved that these self-assembled metamaterials can be produced on large scales with a small number of defects and similar performance as the reference structures.

In the second part of this work, we focused on self-assembled randomly distributed nanoparticle arrays on top of a continuous gold layer and a thin silica spacer for refractive index sensing applications. We proved that we can reduce the line widths of intrinsically broad dipole resonances in gold nanoparticle arrays by measuring both the amplitude and phase of the reflected waves in spectroscopic ellipsometry measurements. By spectrally detuning the electric dipole LSPR for P- and S-polarized waves we can pick up the transition between in- and out-of-phase oscillation of the

free electrons in the metal nanoparticles with respect to the incident wave. As a result the line width of the LSPRs is largely reduced, resulting in a major boost of the Figure-Of-Merit (FOM) for refractive index sensing which could eventually result in much lower detection limits.

In the third part of this work we optimized the plasmonic metamaterial substrates for refractive index sensing by changing from random particle distributions towards periodic arrays on top of a continuous gold layer and a thin silica spacer. We clearly observe that the effects of inhomogeneous broadening are largely reduced, giving rise to narrower line widths both in amplitude- and phase sensitive measurements, resulting in even larger values for the FOM. The grating structure allows for very efficient excitation of propagating SPP modes on the gold film below, which interact strongly with the localized modes. As we scan the angle of incidence, we clearly observe anti-crossing of the SPP and LSPR modes resulting in highly asymmetric line shapes and increased phase differences due to Fano-interference. We show that the interaction between the SPP mode and the LSPR mode can be used to increase the refractive index sensitivity of the LSPR mode dramatically, which in combination with the reduced line widths results in extremely high values for the FOM.

Samenvatting

Metamaterialen zijn artificiële materialen waarvan de optische eigenschappen ontworpen werden om de gewenste optische interactie te bekomen onder invloed van een aangelegde elektromagnetische golf. Ze bestaan uit structuren met afmetingen kleiner dan de golflengte van de inkomende golf, die we kunnen beschouwen als het equivalent van atomen in een conventioneel materiaal. De gezamelijke interactie van deze meta-atomen die periodiek of willekeurig geordend kunnen zijn definieert de eigenschappen van het metamateriaal, die beschreven kunnen worden met behulp van effectieve materiaalparameters zoals de permittiviteit, de permeabiliteit, de brekingsindex en de impedantie. In dit werk tonen wij aan hoe deze metamaterialen kunnen aangewend worden als sensoren in het zichtbare en het nabije infrarood gedeelte van het elektromagnetische spectrum. De gebruikte meta-atomen zijn opgebouw uit goud en silica, beiden zeer stabiele en bio-compatiebele materialen. Op het grensvlak tussen nano-dimensionele edelmetaal deeltjes en diëlectrica kunnen collectieve oscillaties van de elektronwolk in het metaaldeeltje aangeslagen worden, welke gekend zijn als plasmons. In deze thesis bestuderen we twee types van deze resonanties: lokale oppervlakte resonanties (in kleine edelmetaal deeltjes) en propagerende plasmon resonanties (op de interface tussen een vlakke edelmetaal film en een diëlectricum).

De bestudeerde stalen werden geproduceerd door een combinatie van conventionele lithografische processen (top-down), zelf-organisatie gebaseerde nanopartikel lithografie processen (bottom-up) en standaard micro-fabricatie processen. Op die manier realiseerden we een op zelf-organisatie gebaseerde variant van de zogenaamde “double fishnet” metamaterialen die een negatieve brekingsindex vertonen en we vergeleken dit materiaal met referentiestructuren gealiseerd via elektronen-bundel lithografie. We hebben aangetoond dat deze zelf-organisatie gebaseerde materialen op grote oppervlaktes gerealiseerd kunnen worden met een beperkt aantal defecten en een vergelijkbaar gedrag als de referentiestructuren.

In het tweede deel van deze thesis hebben we ons toegespitst op willekeurig geordende goud nanodeeltjes bovenop een continue goud film en een dunne silica tussenlaag voor brekingsindex-gebaseerde sensoren. We hebben aangetoond dat we de

lijnbreedte van intrinsiek brede dipool-resonanties kunnen verkleinen door naast de intensiteit ook de fase van de resonanties op te meten in spectroscopische ellipsometrie metingen. Door de samples onder een bepaalde hoek te belichten verschuiven de dipool resonanties spectraal ten opzichte van elkaar voor de P- en S-polarizatietoestanden, waardoor we het fase-verschil tussen in- en uit-fase oscillatie van de elektronwolk ten opzichte van de inkomende golf kunnen meten. De resulterende lijnbreedte van de lokale resonanties wordt hierdoor veel smaller, wat resulteert in een veel hogere waarde voor de kwaliteitsfactor van de resonantie en ultiem kan leiden tot een verlaging van de detectielimiet voor brekingsindex-gebaseerde sensoren.

In het derde deel van deze thesis hebben we de stalen verder geoptimaliseerd voor toepassing in brekingsindex-gebaseeerde sensoren door van willekeurig geordende structuren naar periodieke structuren over te gaan. We merken dat de effecten van inhomogene verbreding van de resonanties sterk onderdrukt zijn, waardoor smallere lijnbreedtes bekomen worden voor de intensiteit- en fase-gevoelige metingen, wat resulteert in een verhoging van de kwaliteitsfactor van de resonanties. Bovendien leent de periodieke structuur van nanodeeltjes zich als een zeer efficient diffractierooster voor het aanslaan van propagerende golven op de onderliggende goudlaag, die sterk interageren met de lokale resonanties in de nanodeeltjes. Wanneer we de invalshoek variëren merken we duidelijk anti-kruisend gedrag van de propagerende en de lokale modes, wat resulteert in zeer asymmetrische resonantiepieken en grotere faseverschillen ten gevolge van Fano-interferenties. We demonstreren dat de interactie tussen beide modes kan gebruikt worden om de gevoeligheid voor de brekingsindex van de lokale mode significant te verhogen, wat in combinatie met de smalle lijnbreedte resulteert in zeer hoge waarden voor de kwaliteitsfactor van de resonantie.

Curriculum Vitae

May 11, 1984 Born in Lommel, Belgium

2002-2004 Student at the University of Hasselt, Faculty of Physics. Received the degree of “Kandidaat in de Natuurkunde” in September 2004.

2004-2007 Student at the Eindhoven University of Technology, Faculty of Applied Physics. Received the B. Sc. degree in Applied Physics in October 2006 and the M. Sc. degree in Applied Physics in August 2007.

2007-2012 Ph.D. research at the Katholieke Universiteit Leuven, Faculty of Engineering Sciences and the Interuniversity Micro-Electronics Center (imec).

2012 Ph.D. defense: “Plasmonic Metamaterials for Sensing Applications”.

> We have a desire to keep pushing the boundaries,
> and the only thing that will limit us
> will be our own imagination
>
> - Lars Ulrich -

Scientific contributions

Journal contributions

“Self-assembled hexagonal double fishnets as negative index materials”, K. Lodewijks, N. Verellen, W. Van Roy, V. Moshchalkov, G. Borghs and P. Van Dorpe, *Applied Physics Letters* **98**, 091101 (2011)

“Boosting the Figure Of Merit of LSPR-based refractive index sensing by phase sensitive measurements”, K. Lodewijks, W. Van Roy, L. Lagae, G. Borghs and P. Van Dorpe *Nano Letters* **12**, 1655 (2012)

“Tuning the Fano resonance between localized and propagating surface plasmon resonances for refractive index sensing applications”, K. Lodewijks, W. Van Roy, L. Lagae, G. Borghs and P. Van Dorpe *in preparation* (2012)

“Fabrication and optical properties of gold semishells”, J. Ye, P. Van Dorpe, W. Van Roy, K. Lodewijks, I. De Vlaminck, G. Maes and G. Borghs, *Journal of Physical Chemistry C* **8**, 3110 (2009)

“Groove-gratings to optimize the electric field enhancement in a plasmonic nanoslit-cavity”, C. Chen, N. Verellen, K. Lodewijks, L. Lagae, G. Maes, G. Borghs and P. Van Dorpe, *Journal of Applied Physics* **108** 034319 (2010)

“Tuning plasmonic interaction between gold nanorings and a gold film for surface enhanced Raman scattering”, J. Ye, M. Shioi, K. Lodewijks, L. Lagae, T. Kawamura and P. Van Dorpe, *Applied Physics Letters* **97**, 163106 (2010)

“Plasmon line shaping using nanocrosses for high sensitivity localized surface plasmon resonance sensing”, N. Verellen, P. Van Dorpe, C. Huang, K. Lodewijks, G. Vandenbosch, L. Lagae and V. Moshchalkov, *Nano Letters* **11**, 391 (2011)

Patent applications

"Methods and Systems for Enhanced Optical Detection", P. Van Dorpe, K. Lodewijks, M. Shioi, J. Ye, *WO 2011/117260* (29/09/2011)

"A method and device for measuring a concentration of a biogenetic substance", P. Van Dorpe, K. Lodewijks, M. Shioi, *JP2012-001479* (filing date: 06/01/2012)

Conference contributions

Oral presentations

"Self-assembled hexagonal double fishnets as negative index materials", K. Lodewijks, N. Verellen, W. Van Roy, L. Lagae, G. Borghs and P. Van Dorpe, presented at *SPIE Photonics Europe 2010*, Brussels, Belgium (2010)

"Boosting the Figure of Merit of LSPR based refractive index sensing by phase sensitive measurements", K. Lodewijks, W. Van Roy, G. Borghs, L. Lagae and P. Van Dorpe, presented at *Nanoplasmonic Sensors and Spectroscopy 2011*, Gothenburg, Sweden (2011)

"Angular tuning of plasmonic inter-particle coupling probed by spectroscopic ellipsometry", K. Lodewijks, W. Van Roy, G. Borghs and P. Van Dorpe, presented at *Metamaterials 2011*, Barcelona, Spain (2011)

"Fabrication and application of gold open-nanoshells", J. Ye, P. Van Dorpe, W. Van Roy, K. Lodewijks, G. Maes and G. Borghs, presented at *Nanotech Northern Europe 2008*, Copenhagen, Denmark (2008)

"Gold open-nanoshells monolayer designed for surface-enhanced Raman spectroscopy (SERS) application", J. Ye, P. Van Dorpe, W. Van Roy, L. Lagae, U. Hiroshi, K. Lodewijks, G. Maes, G. Borghs, presented at *Cell Physiology and Biosensors* , Hasselt, Belgium (2008)

"Improving refractive index sensing by tailoring the lineshape and measuring the phase of plasmonic resonances", P. Van Dorpe, N. Verellen, K. Lodewijks, J. Ye, L. Lagae, invited presentation at *META '12, 3rd international conference on Metamaterials, photonic crystals and plasmonics*, Paris, France (2012)

Poster presentations

"Design and modeling of self-assembled hexagonal double fishnets", K. Lodewijks, P. Van Dorpe, W. Van Roy and G. Borghs, presented at *SPP4*, Amsterdam, Holland (2009)

"Sharp phase transitions in LSPR probed by spectroscopic ellipsometry", K. Lodewijks, W. Van Roy, L. Lagae, G. Borghs and P. Van Dorpe, presented at *SPIE Optics and Photonics 2010*, San Diego, California, USA (2010)

"Amplifying the figure of merit of phase sensitive refractive index sensing by coupling of propagating and localized surface plasmon resonances", K. Lodewijks, W. Van Roy, G. Borghs, P. Van Dorpe, presented at *SPIE Photonics Europe*, Brussels, Belgium (2012)

"Exciting dark resonances in plasmonic nanocross cavities for high sensitivity biosensing", N. Verellen, C. Huang, K. Lodewijks, G. Vandenbosch, V. Moshchalkov, T. Stakenborg, L. Lagae, K. Jans, P. Van Dorpe, *Nanotech Conference and Expo*, Anaheim, California, USA (2010)

"Subradiant Plasmon Modes in High Sensitivity LSPR Sensing Experiments in the Near-Infrared", N. Verellen, C. Huang, K. Lodewijks, G. Vandenbosch, L. Lagae, P. Van Dorpe, V. Moshchalkov, *SPIE Optics and Photonics 2010*, San Diego, California, USA (2010)

List of acronyms

AOTF	acousto-optical tunable filter
DFN	double fishnets
DL	detection limit
DN	double negative
EBL	electron beam (e-beam) lithography
EM	electromagnetic
FDTD	finite-difference time domain
FOM	figure of merit
IBE	ion beam etching
IC	integrated circuit
LHM	left-handed material
LSPR	localized surface plasmon resonance
MOKE	magneto optical Kerr effect
MIM	metal-insulator-metal
NA	numerical aperture
NIM	negative index material
NIR	near infrared range of the electromagnetic spectrum
NSL	nanosphere lithography
PDDA	polydiallyldimethylammonium
PEM	photo-elastic modulator
PMMA	Poly(methyl methacrylate)
PS	polystyrene
RHM	right-handed material
RIE	reactive ion etching
RIU	refractive index units
SAM	self-assembled monolayer
SEM	scanning electron microscope
SERS	surface-enhanced raman scattering
SN	single negative
SNOM	scanning near-field optical microscope

SPASER	surface plasmon amplification by stimulated emission of radiation
SPP	surface plasmon polariton
SPR	surface plasmon resonance
SRR	split-ring resonator
TE	transverse electric
TIR	total internal reflection
TM	transverse magnetic
VIS	visible range of the electromagnetic spectrum

List of symbols

B	magnetic induction
c	speed of light in vacuum
D	electric displacement
E	electric field
ϵ	electric permittivity
ϵ_0	electric permittivity of vacuum
H	magnetic field
k	wave vector
λ	wavelength
μ	magnetic permeability
μ_0	magnetic permeability of vacuum
n	refractive index
ν_g	group velocity
ν_p	phase velocity
ω	angular frequency
ω_p	plasma frequency
Z	impedance

Chapter 1

Introduction

1.1 General introduction

Over the past few decades we have witnessed a vast increase of very different technological applications that have substantially influenced our way of living. Many of those we could never even have imagined 20 years ago. The rapid advances in the scaling of integrated circuits (IC's) down to nanometer dimensions have opened up a huge opportunity window for affordable consumer electronics which are all around us nowadays. This fast technological revolution was already predicted by Richard P. Feynman in his legendary presentation "There's plenty of room at the bottom" [1] and by Gordon E. Moore who stated in his famous law that "the number of transistors that can be placed inexpensively on an integrated circuit doubles approximately every two years" [2]. Moore's law has defined the road map for the semiconductor industry and the continued scaling down of IC's for the past decades and to that respect we can state that it lies at the basis of the field of nanotechnology that has been growing exponentially since the 1980's. With ever improving performance of device processing technologies, several new research fields were born in the area of nanotechnology. One of those fairly new research fields is "plasmonics", a rapidly growing field in which surface plasmons are investigated. But first we have to ask ourselves what is a plasmon, and what is it useful for? A plasmon is the collective oscillation of free electrons, which usually occurs at the interface of (noble) metals and a dielectric medium. More formally, a plasmon is a quasiparticle which can be defined as a quantum of plasma oscillation, similar to photons being a quantum of light, or phonons being a quantum of mechanical vibration. Plasmons as such are already known for a long time, but only recent technological advances allowed people to control them at will on the nanometer scale. The improved control of plasmons opened up possibilities for many new applications in sensors, improved semiconductor devices or even optical chips. Another new research field in nanotechnology covers the study of "metamaterials", which are a special class of man-made optical materials with a tailored response to electromagnetic waves. The history of this field dates back as far as 1968, when the Russian physicist Viktor Veselago [3] theoretically described the electromagnetic response of a material with simultaneous negative values for the real part of the electric permittivity and the magnetic permeability. He pointed out that such a material would exhibit a negative refractive index. Back then this unexpected result raised a lot of skepticism, as no such material was known to exist. However, in 2000 John Pendry picked up this old concept and developed it further. Veselago already showed that such a material could be used as a flat lens, but Pendry also predicted that this lens would have non-diffraction limited resolution, resulting in the concept of “a perfect lens” [4]. This paper by Pendry really triggered the blooming of the field of metamaterials, which today covers many more electromagnetic materials for a very wide range of applications, such as optical invisibility (cloaking), polarization control and even slowing down light (transition optics).

This thesis combines the aforementioned fields of plasmonics and metamaterials, focusing on the design, fabrication and characterization of (self-assembled) plasmonic structures for (bio-) sensing applications.

1.2 Thesis outline

In **Chapter 2** the theoretical framework for all subjects dealt with in this thesis is provided. First the basic properties of electromagnetic waves are discussed, after which the fields of plasmonics and metamaterials are introduced, followed by their combined use for biosensing applications. Subsequently the principles of spectroscopic ellipsometry and the different approaches to simulate the behavior of plasmonic structures are outlined.

In **Chapter 3** a self-assembled metamaterial with a negative refractive index (NIM) is discussed. It is based on one of the most promising designs in the field and described in terms of effective material parameters. The self-assembled metamaterial is benchmarked with state-of-the art samples based on conventional e-beam lithography.

In **Chapter 4** the angle- and polarization dependent optical response of a self-assembled random array of plasmonic resonators is investigated. The phase difference between the excited plasmon resonances for both polarization states is characterized. The resulting line widths are significantly reduced compared to the intensity based measurements, resulting in much higher Figures Of Merit (FOMs) for sensing applications.

In **Chapter 5** the concepts of the previous chapter are extended into a periodic array of plasmonic resonators. As a result, the effects of inhomogeneous broadening of the local modes are suppressed, while propagating modes are excited by the grating which interfere with the localized modes. We observe anti-crossing behavior of localized and propagating modes and observe more pronounced phase differences in the regions where these modes interfere strongly. This interaction provides an additional degree of freedom to tune the properties of refractive index based sensing devices.

Bibliography

[1] R. P. Feynman, “There’s plenty of room at the bottom,” in *Annual meeting of the American Physical Society*, 1959.

[2] G. E. Moore, “Cramming more components onto integrated circuits,” *Electronics*, vol. 38, no. 8, p. 4, 1965.

[3] V. G. Veselago, “The electrodynamics of substances with simulataneously negative values of permittivitty and permeability,” *Soviet Physics Uspekhi*, vol. 10, no. 4, pp. 509–514, 1968.

[4] J. Pendry, “Negative refraction makes a perfect lens,” *Physical review letters*, vol. 85, no. 18, pp. 3966–9, 2000.

Chapter 2

Theoretical background

In this chapter the theoretical background needed for the understanding of this thesis is outlined. In the first section we start with basic properties of electromagnetic radiation, the different polarization states of an electromagnetic (EM) wave and its propagation in different media. In the second section we give a basic introduction to plasmonics and the excitation of surface plasmons using EM-waves. We also look at the phase of plasmon resonances and their different applications. In the third section we discuss plasmonic metamaterials, their description in terms of effective material parameters and their basic building blocks, focusing on negative index materials (NIMs). In the fourth section we focus on the different types of plasmonic (metamaterial) biosensors and the most important parameters to describe their performance. In the fifth section we discuss spectroscopic ellipsometry: the measured quantities, the mathematical formalism and the various measurement configurations that can be used. The sixth section provides a short introduction to the numerical simulations that are used in the remainder of this thesis.

2.1 Electromagnetic waves

EM-waves are all around us in our everyday life. Only a small fraction of the wide variety of EM-waves surrounding us is visible to our eyes, which is known as “light” or the visible part of the EM spectrum (fig 2.1). This visible part of the spectrum consists of photons (the carrier of light, or more general of EM-waves) with a wavelength between 380 and 760 nm. Photons with an arbitrary wavelength outside of this range are not visible to the human eye, but they are very important in technological applications surrounding us. Some examples include the MHz and GHz bands for our mobile phones, Radio frequencies (RF) used for radio and TV broadcasts and X-rays used for medical imaging.

This wide variety of different EM-waves originates from the same theory, their main difference is the fact that they have different wavelengths (or frequencies) and

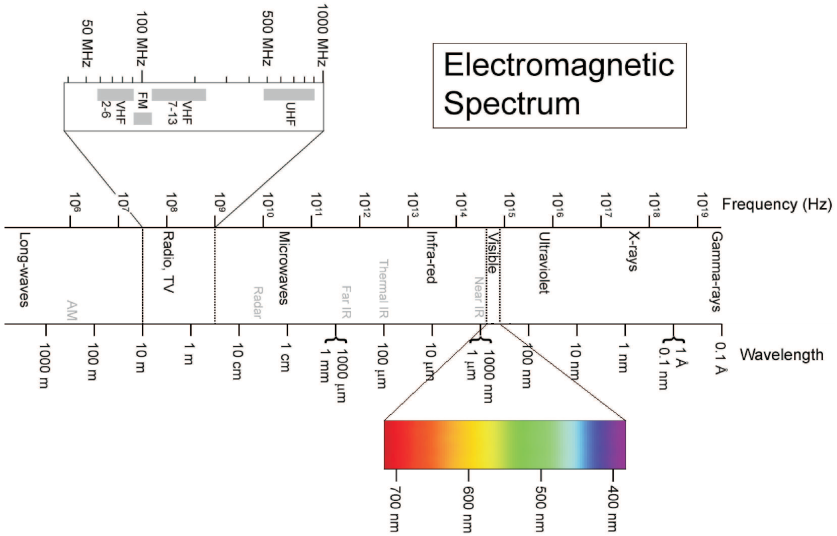
Electromagnetic Spectrum
Frequency (Hz)
10^6
10^7
10^8
10^9
10^{10}
10^{11}
10^{12}
10^{13}
10^{14}
10^{15}
10^{16}
10^{17}
10^{18}
10^{19}
50 MHz
100 MHz
500 MHz
1000 MHz
VHF 2-6
FM
VHF 7-13
UHF
Long-waves
AM
Radio, TV
Microwaves
Radar
Far IR
Thermal IR
Infra-red
Near IR
Visible
Ultraviolet
X-rays
Gamma-rays
Wavelength
1000 m
100 m
10 m
1 m
10 cm
1 cm
1000 µm
1 mm
100 µm
10 µm
1000 nm
1 µm
100 nm
10 nm
1 nm
1 Å
0.1 nm
0.1 Å
700 nm
600 nm
500 nm
400 nm

Figure 2.1: *The electromagnetic spectrum*

very different propagation properties in different media. In this thesis we will focus on visible and near infrared (NIR) EM waves for plasmonic metamaterial biosensors.

2.1.1 Basic properties

The most fundamental form of EM-waves are transverse plane waves, which can be easily derived starting from the Maxwell equations in an infinite medium in the absence of sources (2.1). Here we show the formal derivation of such waves, which are essential in the understanding of the propagation behavior for any other polarization state of an EM-wave (see section 2.1.2).

$$\begin{aligned} \nabla \cdot \mathbf{B} &= 0 \qquad & \nabla \times \mathbf{E} + \tfrac{\partial \mathbf{B}}{\partial t} &= 0 \\ \nabla \cdot \mathbf{D} &= 0 \qquad & \nabla \times \mathbf{H} - \tfrac{\partial \mathbf{D}}{\partial t} &= 0 \end{aligned} \tag{2.1}$$

If we assume solutions with a harmonic time dependence $e^{-i\omega t}$, these equations can be rewritten in order to obtain the field amplitudes.

$$\begin{aligned} \nabla \cdot \mathbf{B} &= 0 \qquad & \nabla \times \mathbf{E} - i\omega \mathbf{B} &= 0 \\ \nabla \cdot \mathbf{D} &= 0 \qquad & \nabla \times \mathbf{H} + i\omega \mathbf{D} &= 0 \end{aligned} \tag{2.2}$$

In uniform isotropic media, these expressions can be reformulated in terms of the electric permittivity ϵ and the magnetic permeability μ which describe the relationship between the electric displacement **D**, the magnetic field **H**, the electric field **E** and the magnetic induction **B** (2.3). Both ϵ and μ are in general complex valued functions of the angular frequency ω, but for now we assume that they are real and positive (i.e. no losses).

$$\mathbf{D} = \epsilon \mathbf{E} \qquad\qquad \mathbf{B} = \mu \mathbf{H} \tag{2.3}$$

Plugging equation 2.3 into 2.2 we obtain the equations for **E** and **B**

$$\nabla \times \mathbf{E} - i\omega \mathbf{B} = 0 \qquad \nabla \times \mathbf{B} + i\omega\mu\epsilon \mathbf{E} = 0 \tag{2.4}$$

By calculating the divergence of equations 2.4, we obtain the Helmholtz wave equation

$$(\nabla^2 + \mu\epsilon\omega^2) \begin{Bmatrix} \mathbf{E} \\ \mathbf{B} \end{Bmatrix} = 0 \tag{2.5}$$

If we look for plane waves propagating in the z-direction as possible solutions ($e^{ikz-i\omega t}$), we obtain the relationship between the wave number k and the frequency ω (2.6).

$$k = \sqrt{\mu\epsilon}\omega \tag{2.6}$$

This expression gives rise to the definition of the phase velocity (v) and the refractive index n, which are related by equation 2.7. The phase velocity describes how any frequency component in a wave propagates, which is determined by the refractive index, that in general is a complex function of the frequency.

$$v = \frac{\omega}{k} = \frac{1}{\sqrt{\mu\epsilon}} = \frac{c}{n} \tag{2.7}$$

The refractive index itself can therefore be described in its most general shape

$$n = n' + in'' = \sqrt{\frac{\mu}{\mu_0}\frac{\epsilon}{\epsilon_0}} \tag{2.8}$$

For a nondispersive medium (μ and ϵ independent of ω), we can rewrite the possible plane wave solutions of the Maxwell equations (2.1) in their most general shape,

$$u(z,t) = ae^{ikz-i\omega t} + be^{-ikz-i\omega t} = ae^{ik(z-vt)} + be^{-ik(z+vt)} \tag{2.9}$$

from which it is clear that we are looking at waves traveling in the positive and negative z-direction with phase velocity v. The derivations above also hold in case of dispersive materials, but in that case the shape of the propagating wave changes as it propagates. In order to formally derive the behavior of a plane wave with frequency ω and wave vector $\mathbf{k} = k\mathbf{q}$ we have to verify that the solution in equation 2.9 is a solution of equations 2.1 and 2.5. If we look at the real parts of the complex fields **E** and **B**, the solutions can be rewritten to

$$\mathbf{E}(\mathbf{r},t) = \mathbf{E_0}e^{ik\mathbf{q}\cdot\mathbf{r}-i\omega t} \qquad \mathbf{B}(\mathbf{r},t) = \mathbf{B_0}e^{ik\mathbf{q}\cdot\mathbf{r}-i\omega t} \tag{2.10}$$

in which $\mathbf{E_0}$, $\mathbf{B_0}$ and $\mathbf{q}$ are constant vectors. By plugging in these values into equation 2.5, it follows that $\mathbf{q}$ should be a unit vector, and the only thing that remains is to fix the vector parameters such that equations 2.1 are satisfied. In that way, we obtain the following conditions from the divergence equations

$$\mathbf{q}\cdot\mathbf{E_0} = 0 \qquad\qquad \mathbf{q}\cdot\mathbf{B_0} = 0 \tag{2.11}$$

which implies that **E** and **B** are both perpendicular to the propagation direction **q**. From the curl equations we can derive the other constraints that apply to **E** and **B**, which result in the following condition

$$\mathbf{B_0} = \sqrt{\mu\epsilon}\mathbf{q}\times\mathbf{E_0} = \frac{n}{c}\mathbf{q}\times\mathbf{E_0} \tag{2.12}$$

from which we can see that $c\mathbf{B}$ and **E** have the same dimensions and the same magnitude (in free space). Moreover, it is also clear that the electric and magnetic fields are perpendicular to the propagation direction and to each other. Plane waves are often expressed in terms of **E** and **H** and in that case equation 2.12 can be rewritten as follows

$$\mathbf{H_0} = \mathbf{q}\times\frac{\mathbf{E_0}}{Z} \tag{2.13}$$

with Z (equation 2.14) being the impedance of the medium.

$$Z = \sqrt{\frac{\mu}{\epsilon}} \tag{2.14}$$

In the case n is a real number, the electric and magnetic fields have the same phase and the resulting transversal plane wave propagates as illustrated in figure 2.2.

A propagating plane wave transports energy and the time-averaged energy flux can be extracted from the real part of the Poynting vector **S** (equation 2.15).

$$S = \frac{1}{2}\mathbf{E}\times\mathbf{H}^* \tag{2.15}$$

The resulting time-averaged energy density u is given by equation 2.16. Note that both electric and magnetic fields contribute to the energy flow, but that these are the same in magnitude for a homogeneous plane wave, such that we write the energy flow as function of electric fields only.

$$u = \frac{\epsilon}{2}|E_0|^2 \tag{2.16}$$

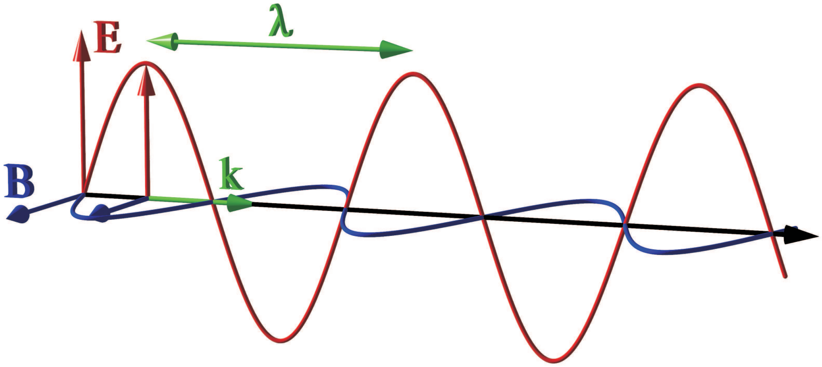

Figure 2.2: *Schematic representation of a transverse electromagnetic plane wave with wave vector* **k** *and wavelength* λ *propagating to the right.*

So far we only considered the refractive index to be real, but in its most general shape (equation 2.8), it also has an imaginary part. If we also take this into account, we are looking at inhomogeneous plane waves, which decay (positive values) or increase (negative values) in amplitude as they propagate.

2.1.2 Polarization states

In the previous section we derived the properties of a transverse plane wave, the most fundamental type of EM-wave. Now we want to take a look at other polarization states, which are a superposition of different plane wave states. We start from 2 transverse plane waves which are polarized perpendicular with respect to each other.

$$\begin{aligned} \mathbf{E_1} &= \mathcal{E}_\mathbf{1} E_{1,0} e^{i\mathbf{k}\cdot\mathbf{r}-i\omega t} & \mathbf{B_1} &= \sqrt{\mu\epsilon}\frac{\mathbf{k}\times\mathbf{E_{1,0}}}{k} \\ \mathbf{E_2} &= \mathcal{E}_\mathbf{2} E_{2,0} e^{i\mathbf{k}\cdot\mathbf{r}-i\omega t} & \mathbf{B_2} &= \sqrt{\mu\epsilon}\frac{\mathbf{k}\times\mathbf{E_{2,0}}}{k} \end{aligned} \tag{2.17}$$

A linear combination of these two plane waves with electric field direction (polarization) $\mathcal{E}_\mathbf{1}$ and $\mathcal{E}_\mathbf{2}$ and complex electric field amplitude $E_{1,0}$ and $E_{2,0}$ is the most general homogeneous plane wave propagating wave vector **k**.

$$\mathbf{E}(\mathbf{r}, t) = (\mathcal{E}_\mathbf{1} E_{1,0} + \mathcal{E}_\mathbf{2} E_{2,0}) e^{i\mathbf{k}\cdot\mathbf{r}-i\omega t} \tag{2.18}$$

The real and complex parts of the electric field amplitudes determine the polarization state of the combined EM-wave, which depends both on the magnitude and phase of the field amplitudes of the constituent waves. In the simplest case both waves are in phase, and their superposition will be a homogeneous plane wave (fig 2.3) of which the polarization angle θ (with respect to $\mathcal{E}_\mathbf{1}$) and the magitude E are given by equation 2.19.

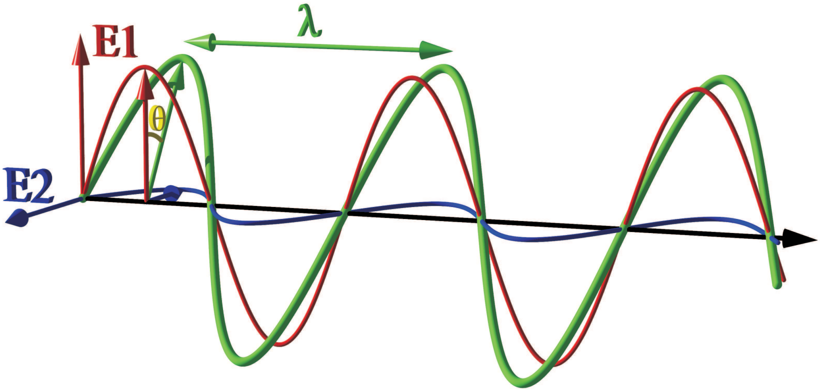

Figure 2.3: *Schematic representation of a linearly polarized wave, composed of 2 transverse electromagnetic plane waves which are in phase*

$$\theta = \arctan E_{2,0}/E_{1,0} \qquad E = \sqrt{{E_{1,0}}^2 + {E_{2,0}}^2} \tag{2.19}$$

When the two constituent plane waves are out of phase, their superposition will in general be elliptically polarized. The simplest example of such a wave consists of the superposition of two orthogonal plane waves with the same magnitude which are out of phase by $\pi/2$, which results in a circularly polarized wave (fig 2.4), of which the mathematical description is given by equation 2.20.

$$\mathbf{E}(\mathbf{r}, t) = E_0(\mathcal{E}_\mathbf{1} \pm i\mathcal{E}_\mathbf{2})e^{i\mathbf{k}\cdot\mathbf{r} - i\omega t} \tag{2.20}$$

If we define the direction of the unit vectors $\mathcal{E}_\mathbf{1}$ and $\mathcal{E}_\mathbf{2}$ to be along the directions x and y, and the propagation direction to be the z-direction, then the components of the electric fields are obtained by taking the real part of equation 2.20:

$$\mathbf{E_x}(\mathbf{r}, t) = E_0 \cos(kz - \omega t) \qquad \mathbf{E_y}(\mathbf{r}, t) = \mp E_0 \sin(kz - \omega t) \tag{2.21}$$

From this formula it is clear that at a fixed point in space, the electric field magnitude is constant and rotates at a frequency ω around the propagation direction. In case we take the upper signs in equations 2.20 and 2.21 the wave is left circularly polarized whereas for the lower signs it is right circularly polarized. These two circular polarization states can also be used as a set of basic fields in order to describe any other polarization state. The corresponding unit vectors can be written as follows:

$$\mathcal{E}_\pm = \frac{1}{\sqrt{2}}(\mathcal{E}_\mathbf{1} \pm i\mathcal{E}_\mathbf{2}) \tag{2.22}$$

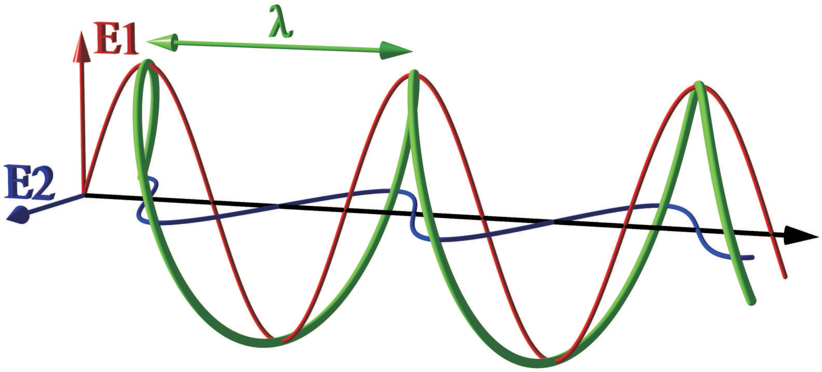

Figure 2.4: *Schematic representation of a circularly polarized wave, composed of 2 transverse electromagnetic plane waves which are out of phase by $\pi/2$*

Using these unit vectors, a homogeneous plane wave (fig 2.5) can be constructed based on equation 2.22

$$\mathbf{E}(\mathbf{r},t) = (E_{+}\mathcal{E}_{+} + E_{-}\mathcal{E}_{-})e^{i\mathbf{k}\cdot\mathbf{z}-i\omega t} \tag{2.23}$$

in which $\mathcal{E}_{+}$ and $\mathcal{E}_{-}$ are the complex amplitudes, which in this case have equal magnitudes.

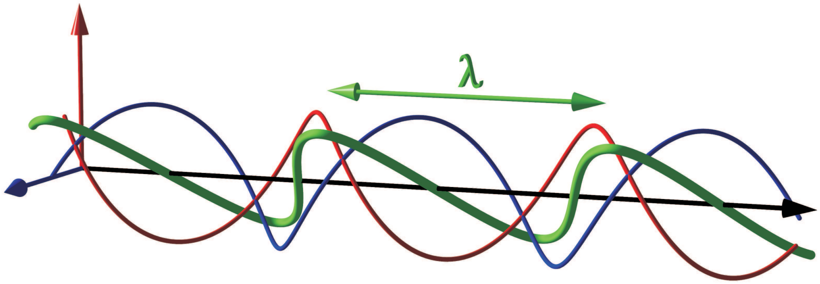

Figure 2.5: *Schematic representation of two circularly polarized waves which make up a transverse electromagnetic plane wave*

In the more general case where the magnitudes (amplitude and/or phase) of the circularly polarized waves differ, we end up with an elliptically polarized wave (fig. 2.6). The principal axes of the ellipse are given by the vectors $\mathcal{E}_{\mathbf{1}}$ and $\mathcal{E}_{\mathbf{2}}$. The ratio between the two axes is $|(1+r)/(1-r)|$ with $E_{-}/E_{+} = r$. In case there is also a phase difference between the constituent waves, which can be expressed as

$$E_-/E_+ = re^{i\alpha} \tag{2.24}$$

where the rotation angle of the main axis of the ellipse is given by $\alpha/2$.

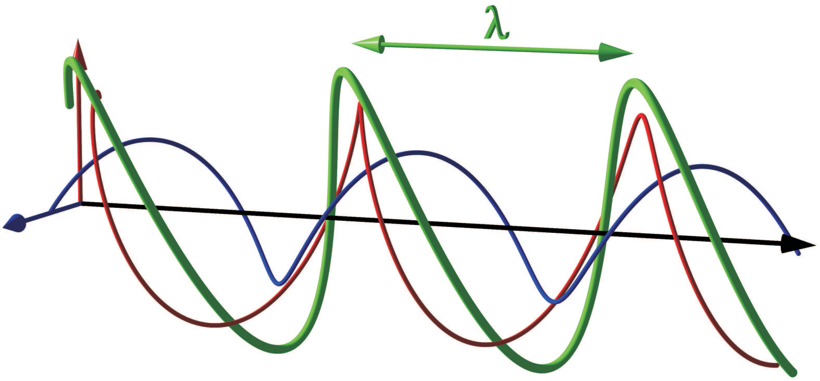

Figure 2.6: *Schematic representation of two circularly polarized waves which make up an elliptically polarized wave*

Any elliptical polarization state can also be described as a superposition of two linearly polarized waves (equation 2.17) with different magnitudes for $E_{1,0}$ and $E_{2,0}$ and a phase difference between them, as illustrated in figure 2.7.

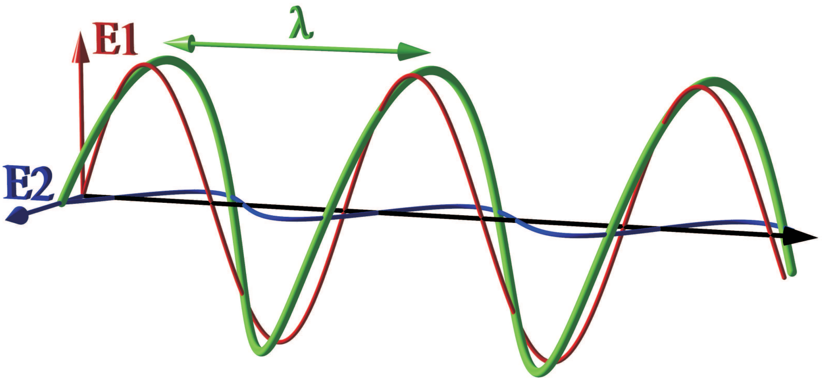

Figure 2.7: *Schematic representation of an elliptically polarized wave, composed of 2 transverse electromagnetic plane waves which are out of phase by* $\pi/4$

In section 2.5 we'll focus in some more detail on the different polarization states in the framework of spectroscopic ellipsometry.

2.1.3 Wave propagation in different media

In the previous sections we looked at the basic properties of idealized EM-waves and their mathematical description. Here we look at the propagation behavior of these waves in different media. The propagation behavior can be described entirely in terms of the electric permittivity ($\epsilon = \epsilon' + i\epsilon''$) and the magnetic permeability ($\mu = \mu' + i\mu''$), which are both complex functions of the frequency and can be related to the refractive index ($n = n' + in''$) and the impedance ($Z = Z' + iZ''$) by equations 2.8 and 2.14. All of these quantities can take a huge range of values for different materials and different frequency values. These differences are responsible for the effect of frequency dispersion: different propagation behavior of EM-waves for different frequencies. Dispersion gives rise to the splitting up of a ray of white light into its different frequency components in a prism (fig 2.8(a)) and the formation of a rainbow (fig 2.8(b)).

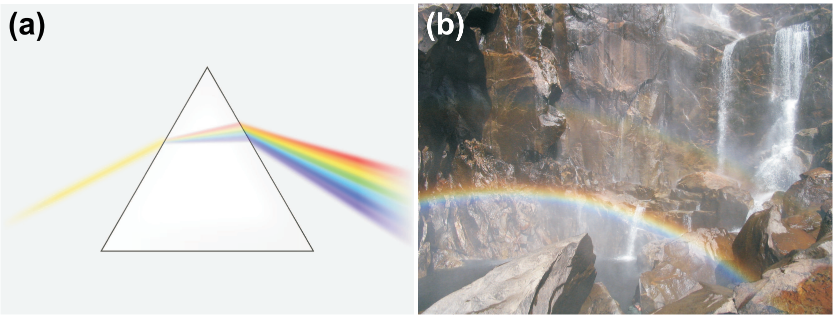

Figure 2.8: *Two examples of dispersion and refraction. (a) A beam of white light is split up into its spectral components by a prism. (b) The formation of a rainbow.*

Both phenomena originate from frequency dispersion in the refractive index. For each of the wavelengths in the visible spectrum, the refractive index of the prism and the collection of rain droplets is slightly different. At the interface between two media, the angle between the normal and the transmitted wave differs from the angle between the incident wave and the normal, according to Snell's law.

$$\frac{\sin\theta_i}{\sin\theta_r} = \frac{v_1}{v_2} = \frac{n_2}{n_1} \tag{2.25}$$

This change in the transmitted angles is known as refraction and originates from the wavelength dependence of the refractive index. In order to formally derive this behavior, we consider the polarization dependent properties of electromagnetic waves that are incident on the interface between two different media. We consider two different perpendicular polarization states of a homogeneous plane wave: one with the electric field perpendicular to the plane of incidence (fig 2.9(a)) and one with the electric field parallel to the plane of incidence (fig 2.9(b)). The former is S-polarized

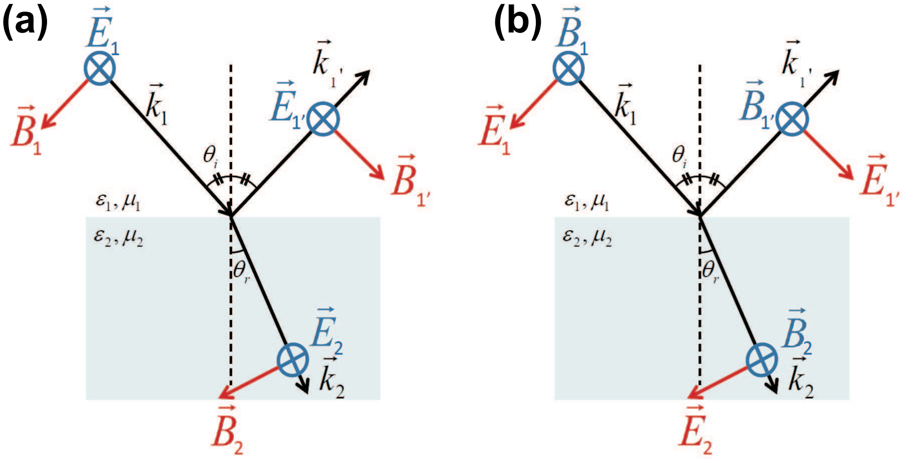
(a)
$\vec{E}_1$
$\vec{B}_1$
$\vec{k}_1$
θ_i
$\vec{k}_{1'}$
$\vec{E}_{1'}$
$\vec{B}_{1'}$
ε_1, μ_1
ε_2, μ_2
θ_r
$\vec{E}_2$
$\vec{k}_2$
$\vec{B}_2$
(b)
$\vec{B}_1$
$\vec{E}_1$
$\vec{k}_1$
θ_i
$\vec{k}_{1'}$
$\vec{B}_{1'}$
$\vec{E}_{1'}$
ε_1, μ_1
ε_2, μ_2
θ_r
$\vec{B}_2$
$\vec{k}_2$
$\vec{E}_2$

Figure 2.9: *Illustration of Snell's law and definition of S-polarized (a) and P-polarized (b) waves*

or a transverse electric (TE) wave, while the latter is P-polarized or a transverse magnetic (TM) wave.

For both polarization states the appropriate boundary conditions need to be applied in order to derive the propagation behavior of the incident wave at the interface. Three different waves are involved in this process, which depend on the material properties of both media: the incident wave (equation 2.26), the refracted wave (equation 2.27) and the reflected wave (equation 2.28).

$$\mathbf{E_1} = \mathbf{E_{1,0}} e^{i\mathbf{k_1}\cdot\mathbf{r}-i\omega t} \qquad \mathbf{B_1} = \sqrt{\mu_1\epsilon_1}\frac{\mathbf{k_1}\times\mathbf{E_1}}{k_1} \tag{2.26}$$

$$\mathbf{E_2} = \mathbf{E_{2,0}} e^{i\mathbf{k_2}\cdot\mathbf{r}-i\omega t} \qquad \mathbf{B_2} = \sqrt{\mu_2\epsilon_2}\frac{\mathbf{k_2}\times\mathbf{E_2}}{k_2} \tag{2.27}$$

$$\mathbf{E_{1'}} = \mathbf{E_{1',0}} e^{i\mathbf{k_{1'}}\cdot\mathbf{r}-i\omega t} \qquad \mathbf{B_{1'}} = \sqrt{\mu_1\epsilon_1}\frac{\mathbf{k_{1'}}\times\mathbf{E_{1'}}}{k_{1'}} \tag{2.28}$$

The magnitudes of the different wave numbers are given by

$$|\mathbf{k_1}| = |\mathbf{k_{1'}}| = k = \omega\sqrt{\mu_1\epsilon_1} \qquad |\mathbf{k_2}| = k_2 = \omega\sqrt{\mu_2\epsilon_2} \tag{2.29}$$

At the interface between medium 1 and medium 2 ($z = 0$) the boundary conditions have to be satisfied for all points. The spatial and time variation of all fields must be the same there, which implies that all phase vectors should be equal, independent of the boundary conditions.

$$(\mathbf{k_1}\cdot\mathbf{r})_{interface} = (\mathbf{k_2}\cdot\mathbf{r})_{interface} = (\mathbf{k_{1'}}\cdot\mathbf{r})_{interface} \tag{2.30}$$

From equation 2.30 it is clear that all 3 wave vectors lie in the same plane. As $k_1 = k_{1'}$, it follows that the angle between the incident and refracted wave should be equal, and we also can derive Snell's law directly.

$$k_1 \sin\theta_i = k_2 \sin\theta_r = k_{1'} \sin\theta_i \tag{2.31}$$

The boundary conditions that have to be satisfied can now be written in terms of the field values (equations 2.26-28). The normal components of **D** and **B** and the tangential components of **E** and **H** have to be continuous at the interface, which can be expressed as follows

$$\begin{gathered}
[\epsilon_1(\mathbf{E_{1,0}} + \mathbf{E_{1',0}}) - \epsilon_2\mathbf{E_{2,0}}]\cdot\mathbf{n} = 0\\
[\mathbf{k_1} \times \mathbf{E_{1,0}} + \mathbf{k_{1'}} \times \mathbf{E_{1',0}} - \mathbf{k_2} \times \mathbf{E_{2,0}}\cdot\mathbf{n} = 0\\
[\mathbf{E_{1,0}} + \mathbf{E_{1',0}} - \mathbf{E_{2,0}})] \times \mathbf{n} = 0\\
[\tfrac{1}{\mu_1}(\mathbf{k_1} \times \mathbf{E_{1,0}} + \mathbf{k_{1'}} \times \mathbf{E_{1',0}}) - \tfrac{1}{\mu_2}(\mathbf{k_2} \times \mathbf{E_{2,0}})] \times \mathbf{n} = 0
\end{gathered} \tag{2.32}$$

in which **n** is a unit vector perpendicular to the interface. From this point onwards, it is useful to split up the derivation in 2 cases for S-polarized (fig 2.9(a)) and P-polarized (fig 2.9(b)) waves, as any other polarization state can be constructed based on these two polarization states.

For the S-polarized case, the first equation from 2.32 yields no result, as the electric fields are all perpendicular to the plane of incidence. From the third and fourth equation in 2.32 we can derive equations 2.33, while the second equation in 2.32 reproduces the third when we apply Snell's law.

$$\begin{gathered}
E_{1,0} + E_{1',0} - E_{2,0} = 0\\
\sqrt{\tfrac{\epsilon_1}{\mu_1}}(E_{1,0} - E_{1',0})\cos\theta_i - \sqrt{\tfrac{\epsilon_2}{\mu_2}}(E_{2,0})\cos\theta_r = 0
\end{gathered} \tag{2.33}$$

From the obtained boundary conditions, the relative amplitudes of the refracted and reflected waves are obtained, which gives the following complex transmission and reflection coefficients:

$$\begin{aligned}
t_s &= \frac{E_{2,0}}{E_{1,0}} = \frac{2n_1\cos\theta_i}{n_1\cos\theta_i + \frac{\mu_1}{\mu_2}\sqrt{n_2{}^2 - n_1{}^2\sin^2\theta_i}}\\
r_s &= \frac{E_{1',0}}{E_{1,0}} = \frac{n_1\cos\theta_i - \frac{\mu_1}{\mu_2}\sqrt{n_2{}^2 - n_1{}^2\sin^2\theta_i}}{n_1\cos\theta_i + \frac{\mu_1}{\mu_2}\sqrt{n_2{}^2 - n_1{}^2\sin^2\theta_i}}
\end{aligned} \tag{2.34}$$

in which the square roots are introduced using Snell's law to rewrite everything as function of the properties of the incident wave.

For the P-polarized case a similar derivation can be made, for which the tangential E and H have to be continuous, which results in

$$\begin{gathered}
\cos\theta_i(E_{1,0} - E_{1',0}) - \cos\theta_r E_{2,0} = 0\\
\sqrt{\tfrac{\epsilon_1}{\mu_1}}(E_{1,0} + E_{1',0}) - \sqrt{\tfrac{\epsilon_2}{\mu_2}}(E_{2,0}) = 0
\end{gathered} \tag{2.35}$$

In this case the normal component of **D** should be continuous as well, which duplicates the second equation when we apply Snell's law. Again, we can write the relative field amplitudes as function of the properties of the incident wave, which gives the following complex transmission and reflection coefficients:

$$\begin{aligned} t_p &= \frac{E_{2,0}}{E_{1,0}} = \frac{2n_1 n_2 \cos\theta_i}{\frac{\mu_1}{\mu_2} {n_2}^2 \cos\theta_i + n_1 \sqrt{{n_2}^2 - {n_1}^2 \sin^2\theta_i}} \\ r_p &= \frac{E_{1',0}}{E_{1,0}} = \frac{\frac{\mu_1}{\mu_2} {n_2}^2 \cos\theta_i - n_1 \sqrt{{n_2}^2 - {n_1}^2 \sin^2\theta_i}}{\frac{\mu_1}{\mu_2} {n_2}^2 \cos\theta_i + n_1 \sqrt{{n_2}^2 - {n_1}^2 \sin^2\theta_i}} \end{aligned} \tag{2.36}$$

The propagation behavior of any type of EM-wave can be fully described by means of equations 2.34 and 2.36, which are often referred to as the Fresnel equations. In general the refractive index n, the electric permittivity ϵ and the magnetic permeability μ are all complex functions of the frequency. At optical frequencies in conventional materials it is often stated that $\mu_1 = \mu_2 = 1$, but as we'll show in section 2.3, this is not valid in case of optical metamaterials which also exhibit a strong magnetic response.

The electric permittivity of a material depends primarily on the electric polarizability, which is closely related to the electron density. For the plasmonic metamaterials of interest in this thesis, we restrict ourselves to dielectrics and noble metals in the visible and NIR wavelength range of the EM spectrum. In case of dielectric materials (such as silica (SiO_2)), the refractive index n and permittivity ϵ show almost no frequency dispersion and can be treated as positive real numbers (damping can be ignored). Metals show a totally different behavior, and can be described by the Drude-Sommerfeld model:

$$\epsilon_{Drude}(\omega) = \epsilon_\infty - \frac{{\omega_p}^2}{\omega^2 + i\gamma\omega} \tag{2.37}$$

in which ω_p is the plasma frequency, and γ a damping factor. The contribution of the bound electrons to the polarizability is included in ϵ_∞, which is 1 in case only the conduction band electrons contribute. This model gives a fairly good description for noble metals in the visible and NIR spectral range, although some modifications are needed at shorter wavelengths in order to compensate for inter-band transitions. Therefore in numerical calculations we use adapted models based on experimental data to obtain a more accurate description of the investigated structures. In general, the permittivity can be written as $\epsilon(\omega) = \epsilon' + i\epsilon''$. The real part is negative for frequencies below the plasma frequency and relates directly to the polarizability of the metal, while the imaginary part takes positive values and relates to the damping of propagating waves and the phase of the polarizability. An overview of the experimental values [1] of the permittivity for gold (Au), which we used in our numerical simulations is given in figure 2.10.

It is clear that also the propagation behavior of EM-waves will be influenced by the effects of dispersion. So far we only considered the propagation of idealized waves at a fixed frequency. In that case the permittivity defines the amplitude, phase

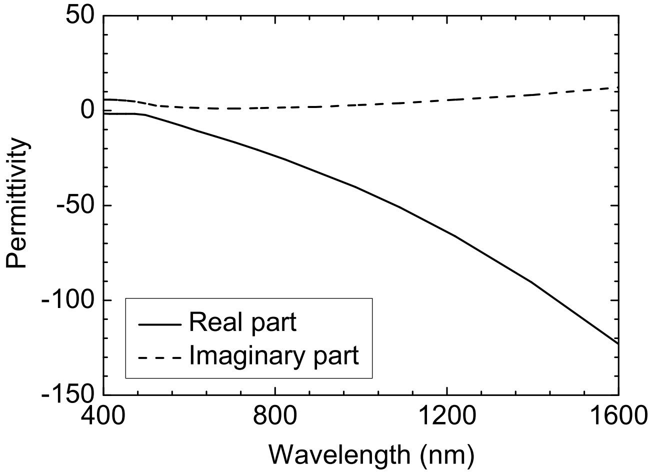

Figure 2.10: *Electric permittivity of gold [1]*

and damping of a propagating wave. In that respect, we introduced the concept of phase velocity v (equation 2.7), which defines the propagation velocity for a single frequency component. In practical applications even the most idealized source will contain more than one frequency component or wavelength, due to finite pulse durations or inherent broadening in the source. All of these frequency components propagate with slightly different phase velocities and as a consequence both the amplitudes and phases tend to show changes with respect to each other. This implies that in dispersive media the velocity of energy flow can differ largely from the phase velocity.

For dispersive media, the frequency depends on the wave vector ($\omega = \omega(k)$). In most spectral regions ω is a slowly varying function of k, but in certain spectral regions the variation is much more pronounced, for example in the vicinity of the plasma frequency of a metal. If we assume for now that k and ω are real numbers, we can write a superposition of homogeneous plane waves (equation 2.9) to construct a more general solution for a plane wave in a dispersive medium

$$u(z,t) = \frac{1}{\sqrt{2\pi}} \int_{-\infty}^{+\infty} A(k) e^{ikz - i\omega(k)t} dk \tag{2.38}$$

where $A(k)$ defines the amplitude for the different components of the superposition of plane waves. The amplitude values are obtained by the Fourier transform of the spatial amplitude $u(z,t)$ at $t = 0$

$$A(k) = \frac{1}{\sqrt{2\pi}} \int_{-\infty}^{+\infty} u(z,0) e^{-ikz} dz \tag{2.39}$$

In that way, we obtain homogeneous plane wave $u(z,t) = e^{ik_0 z - i\omega(k_0)t}$. If we consider a finite wave train $u(z,0)$ at $t = 0$ then $A(k)$ will not be a delta function but a peaked function with a finite width (determined by the length of the wave train) Δk which is centered around the wave number k_0. If we assume a fairly sharp shape of this peaked function (i.e. the wave train is rather long), then the frequency $\omega(k)$ can be expanded around k_0.

$$\omega(k) = \omega_0 + \frac{\partial \omega}{\partial k}|_0 (k - k_0) + \ldots \tag{2.40}$$

By inserting this expansion into equation 2.38, we can derive $u(z,t)$

$$u(z,t) \approx \frac{e^{i[k_0 \frac{\partial \omega}{\partial k}|_0 - \omega_0]t}}{\sqrt{2\pi}} \int_{-\infty}^{+\infty} A(k) e^{i[z - \frac{\partial \omega}{\partial k}|_0 t]k} dk \tag{2.41}$$

If we compare this with equation 2.39 then it follows that the integral in equation 2.42 describes $u(z', 0)$ with $z' = z - \frac{\partial \omega}{\partial k}|_0 t$, from which we obtain

$$u(z,t) \approx u(z - t\frac{\partial \omega}{\partial k}|_0, 0) e^{i[k_0 \frac{\partial \omega}{\partial k}|_0 - \omega_0]t} \tag{2.42}$$

This illustrates that apart from an overall phase factor, the pulse travels undistorted in shape with a group velocity v_g which can differ significantly from the (average) phase velocity v_p which was already introduced in equation 2.7.

$$v_g = \frac{\partial \omega}{\partial k}|_0 \tag{2.43}$$

As the group velocity of a pulse describes its propagation velocity, it also determines at which rate the pulse is transporting energy in the direction of the Poynting vector (equations 2.15 and 2.16). The relationship between ω and k can be written in its most general shape

$$\omega(k) = \frac{ck}{n(k)} \tag{2.44}$$

from which we obtain the general expressions for the phase velocity v_p and group velocity v_g as function of the refractive index n

$$v_p = \frac{\omega(k)}{k} = \frac{c}{n(k)} \tag{2.45}$$

$$v_g = \frac{c}{n(\omega) + \omega(\partial n / \partial \omega)} \tag{2.46}$$

In most conventional materials with normal dispersion ($(\partial n/\partial \omega) > 0$ and $n > 1$) the velocity of energy flow is smaller than the phase velocity and smaller than c.

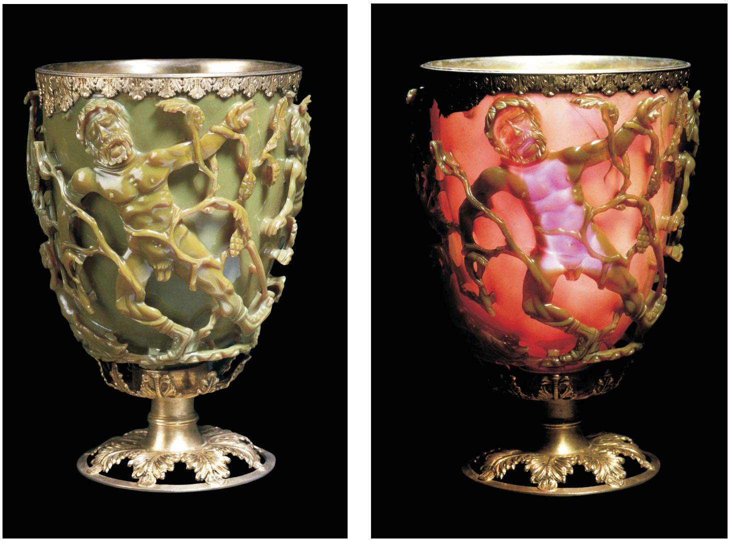

Figure 2.11: *Roman nanotechnology: the Lycurgus gup shows up green/yellow (left) when light reflects from the outer surface and red (right) when it is illuminated from the inside [5]*

In regions of anomalous dispersion, huge differences between the phase and group velocity can occur. One important example of such materials are electromagnetic metamaterials, which will be discussed in section 2.3. For a more comprehensive overview of wave propagation, the reader is referred to Jackson [2].

2.2 Plasmonics

The most famous and probably oldest example of a plasmonic material is the Lycurgus Cup (fig 2.11), which dates back to the 4^{th} century. This glass cup contains nanometer sized silver and gold clusters, in which localized plasmon resonances can be excited with visible light. When illuminated from the outside, the light reflected from the outer surface produces a green/yellow color but when it is illuminated from the inside the transmitted light produces a red color [3]. This effect has been used for many centuries in the fabrication of stained glass windows in historical buildings but it was only in the beginning of the last century that people realized that these effects could be attributed to plasmonic resonances [4].

The first experimental observation of collective electron oscillations already dates back more than one century [6], when Wood reported on Wood's anomalies: intensity drops in optical reflection spectra of metal gratings. It was only in the late 1960's that this effect could be attributed to the excitation of surface plasmons [7], the collective oscillations of free electrons in the metal. The term "plasmon" was introduced shortly before by Pines [8]. A plasmon can be defined as a quantum for the collective oscillation of free electrons, usually at the interface between (noble) metals and dielectrics. The term plasmon refers to the plasma-like behavior of the free electrons in a metal under the influence of electromagnetic radiation. Nowadays, due to ever improving nanofabrication methods, the field of plasmonics is more active than ever before.

2.2.1 Localized and propagating surface plasmons

Although the term plasmon covers any type of plasma-like oscillation of free electrons, we can distinguish between a few different types. The different types of plasmons that can be excited in metallic objects depend on their dimensions. In large three-dimensional metal structures volume plasmons can exist in the bulk of the metal. At the interface between metals and dielectrics propagating surface plasmon polaritons (SPPs) can be excited. Low-dimensional metal structures such as nanoparticles support a wide variety of localized surface plasmon resonances (LSPRs).

Volume plasmons

Volume plasmons are the most fundamental and intrinsic type of plasmon resonance that can be supported by a metal. These resonances occur at the plasma frequency of metals ω_p, which are transparent to radiation with higher frequencies and non-transparent to radiation with lower frequencies. The plasma frequency primarily depends on the electron density:

$$\omega_p^2 = \frac{Ne^2}{m\epsilon_0} \tag{2.47}$$

in which N is the conduction electron density, e the electron charge, m the effective optical mass of the electron and ϵ_0 the permittivity of free space. These volume plasmons are longitudinal modes which cannot be excited by an incident photon, but only by particle impact [9].

Surface Plasmon Polaritons (SPPs)

At the interface between a metal and a dielectric, propagating solutions of Maxwell's equations (2.1) exist, which are so-called surface plasmon polaritons (SPPs). These collective oscillations of the free electrons in the metal make up dispersive longitudinal waves that propagate along the interface and decay exponentially into both media (fig 2.12 (a and b)) with typical decay lengths of a few tens of nanometers in the metal and up to several hundreds of nanometers in the dielectric (depending on the resonant wavelength). The propagating solutions travel with an in-plane wave vector k_{spp} (equation 2.49) which defines the dispersion relation in figure 2.12 (c)

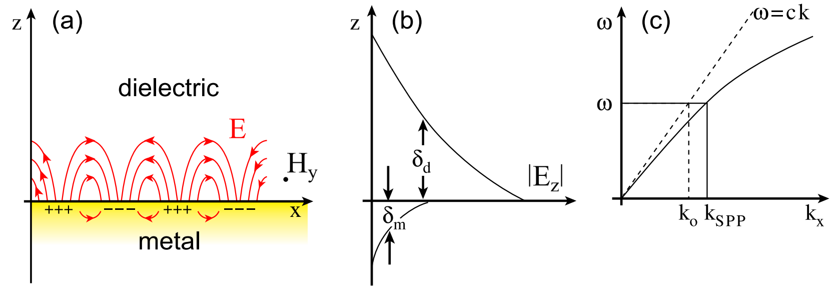

Figure 2.12: *Propagating surface plasmon polaritons (SPPs). (a) Charge density oscillations at the metal/dielectric interface with the associated EM fields. (b) The different decay lengths of the evanescent field component in the dielectric and metal, depending on the skin depth. (c) The dispersion relation of an SPP, illustrating its subwavelength confinement and the momentum mismatch that has to be overcome in order to excite them.*

$$k_{spp}(\omega) = \frac{\omega}{c}\sqrt{\frac{\epsilon_d \epsilon_m}{\epsilon_d + \epsilon_m}} \tag{2.48}$$

in which ϵ_m and ϵ_d are the permittivity of the metal and dielectric medium [9]. Clearly the dispersion relation lies to the right of the light line in free space ω/c, which implies that this SPP mode cannot directly be excited by an incident photon. Only when the dispersion relation of the incident wave and the propagating SPP mode coincide, an incident photon can excite the SPP mode. To do so, several coupling mechanisms can be applied, as described in the next section.

Localized Surface Plasmon Resonances

Localized surface plasmon resonances (LSPRs) are the non-propagating counterpart of SPPs, which can be excited in nanometer-sized subwavelength metallic particles. The free electron cloud of the nanostructure can be resonantly excited by EM fields due to enhanced polarizabilities of the particles at certain frequencies. These enhanced polarizabilities give rise to strongly enhanced near fields close to the metal surface, which are often referred to as hot spots.

The simplest structure in which LSPRs can be excited, and for which analytical solutions of Maxwell's equations can be obtained is a metallic sphere which was already treated by Mie in 1908 [4]. This example is very instructional in order to understand more complex structures, so therefore we will describe the case of the dipolar plasmon resonance in a metal sphere with a radius a much smaller than the wavelength of the incident field ($a \ll \lambda$). This allows us to treat this case in the *quasistatic approximation*: the electric field over the nanoparticle can be assumed to be constant, while the wavelength dependence of the permittivity of the metal ϵ_m and

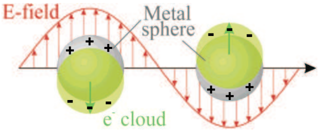

Figure 2.13: *Illustration of the dipole polarizability of a spherical metal nanoparticle under the influence of a plane wave*

the surrounding medium ϵ_s is taken into account. To solve this problem, we have to look for solutions of the Laplace equation

$$\nabla^2\Phi = 0 \tag{2.49}$$

from which the electric field can be calculated by

$$\mathbf{E} = -\nabla\Phi \tag{2.50}$$

The boundary conditions at the interface between the sphere and the surroundings require that both the tangential component of the electric field and the normal component of the displacement are continuous. The obtained solution for the electric field consists of a superposition of the applied field $\mathbf{E_0}$ and an ideal electric dipole located at the center of the sphere with dipole moment

$$p = \epsilon_0\epsilon_s\alpha E_0 \tag{2.51}$$

where α is the complex polarizability of the metal particle [2, 9]:

$$\alpha = 4\pi a^3 \frac{\epsilon_m - \epsilon_s}{\epsilon_m + 2\epsilon_s} \tag{2.52}$$

From the shape of the denominator, one can see immediately that a resonant behavior in the polarizability is expected when $|\epsilon_m + 2\epsilon_s|$ reaches a minimum. For (noble) metals at optical frequencies (e.g gold, fig 2.10), the real part of the permittivity is negative, from which the Frölich resonance condition is obtained [9]:

$$\epsilon_m'(\lambda) = -2\epsilon_s \tag{2.53}$$

When this condition is satisfied, the dipolar LSPR mode in the nanoparticle will be resonantly excited. The damping of the plasmon resonance depends on the magnitude of the imaginary permittivity, which is reflected in the value of α. For this simple approximation in the quasistatic limit, the resonance position is independent of the size of the metal sphere, which is not generally true (see section 2.4). An other important property of plasmon resonances is reflected in the Frölich resonance condition: the dependence of the resonance position on the dielectric properties of the surroundings. When the dielectric constant ϵ_s of the surroundings (and thus the refractive index n_s) increases, the resonance position shows a red shift. This principle is often applied in biochemical LSPR based sensors. On top of that, at the plasmon resonance there will be a tremendous near-field enhancement of the incident wave, dipole radiation of the excited dipole and increased scattering and absorption in the nanoparticle.

For larger and more complex nanoparticles, the quasistatic limit is not valid any more. For example, in larger structures also higher order modes (quadrupole, octopole, hexadecapole...) can be excited, given that the appropriate conditions are satisfied. These modes typically show much smaller line widths and much smaller scattering cross sections due to a largely reduced (or zero for symmetric particles) net dipole moment. We'll discuss the excitation and tunability of some of these modes in the next sections.

2.2.2 Plasmon excitation mechanisms

It was already pointed out in the previous sections that certain conditions apply to the possibility to excite plasmonic modes with EM fields. The excitation mechanisms are quite diverse for SPPs and LSPRs and largely depend on the geometry and sizes of the plasmonic (nano-) structures and the polarization state of the incident wave.

Surface Plasmon Polaritons

From equation 2.49 and figure 2.12 it is clear that the dispersion relation of SPPs lies to the right of the light line of the dielectric, which implies that direct coupling to an incident wave is not possible. In order to excite SPPs on a metal film, the dispersion relation of the incident photon and the SPP should coincide, such that the quasi momentum $\hbar k$ and the energy $\hbar\omega$ are conserved, a condition which can only be fulfilled for incident waves with P-polarization. The matching of the dispersion relations can be achieved in different ways. In order to bridge the momentum gap 3 methods are used commonly: prism coupling by evanescent waves, diffraction grating coupling and coupling by surface corrugations (fig 2.14). Next to those, it is also possible to use focused high-energy beams or near-field coupling using a scanning near-field optical microscope (SNOM) tip. A more comprehensive overview can be found in references [9, 10].

In order to be able to excite propagating SPPs it is necessary to obtain phase matching between the in-plane wave vector of the incident wave along the interface and the wave vector of the propagating SPP (equation 2.49). We consider an interface between air and a metal surface, for which the in-plane component along the interface is determined by the incident angle θ with respect to the surface normal:

$$k_x = k \sin\theta \tag{2.54}$$

If we consider a prism coupled to the system described above, the two most commonly used excitation mechanisms are the Kretschmann (fig 2.14(a)) [11] and

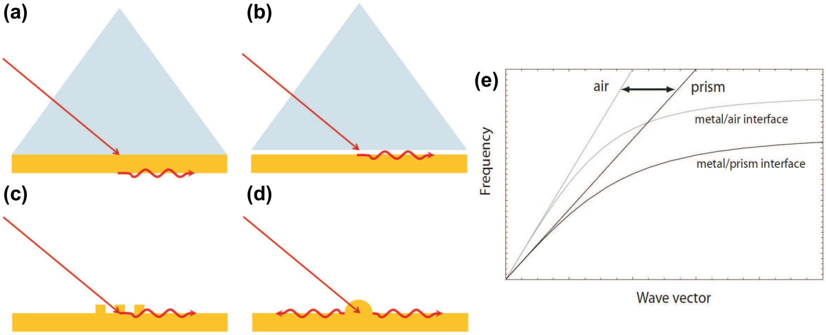

Figure 2.14: *Different coupling mechanisms for SPPs. (a) Kretschmann configuration. (b) Otto configuration. (c) Grating excitation. (d) Scattering by surface roughness. (e) Dispersion relations for excitation of plasmons at the air/metal interface by means of prism coupling.*

Otto (fig 2.14(b)) [12] configurations. By directing the incident wave through a prism with a higher dielectric constant ϵ_p, the wave vector along the interface is modified to

$$k_x = k\sqrt{\epsilon_p}\sin\theta \tag{2.55}$$

which allows to couple to plasmons at the metal/air interface. In this way, SPPs can be excited with wave vectors in between the free space light line and the prisms dispersion relation (fig 2.14(e)). Note that the direct coupling to plasmons at the prism/metal interface can not be achieved in this way. The coupling is based on total internal reflection (TIR) at the prism interface, which results in tunneling of the evanescent fields, that can couple to propagating modes at the metal/air interface. The Kretschmann [11] configuration is used most often, and in that case a thin metal layer is deposited on top of the prism, and the beam is incident with an angle larger than the critical angle, such that TIR occurs at the prism/metal interface. The evanescent fields of the TIR-wave tunnel through the metal layer and excite propagating SPPs at the metal/air interface. The Otto [12] configuration is fairly similar, but in this case there is a small air gap between the metal layer and the prism, and the evanescent field of the TIR-wave tunnels through this air gap in order to excite an SPP mode at the air/metal interface. In practical applications, the reflected signals are monitored and show a minimum in the signal at the angle/wavelength where SPP excitation occurs (see section 2.4.1).

If a grating structure is present on (a part of) the metal film (fig 2.14(c)), diffraction effects can be used to couple efficiently to propagating SPPs. In this case, the period of the grating a determines the magnitude of the reciprocal vector of the grating g:

$$g = \frac{2\pi}{a} \tag{2.56}$$

Wave matching between the incident wave and the excited SPPs can than be achieved when the following condition is fulfilled

$$k_{SPP} = k \sin\theta \pm \nu g \tag{2.57}$$

in which ν is an integer number. This general formula can be applied for any type of diffraction grating structure which is defined in or on top of the metal film. These can include many different features such as stripes, slits, dots, holes etc. In practical applications, the excitation of SPPs results in a (narrow) minimum in the intensity of the reflected light. Grating structures can be applied for the reverse process as well, in order to couple out SPPs into free space again.

Figure 2.14(d) illustrates the excitation of SPPs by means of surface corrugations, which can occur unintentionally due to undesired effects in sample fabrication, such as surface roughness and particle contamination. Alternatively, surface corrugations can be used as a controlled means of SPP excitation, for example by defining a structure which allows for excitation of LSPRs, which can also couple to propagating SPP waves on the metal film.

Localized Surface Plasmon Resonances

In the previous section, we already showed how the dipolar plasmon resonance can be excited in small nanoparticles based on the *quasistatic approximation*. Although this model is very instructional for plasmon resonances in general, it doesn't tell the full story. If we consider an asymmetric nanoparticle such as a nanodisk with radius a, and we assume that $a = \lambda/4$, then the approximation of a uniform field over the volume of the particle is no longer generally valid. Therefore we consider two different polarization states of EM-waves propagating along two of the symmetry axes of the nanoparticle. For a plane wave that propagates perpendicular to the plane of the disk (fig 2.15(a)) it is only possible to excite a dipole resonance of which the dipole moment is aligned with the polarization vector of the incident wave. For a plane wave propagating in the plane of the disk with the polarization in the plane of the disk we can couple to the quadrupole (fig 2.15(b)) and the dipole mode of the disk.

2.2.3 Tunability of plasmon resonances

Plasmon resonances can be tuned in many different ways, depending on the intended application. As the excitation mechanisms for the different sorts of plasmon resonances differ, we also treat them separately in the next sections.

Surface plasmon polaritons

SPP modes are propagating modes at the interface between a metal and a dielectric, and therefore they can be considered as modes propagating on a waveguide (in this

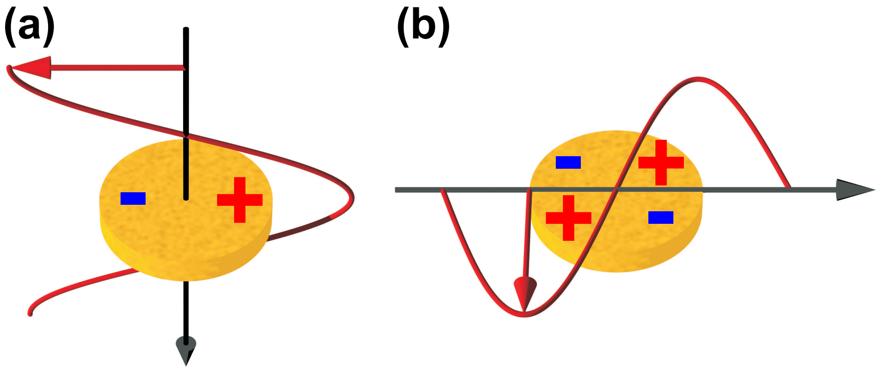

Figure 2.15: *Illustration of the effect of retardation for different polarization states in a disk particle with radius $a = \lambda/4$. (a) A plane wave propagating perpendicular to the plane of the disk can only excite a dipole resonance. (b) A plane wave propagating in the plane of the disk with the polarization direction in the plane of the disk can couple to the quadrupole mode in the disk.*

case the metal/dielectric interface) [13]. Depending on the waveguide design, we can distinguish between long-range SPP waveguides [14] (propagation distances of a few tens of microns in the VIS up to hundreds of microns in the NIR) and short-range SPP waveguides [15] (propagation distances limited to tens of microns). The former typically show very low confinement and small damping, while the latter show very high confinement but strong damping. The properties of propagating SPPs depend strongly on the waveguide design and are determined by the dispersion relations of the materials used and their thicknesses. The propagation behavior can be characterized by the *mode index* n_{eff} of the waveguide, which defines the degree of confinement and the wave vector of the SPP:

$$k_{spp}(\omega) = \frac{\omega}{c}\sqrt{\frac{\epsilon_d \epsilon_m}{\epsilon_d + \epsilon_m}} = \frac{\omega}{c} n_{eff} \tag{2.58}$$

Clearly, the propagation behavior and mode index depend strongly on the permittivity of both the dielectric and the metal, and the propagation of SPPs for the overall system can be described using the effective mode index n_{eff}. As most dielectric materials show little or no damping, the propagation behavior is mainly dominated by the properties of the metal layer(s). Typical examples of long-range SPP waveguides are Insulator-Metal-Insulator waveguides in which the metal layer is thinner than the skin depth, resulting in very low confined modes with very long propagation distances [14]. The aforementioned example of the Kretschmann [11] configuration for SPP coupling also falls in the same class of waveguided modes. Typical examples of short-range SPP waveguides are Metal-Insulator-Metal (MIM) waveguides in which

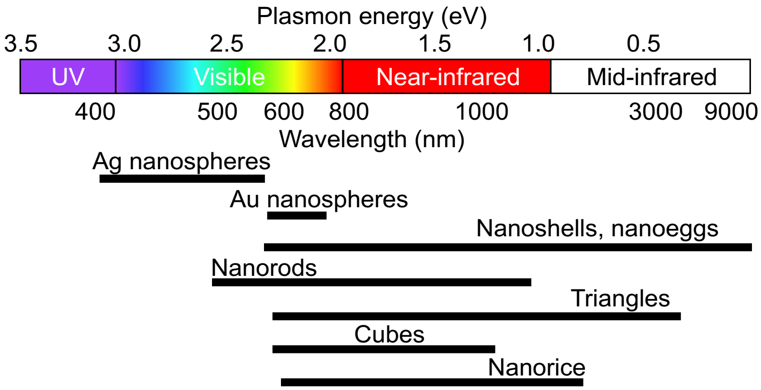

Figure 2.16: *The tunability of LSPRs by playing with particle material, size, and shape [13].*

the metal thickness is larger than the skin depth, resulting in highly confined modes with shorter propagation distances [15].

Localized surface plasmon resonances

Localized surface plasmon resonances are highly tunable and allow to confine light down to deep sub-wavelength dimensions. With increasing dimensions of the nanoparticle, most plasmon resonances show a red shift. The shape of nanoparticles is an important design parameter which allows to favor the excitation of specific plasmonic modes. Plasmon resonances are also highly sensitive to the material properties of the metal and the surrounding dielectric medium. By playing with nanoparticle size, shape, material and the surrounding medium, localized surface plasmon resonances can be tuned from the ultraviolet part of the spectrum up to the NIR as illustrated in figure 2.16 [13].

Interactions between localized surface plasmon resonances

Next to the structural properties of the nanoparticles themselves, the LSPR wavelength also depends on the interactions with plasmon resonances in neighboring particles. These interactions can be devided into two sorts: near field coupling for particles which are separated by a distance smaller than the wavelength of the incident light and far field coupling for particles that are separated by distances larger than the wavelength of the incident light. The spectral shifts that are introduced due to these coupling phenomena depend mainly on phase coherence between the local mode in one particle and the scattered fields due to modes in the neighboring particles. In case of near-field coupling, the particles can be considered as simple point dipoles and longitudinal coupling results in a red-shifted resonance, while transverse coupling

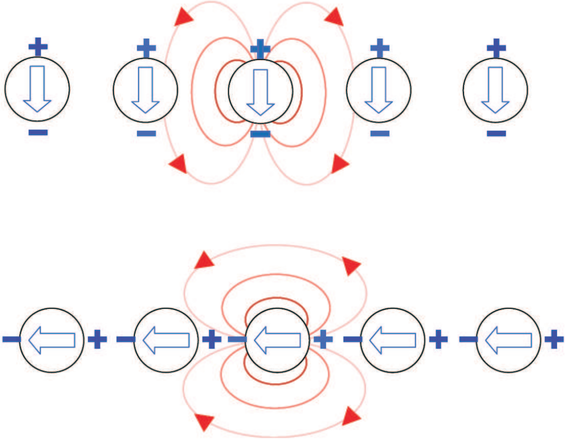

Figure 2.17: *Near-field coupling of electric dipoles in linear arrays of nanoparticles with transversal (top) or longitudinal (bottom) coupling [9,16].*

results in a blue shifted resonance [16]. For longitudinal coupling, the scattered fields of the neighboring particles oppose the local resonance and decrease its energy, while in the transversal case, the scattered fields of the neighboring particles enhance the local resonance and increase its energy.

For nanoparticles that are spaced further apart, also far-field coupling should be taken into account. In that case, the length scale on which the interactions contribute ranges up to several microns, and with increasing inter-particle spacing the plasmon resonance position and its line width show an oscillating behavior for both polarization states [17].

2.2.4 Phase and amplitude of plasmon resonances

If we consider a simple mechanical system such as a pendulum, it will oscillate at its eigenfrequency when it is moved from its equilibrium position and released to move freely. If we consider the same pendulum and drive it with a harmonic force of which we scan the frequency, we observe that at the eigenfrequency of the pendulum the amplitude of the oscillation will be maximized. Moreover, if we measure the phase difference between the applied force and the oscillating pendulum, we observe a pronounced phase difference (approaching 180^o) between in- and out-of-phase oscillation around the eigenfrequency of the system. The eigenfrequency of the system depends on the geometrical properties of the pendulum, similar to how the properties of (propagating or localized) plasmons depend on the size, shape and the material in which they are excited. In case of plasmon resonances a similar effect can be observed, where the driving force is the oscillating electric field of the incident EM

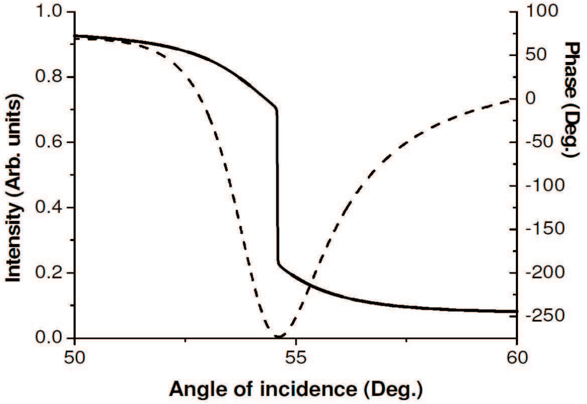

Figure 2.18: *Comparison of amplitude and phase signals for an SPR experiment [18].*

wave, which triggers the oscillation of the free electrons on the metal surface. If the wavelength of the incident wave is scanned across the plasmon resonance wavelength, the electron cloud also makes the transition from in- to out-of-phase oscillation with respect to the incident wave, which can be experimentally observed.

Surface plasmon polaritons

In the field of SPP-based sensing, substantial efforts have been made in order to measure the phase of propagating plasmons. The basic approach is to use a combination of P- and S-polarized waves for the excitation, and to measure the phase difference between the reflected waves using lock-in measurements [18]. The P-polarized wave can couple to a propagating SPP mode very efficiently, while the S-polarized wave is reflected without picking up any substantial phase change. In that way, the transition between in and out-of-phase oscillation of the free electron cloud could be experimentally observed. The phase difference shows a much smaller spectral/angular footprint compared to the intensity based signals, as illustrated in figure 2.18.

Localized surface plasmon resonances

For localized surface plasmon resonances, similar observations were made in recent years [19], inspired by earlier work in SPR-based sensing. For periodic arrays of gold nanoparticles, the amplitude and phase based reflection signals were recorded near the LSPR modes, which show a pronounced phase difference over the center wavelength of the plasmon resonance. In chapters 4 and 5 we investigate the amplitude and phase behavior of both localized and propagating surface plasmon resonances for sensing applications in more detail.

Phase interference of localized surface plasmon resonances

Next to the phase behavior of individual plasmon resonances, it is also interesting to look at the interference between different localized modes which show spectral overlap. In that way it is possible to obtain coupling between bright dipolar modes and dark higher order modes, which allows to tune plasmon resonances at a higher level. Dark higher order modes typically have large quality factors, but are complex to excite, while bright dipolar modes have small quality factors and are easy to excite. When different nanoparticles are brought close together, it is possible to achieve interference between the plasmon modes in the individual cavities. In that way, by appropriate design the bright modes can be used to excite the dark modes, which gives rise to very interesting phenomena such as Fano-interference and subradiance [20–22], which allows to tune the plasmon line shapes.

2.3 Metamaterials

The term metamaterial was introduced in 1999 by Rodger M. Walser of the University of Texas (Austin). He defined metamaterials as "*macroscopic composites having a manmade, three-dimensional, periodic cellular architecture designed to produce an optimized combination, not available in nature, of two or more responses to specific excitation*". By now, this definition is a bit outdated, as the field of metamaterials has evolved tremendously over the past decade. A better definition would be "*Manmade artificial materials with a response not readily available in nature which gain their properties from their structural composition rather than their atomic composition*". In that sense, any engineered structure such as an IC could be considered as a metamaterial, but usually the term refers to "optical metamaterials" which are artificial materials with an engineered response to EM-waves. This artificial response is obtained from the sub-wavelength sized building blocks or metamaterial atoms, which can be ordered randomly or in a periodic fashion, in order to obtain the desired effective medium response of the metamaterial.

The birth of the field of metamaterials dates back to a seminal paper by Victor Veselago [23] from 1968 in which the electromagnetic response of a material with simultaneously negative values for the electric permittivity ϵ and the magnetic permeability μ was described theoretically. Veselago pointed out that such a material would have a negative refractive index n, and therefore a flat slab of such a material would act as a lens. As such a material was not known to exist at the time, the concept raised a lot of skepticism, until it was picked up in 2000 by John Pendry [24] who pointed out that the flat lens proposed by Victor Veselago would also have non-diffraction-limited resolution. Around the same time the first negative index material (NIM) for microwave frequencies was demonstrated [25], which soon would lead to many new designs that would allow to obtain NIMs for frequencies up to the visible range.

2.3.1 Negative Index Materials (NIMs)

In this section the theoretical description for NIMs is given based on the Veselago [23] and Pendry [24] papers. The electric permittivity ϵ and the magnetic permeability μ are assumed to be purely real and negative numbers. For the theoretical description of such a material we start from the constitutive Maxwell equations

$$\begin{aligned} \mathbf{D} &= \epsilon\mathbf{E} & \qquad \nabla\times\mathbf{E} &= -\frac{\partial\mathbf{B}}{\partial t} \\ \mathbf{B} &= \mu\mathbf{H} & \qquad \nabla\times\mathbf{B} &= \frac{\partial\mathbf{D}}{\partial t} \end{aligned} \tag{2.59}$$

We consider a homogeneous plane wave which propagates in an isotropic slab of material with $\epsilon_r = \mu_r = -1$ (here ϵ_r and μ_r are the relative permittivity and permeability with respect to the vacuum values, such that $\epsilon = \epsilon_0\epsilon_r$ and $\mu = \mu_0\mu_r$) for which the propagation behavior is described by

$$k^2 = \frac{\omega^2}{c^2}n^2 \tag{2.60}$$

with $n^2 = \epsilon_r\mu_r$. We consider a plane wave propagating in the positive z-direction so the field amplitudes show a $e^{i(kz-\omega t)}$-dependence. By substitution into equations 2.60, these are reduced to

$$k\times\mathbf{E} = \omega\mu_0\mu_r\mathbf{H} \qquad k\times\mathbf{H} = -\omega\epsilon_0\epsilon_r\mathbf{E} \tag{2.61}$$

From these equations we can see that a simultaneous change of the sign of ϵ_r and μ_r changes nothing to this generalized solution of Maxwell's equations. Moreover it shows that for negative values of ϵ_r and μ_r, the triplet of vectors **k**, **E** and **H** form a left-handed system of reference, which is why Veselago named these materials left-handed materials (LHM). From the definition of the refractive index $n^2 = \epsilon_r\mu_r$ we see that there are two possible choices for the sign of n, and the correct solution is dictated by causality. If we assume that a plane wave is propagating in the positive z-direction in a lossy LHM, then the complex values of the permittivity and permeability can be written as

$$\epsilon_r = |\epsilon_r|e^{i\alpha} \qquad \mu_r = |\mu_r|e^{i\beta} \tag{2.62}$$

while the refractive index in given by $n = \sqrt{|\epsilon_r\mu_r|}e^{i\gamma}$ where γ can take the value $(\alpha+\beta)/2$ or $(\alpha+\beta)/2+\pi$. As we consider a plane wave propagating in a lossy LHM, the wave should decay in the positive z-direction. This can only be achieved when $Im(n) > 0$, which fixes the choice of the sign for $Re(n)$ to be negative, as illustrated in figure 2.19.

The direction of the energy flow in a LHM is given by the Poynting vector **S** (equation 2.15). Due to the presence of the vector product of **E** and **B**, the Poynting

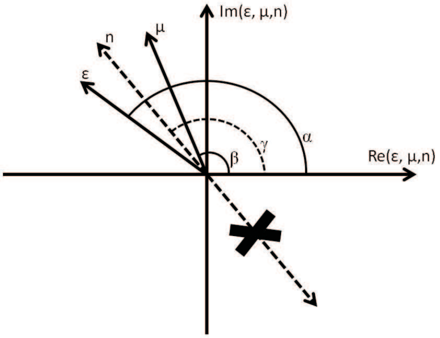

Figure 2.19: *Choice of the appropriate sign of the refractive index for a LHM in the complex plane. Given the lossy nature of the material, the wave should decay as it propagates, which implies that Im(n) > 0 and fixes the choice for Re(n).*

vector **S** and the wave vector **k** are aligned anti-parallel, contrary to conventional right-handed materials (RHM). As a consequence, in a LHM the phase velocity v_p (equation 2.46) is aligned anti-parallel to the energy flow and to the group velocity v_g (equation 2.47). This implies that the direction of the energy flow in LHM and RHM is the same, but the wave fronts travel in opposite directions.

The propagation behavior of EM-waves in LHMs discussed above was allready descibed by Veselago in 1968 [23], but in 2000 Pendry [24] pointed out that a NIM can also cancel out the exponential decay in amplitude of evanescent waves, allowing to use it as a perfect lens. We consider a slab of LHM in vacuum with thickness d and permittivity $\epsilon_r = -1$ and permeability $\mu_r = -1$ (figure 2.21) and derive the propagation behavior for a S-polarized evanescent wave travelling in the positive (+) z-direction. The incident wave can be descibed as follows

$$E_{0,+} = E_{y,0}e^{ik_z z + ik_x x - i\omega t} \tag{2.63}$$

with $k_z = i\sqrt{k_x^2 + k_y^2 - \omega^2 c^{-2}}$ and $\omega^2/c^2 < k_x^2 + k_y^2$ such that the wave decays exponentially in the propagation direction. At the first interface between the LHM and the surroundings, part of the light will be reflected ($E_{0,-}$), and part of the light will be transmitted ($E_{1,+}$)

$$E_{0,-} = r_s E_{y,0}e^{-ik_z z + ik_x x - i\omega t} \tag{2.64}$$

$$E_{1,+} = t_s E_{y,0}e^{ik_z' z + ik_x x - i\omega t} \tag{2.65}$$

where the choice of $k_z' = i\sqrt{k_x^2 + k_y^2 - \epsilon\mu\omega^2/c^2}$ and $\epsilon\mu\omega^2/c^2 < k_x^2 + k_y^2$ is defined by causality as the wave should decay as it propagates away from the source. The

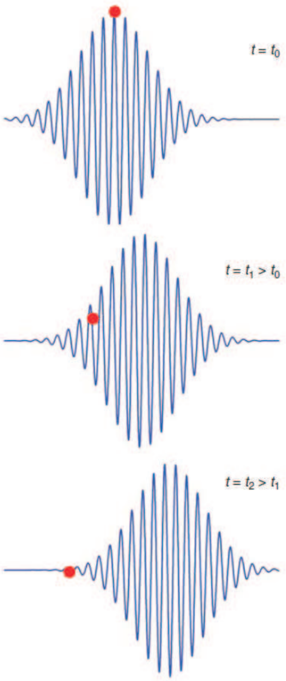

Figure 2.20: *Illustration of phase and group velocity for a wave packet traveling in a LHM. While the pulse and energy propagate to the right, the wavefronts (indicated by a red dot) propagate in the opposite direction.*

transmission and reflection coefficients at the interfaces are given by the Fresnel equations (equations 2.34 and 2.36), which for the S-polarized case reduce to

$$\begin{array}{ll} t_s = \frac{2\mu_r k_z}{\mu_r k_z + k_z^{'}} & r_s = \frac{\mu_r k_z - k_z^{'}}{\mu_r k_z + k_z^{'}} \\ t_s^{'} = \frac{2k_z^{'}}{k_z^{'} + \mu_r k_z} & r_s^{'} = \frac{k_z^{'} - \mu_r k_z}{k_z^{'} + \mu_r k_z} \end{array} \tag{2.66}$$

where t_s and r_s are the coefficients for the vacuum-NIM interface and $t_s^{'}$ and $r_s^{'}$ are the coefficients for the NIM-vacuum interface. The overall transmission and reflection coefficients T_s and R_s can be obtained by calculating the sum of all scattering events

$$T_s = t_s t_s{'} e^{ik_z^{'}d} + t_s t_s{'} r_s^{'2} e^{3ik_z^{'}d} + t_s t_s{'} r_s^{'4} e^{5ik_z^{'}d} + ... = \frac{t_s t_s{'} e^{ik_z^{'}d}}{1 - r_s^{'2} e^{2ik_z^{'}d}} \tag{2.67}$$

The actual transmission and reflection is calculated by taking the limit for $\epsilon_r \rightarrow -1$ and $\mu_r \rightarrow -1$ which yields

$$\lim_{\epsilon_r, \mu_r \rightarrow -1} T_s = \frac{t_s t_s{'} e^{ik_z^{'}d}}{1 - r_s^{'2} e^{2ik_z^{'}d}} = e^{-ik_z^{'}d} = e^{-ik_z d} \tag{2.68}$$

Which shows that the wave travels through the medium without experiencing any decay. For the reflection we can make a similar derivation which yields that the overall reflection equals zero.

$$\lim_{\epsilon_r, \mu_r \rightarrow -1} R_s = \lim_{\epsilon_r, \mu_r \rightarrow -1} r_s + \frac{t_s t_s{'} r_s^{'} e^{2ik_z^{'}d}}{1 - r_s^{'2} e^{2ik_z^{'}d}} = 0 \tag{2.69}$$

A similar derivation can be made for P-polarized waves by exchanging ϵ_r and μ_r in equations 2.67. This means that for a flat slab of a LHM which is perfectly impedance matched to the surroundings, any wave with an arbitrary polarization state will be transmitted without any decay. The amplification of the amplitude of evanescent waves does not violate energy conservation, as evanescent waves do not transport energy. This was the main conclusion from the paper by Pendry as it proves that both low- and high-frequency components of an image can travel through a NIM without any decay, resulting in a perfect lens.

In conventional optical systems, the high-frequency components which make up the smallest details of an object are evanescent in nature and decay exponentially with the distance from the source. Therefore these high-frequency components are lost in the image plane, and the resolution of a conventional lens is *diffraction limited*. The smallest distance between two points in the object plane (Δx) which can be distinguished in the image plane is given by

$$\Delta x \approx \frac{\lambda}{NA.n} \tag{2.70}$$

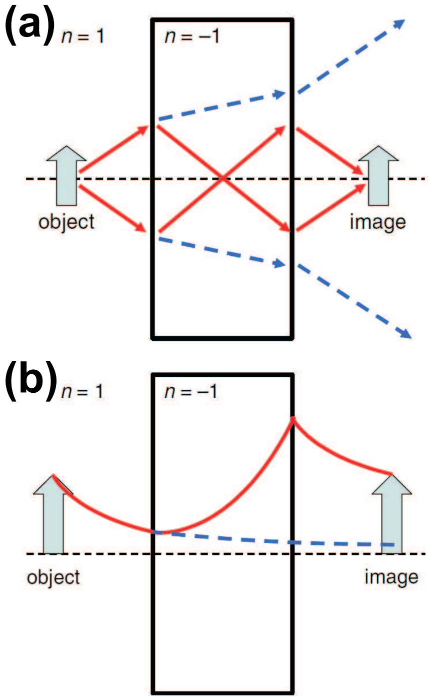

Figure 2.21: *Illustration of a NIM as perfect lens. All frequency components can travel through the lens without any decay. (a) Ray-tracing picture of imaging by a NIM lens (red lines) and comparison with a conventional lens (dotted blue lines). The image of the object is focussed once inside the lens and once in the image plane. (b) Illustration of enhancement of evanescent waves in a NIM (red lines) compared to the decay in a conventional lens (blue dotted lines).*

in which λ is the illumination wavelength, NA is the numerical aperture of the optical system and n the refractive index. For a NIM lens all components can travel without any decay, which implies that inside the NIM the evanescent waves are amplified in order to allow for transmission to the image plane without any losses (figure 2.21(b)).

2.3.2 Effective material parameters

Metamaterials are often described in terms of effective material parameters such as permittivity ϵ_{eff}, permeability μ_{eff}, refractive index n_{eff} and impedance Z_{eff}. These parameters describe the propagation properties of EM-waves through metamaterials by treating them as an effective medium. The metamaterial is considered as a homogeneous material (in the propagation direction) which implies that the metamaterial atoms or building blocks should be deep sub-wavelength in order for this approximation to be valid. In fact, this criterion is often used to discriminate between photonic crystals ($a \approx \lambda$) and metamaterials ($a \ll \lambda$) in function of the unit cell dimension a.

For optical metamaterials the effective parameters can be deduced from measurements or simulations in which both the amplitude and phase information of reflected and transmitted waves are recorded. The experimental extraction of these parameters is rather cumbersome for VIS and NIR metamaterials, but it is possible to extract both phase and amplitude by interferometric measurements [26]. In this thesis we performed effective parameter extraction based on finite element simulations and compared the simulated far-field transmission and reflection spectra with the measurement results. The homogenization step is performed by averaging out the electric and magnetic field amplitudes over one unit cell of the metamaterial and calculating the complex transmission and reflection coefficients at each side of the metamaterial [27]. In case of bi-anisotropy in the propagation direction, the effective parameters were extracted through a modified protocol [28] in which the transmission and reflection coefficients are extracted for illumination from both sides of the metamaterial layer. The values for the refractive index n and impedance Z are calculated by inversion of the scattering parameters (S parameters), the complex reflection and transmission coefficients.

We start from a homogeneous 1D slab of metamaterial with a thickness d and consider the transmission and reflection in terms of the transfer function which relates the transmitted and reflected waves to the incident wave according to

$$\mathbf{F}' = \mathbf{T}\mathbf{F} \tag{2.71}$$

where

$$\mathbf{F} = \begin{pmatrix} E \\ H_{red} \end{pmatrix} \tag{2.72}$$

with E and H_{red} the electric and magnetic field amplitudes of the incident wave ($\mathbf{F}$) and the transmitted wave ($\mathbf{F}'$). Here we use the reduced magnetic field which is the normalized magnetic field according to $H_{red} = i\omega\mu_0 H$ [29]. For an isotropic slab of material the transfer matrix can then be written as

$$\mathbf{T} = \begin{pmatrix} \cos(nkd) & -\frac{Z}{k}\sin(nkd) \\ \frac{k}{Z}\sin(nkd) & \cos(nkd) \end{pmatrix} \tag{2.73}$$

In practical applications we don't have direct access to the components of the transfer matrix **T** but to the scattering parameters (S-parameters) in the scattering matrix **S**

$$\mathbf{S} = \begin{pmatrix} S_{11} & S_{12} \\ S_{21} & S_{22} \end{pmatrix} \tag{2.74}$$

which can be related to the parameters of the T-matrix [27] by

$$\begin{aligned} S_{11} &= \frac{T_{11}-T_{22}+(ikT_{12}-\frac{T_{21}}{ik})}{T_{11}+T_{22}+(ikT_{12}+\frac{T_{21}}{ik})} \\ S_{12} &= \frac{2|\mathbf{T}|}{T_{11}+T_{22}+(ikT_{12}+\frac{T_{21}}{ik})} \\ S_{21} &= \frac{2}{T_{11}+T_{22}+(ikT_{12}+\frac{T_{21}}{ik})} \\ S_{22} &= \frac{T_{22}-T_{11}+(ikT_{12}-\frac{T_{21}}{ik})}{T_{11}+T_{22}+(ikT_{12}+\frac{T_{21}}{ik})} \end{aligned} \tag{2.75}$$

where S_{11} and S_{21} are the complex reflection and transmission coefficients for incidence from the top and S_{22} and S_{12} are the complex reflection and transmission coefficients for incidence from the bottom, which are extracted from two separate experiments or simulation runs.

Isotropic materials

For an isotropic material $T_{11} = T_{22} = T_s$ and $|\mathbf{T}| = 1$ (equation 2.74), such that the S-matrix is symmetric:

$$\begin{aligned} S_{11} = S_{22} &= \frac{\frac{1}{2}(\frac{T_{21}}{ik}-ikT_{12})}{T_S+\frac{1}{2}(ikT_{12}+\frac{T_{21}}{ik})} \\ S_{12} = S_{21} &= \frac{1}{T_S+\frac{1}{2}(ikT_{12}+\frac{T_{21}}{ik})} \end{aligned} \tag{2.76}$$

By substituting the T-matrix elements from equation 2.74 we obtain the relationship between the S-parameters and n and Z

$$\begin{aligned} S_{11} = S_{22} &= \frac{i}{2}(\frac{1}{Z} - Z)\sin(nkd) \\ S_{12} = S_{21} &= \frac{1}{\cos(nkd)-\frac{i}{2}(Z-\frac{1}{Z})\sin(nkd)} \end{aligned} \tag{2.77}$$

If all of the S-parameters are known, the equations above can be inversed in order to obtain n and Z

$$\begin{aligned} n &= \tfrac{1}{kd}\cos^{-1}[\tfrac{1}{2S_{21}}(1 - S_{11}^2 + S_{21}^2)] \\ Z &= \sqrt{\tfrac{(1+S_{11})^2 - S_{21}^2}{(1-S_{11})^2 - S_{21}^2}} \end{aligned} \tag{2.78}$$

In order to obtain physically sound values for the refractive index and impedance, the right branch of the cosine function has to be selected, bearing in mind that for passive materials, both $Im(n) > 0$ and $Re(Z) > 0$ should be fulfilled. The relative permittivity and permeability can subsequently be calculated from

$$\epsilon_r = \tfrac{n}{Z} \qquad \mu_r = nZ \tag{2.79}$$

which are complex functions of the wavelength.

Bi-anisotropic materials

When the metamaterial is not isotropic in the propagation direction, the S-matrix is no longer symmetric as the reflected and transmitted signals are different for illumination from the top or bottom. The S-parameters from both experiments are used in order to construct the overall T-matrix for the anisotropic metamaterial:

$$\begin{aligned} T_{11} &= \tfrac{(1+S_{11})(1-S_{22})+S_{21}S_{12}}{2S_{21}} \\ T_{12} &= \tfrac{(1+S_{11})(1+S_{22})-S_{21}S_{12}}{2S_{21}} \\ T_{21} &= \tfrac{(1-S_{11})(1-S_{22})-S_{21}S_{12}}{2S_{21}} \\ T_{22} &= \tfrac{(1-S_{11})(1+S_{22})+S_{21}S_{12}}{2S_{21}} \end{aligned} \tag{2.80}$$

For anisotropic metamaterials, the obtained values of the refractive index n are different for both propagation directions and these 2 values are very similar to equation 2.79

$$\begin{aligned} n_1 &= \tfrac{1}{kd}\cos^{-1}[\tfrac{1}{2S_{12}}(1 - S_{11}^2 + S_{12}^2)] \\ n_2 &= \tfrac{1}{kd}\cos^{-1}[\tfrac{1}{2S_{12}}(1 - S_{22}^2 + S_{12}^2)] \end{aligned} \tag{2.81}$$

while an overall effective refractive index n_{eff} can be defined by replacing S_{11} or S_{22} in the equations above by an average S-parameter $S_{av} = \sqrt{S_{11}S_{22}}$ such that

$$n_{eff} = \frac{1}{kd}\cos^{-1}[\frac{1}{2S_{21}}(1 - S_{av}^2 + S_{21}^2)] \tag{2.82}$$

The impedance is also different for both propagation directions and can be defined in terms of the T-matrix elements (equation 2.81)

$$Z_{eff} = \frac{(T_{22} - T_{11}) \pm \sqrt{(T_{22} - T_{11})^2 + 4T_{12}T_{21}}}{2T_{12}} \tag{2.83}$$

where the choice of the sign determines the different propagation directions. The extracted effective values for the refractive index and impedance are to be found in between the effective values obtained for top and bottom incidence without bi-anisotropy correction, as defined by equation 2.78.

2.3.3 Plasmonic metamaterial building blocks

Many of the plasmonic metamaterial atoms originated from the original attempts to realize NIMs at lower frequencies, for example in the microwave range. Researchers were trying to realize a material with simultaneously negative values for the electric permittivity ϵ and the magnetic permeability μ. The first realization of a NIM [25] consisted of two seperate structures that governed a negative electric and a negative magnetic response at an operational frequency of 10.5 GHz (figure 2.22). The negative electric response was realized by an array of parallel wires that act as a diluted plasma, while the negative magnetic response was induced by using split-ring resonators (SRRs), in which magnetic resonances can be excited. The SRRs can be seen as subwavelength LC-circuits: the ring behaves like a coil while the slit behaves as a capacitor.

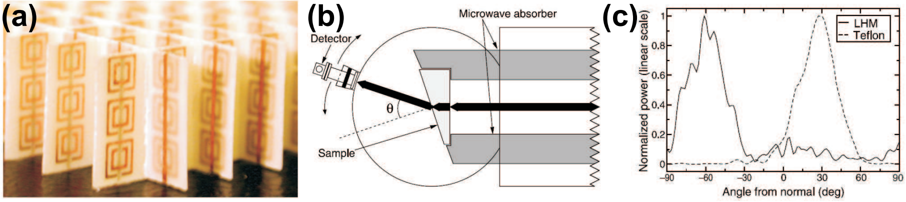

Figure 2.22: *First experimental realization of a NIM. (a) Picture of the NIM structure consisting of metallic wires and split-ring resonators. (b) Experimental setup to verify the negative value of the refractive index of a prism structure by Snell's law. (c) Angle dependent transmission through a NIM prism and a conventional prism strucutre. [25]*

In initial attempts to realize NIMs at higher frequencies, the SRRs were shrunk down to the limiting sizes that could be achieved with e-beam lithography, resulting in the first plasmonic NIMs in the NIR [30, 31]. These metamaterials obtained their negative magnetic response from LC-resonances, while the negative electric response is governed by the intrinsic material properties of the metals in the NIR. The first truly 3D metamaterials in the NIR were also realized by means of multilayers of stacked SRRs [32, 33]. Soon it was realized that further downscaling of conventional SRRs would lead to saturation of the magnetic resonance [34, 35], and new metamaterial atoms were proposed in order to push negative magnetic responses into the visible wavelength range. The saturation frequency can be increased by introducing more splits in a classical SRR [35], which is one of the paths that was pursued by different research groups simultaneously, resulting in new metamaterial atoms such as double-wire pairs [36, 37]. The next generation of NIMs emerged shortly afterwards and consisted of metal-insulator-metal (MIM) layers, perforated by a periodic array of holes, the so-called double fishnets [38–41]. The double fishnets are one of the most widely studied classes of NIMs for which negative refraction at NIR wavelengths could be experimentally verified [42]. In chapter 3 we discuss a self-assembly based version of a double fishnet NIM.

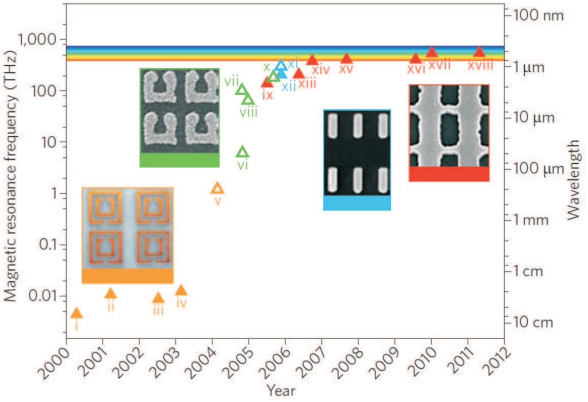

Figure 2.23: *Evolution of the scaling of NIMs. The different colors in the plot indicate the different metamaterial atoms used: Orange for double SRRs, Green for U-shaped SRRs, Blue for pairs of wires and Red for double fishnet materials [43].*

In recent years, the focus of the metamaterial community has diverged into several new areas such as chiral metamaterials (allowing to control the polarization state of light) and transition optics (slowing down light, invisibility cloaking), which use many different metamaterial atom designs. An overview of recent developments is beyond the scope of this thesis but can be found in reference [43].

2.4 Plasmonic biosensors

Plasmonic devices consist of nanometer and micrometer sized particles and surfaces, which are comparable in size to many biological substances such as cells, anti-bodies, anti-gens and even DNA. Therefore plasmonic sensors offer a good platform to interface with bio-molecules as the typical decay lengths of the enhanced fields are of the same order as the investigated molecules. The plasmonic structures can be fabricated in bio-compatible materials such as Gold (Au), Silica (SiO_2) and Silicon (Si), which makes them suitable for in-vitro and in-vivo applications. On top of that, different mature types of chemical functionalizations can be applied on these materials in order to make the sensors specific to the desired analyte molecules.

2.4.1 Surface Plasmon Polariton (SPP) sensing

SPP sensing is one of the most widely spread plasmon based commercial platforms [44] in life sciences. The sensing principle is illustrated in figure 2.24. The analyte solution flows through a channel which is in contact with a (functionalized) gold surface. A P-polarized beam excites plasmons on the gold surface by SPP coupling in the Kretschmann [11] configuration. Two configurations are typically used: (1) The wavelength is fixed while the angle of incidence is scanned (angular approach); (2) The angle of incidence is fixed while the wavelength is scanned (spectral approach); In both cases, a dip in the reflection spectrum is observed at the angular/spectral position where SPPs are excited. These propagating SPPs are prone to changes in the dielectric environment and as a result an angular/spectral shift will be observed for changes in the analyte solution or binding events at the gold surface. Typically with increasing concentration of the analyte or upon binding events on the gold layer, (local) refractive index is increased, resulting in a shift of the spectral/angular position to larger values. The electric field of the propagating SPP decays exponentially with the distance from the gold surface, with typical decay lengths of a few 100 nanometers. Therefore SPP-based sensors are sensitive to concentration changes in the bulk and to binding events at the gold surface.

As outlined in section 2.2.4 it is possible to measure both the intensity and phase of the SPP resonance (see fig 2.24(b)), and the resulting line widths differ tremendously, allowing to reach detection limits which are 2 orders of magnitude smaller for phase-based SPR sensing [18].

2.4.2 Localized Surface Plasmon Resonance (LSPR) sensing

Localized surface plasmon resonances are highly susceptible to their dielectric environment and show pronounced red-shifts of the plasmon resonance as the refractive index of the surrounding medium is increased. Due to the strong confinement of LSPRs, the field enhancement around the plasmonic structure is limited to the near field, with decay lengths in the order of a few tens of nanometers (depending on the resonance wavelength and the nanostructure itself). Therefore LSPR-based sensors

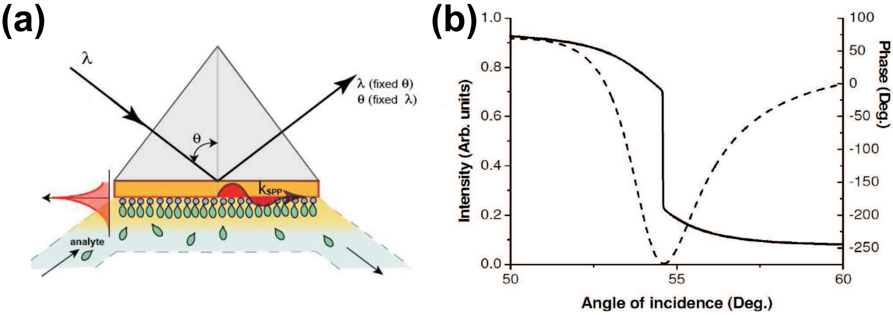

Figure 2.24: *(a) Schematic overview of an SPP sensing experiment. (b) Example of a measurement for an SPP-based sensor showing both intensity and phase based signals in configuration (1). [18].*

are only sensitive to changes in the immediate environment of the nanoparticles and less sensitive to bulk refractive index changes than SPP-based sensing platforms. The sensor response is largely dominated by "hot-spots", the regions around the nanostructures where the field enhancements are maximized. In optimizing the sensor performance, it is important to maximize the sensing volume [22, 45] and the contact area with the sensing solution, as these parameters determine the final sensor sensitivity.

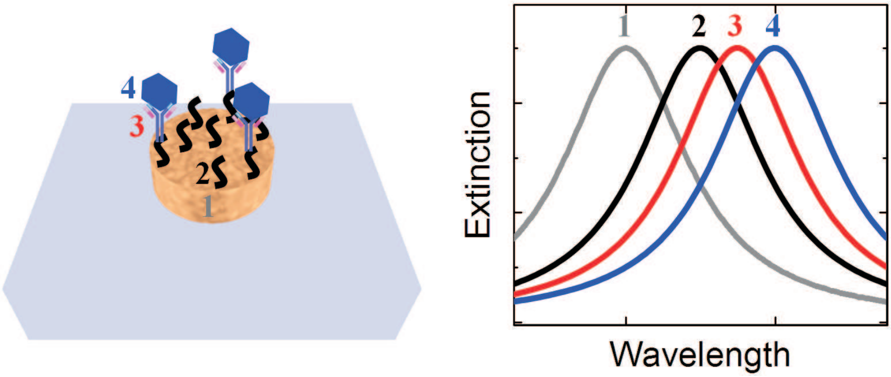

Figure 2.25: *Schematic overview of an LSPR sensing experiment on a gold nanodisk. The extinction spectra are shown for the bare gold nanodisk (1), the disk functionalization with a self-assembled monolayer (SAM)(2), antibodies coupled to the SAM (3) and antigens captured by the antibodies (4).*

A recent review on LSPR based sensing platforms can be found in reference [46].

2.4.3 Characterization of sensor performance

In this section we introduce the most important parameters that quantify the sensor performance for plasmonic sensors based on refractive index changes. Some of these parameters are inherent to the plasmonic structure, while others show a strong dependence on the surface functionalization and the chemical reactions that take place in (bio-) sensing experiments.

The tunability of plasmon resonances (section 2.2.3) can be exploited in optimizing the sensor performance. The intrinsic properties of the plasmon resonance play a key role in the efficiency of the sensor for practical applications. The geometric design of the plasmon resonator determines the position of hot spots and its accessibility for the analyte solutions. A proper design of the plasmonic structure results in high values for the *sensitivity (S)*: the observed red shift of the plasmon resonance ($\Delta\lambda_{res}$) per refractive index unit (RIU), which is given in units of nm/RIU.

$$S = \frac{\Delta\lambda_{res}}{\Delta n} \tag{2.84}$$

The sensitivity largely depends on the nanostructure and takes different values for different plasmonic modes. Larger values for S are expected for plasmon resonances at at longer wavelengths. Each plasmonic mode is also characterized by a certain *line width (*Γ*)* which is defined as the *full width at half maximum* value of the plasmon line shape. The line width is a measure for the damping of the plasmon resonance, which depends strongly of the nature of the plasmon resonance. Dipolar modes radiate strongly and the resulting line widths are broad while dark higher order modes radiate less and the resulting line widths are much more narrow. As the line width also strongly depends on the resonant wavelength, a *quality factor (Q-factor)* of the resonance is introduced, which is given by the ratio of the resonant wavelength and its width.

$$Q = \frac{\lambda_{res}}{\Gamma} \tag{2.85}$$

The value of the Q-factor determines the line width of the plasmon resonance (relative to its spectral position) and higher Q-factors allow to observe smaller spectral shifts of plasmon resonances with increased accuracy. Therefore in terms of sensing the sensor performance is often expressed in a *Figure Of Merit (FOM)*, which relates the line width to the sensitivity of the sensor.

$$FOM = \frac{\frac{\Delta\lambda_{res}}{\Delta n}}{\Gamma} \tag{2.86}$$

The FOM is in general a good measure for the intrinsic sensor performance, and higher FOM values allow a more accurate determination of the resonance position, which implies that smaller spectral shifts can be observed. The smallest refractive index change (Δn) that can be observed with the sensor, which is called the *detection limit (DL)* and expressed in RIUs.

2.4.4 Surface functionalization

The typical dimensions of plasmonic structures are matched pretty well with the sizes of biological molecules, cells and even DNA, which makes them really useful for biological sensing applications. It is critical to bring the analyte molecules in the vicinity of the plasmonic sensors in order to obtain accurate measurement results. To that extent, chemical functionalization of the plasmonic structures is very important to obtain the best possible interfacing properties between the sensors and the analytes. The typical sample structures used in this thesis are fabricated in gold and silica, which can both be chemically functionalized. Gold surfaces show a high affinity for thiol (SH-groups) [47] while silica and silicon surfaces show a high affinity for silane (Si-O-groups) [48]. Both thiol and silane based chemistry can be exploited to form self-assembled monolayers (SAMs) on gold and silicon-based structures with nearly perfect sample coverage. These SAMs can be tailored at will for a specific application: one side is designed to realize the coupling with the sensor surface, while the other can be tailored to couple analyte molecules or antibodies (biofunctionalization). Typically the molecules making up the SAM consist of two functional end-groups and a (long) chain of atoms in between them which can form Van-Der-Waals bonds with the neighboring SAM molecules, resulting in rather densely packed monolayers on the functionalized substrates. For most applications the SAMs are formed upon exposure of the samples to a solution of the SAM molecules which can then self-assemble onto the sample surface.

2.4.5 Other types of plasmonic biosensors

Next to refractive index based plasmonic biosensors the most promising application is surface-enhanced Raman spectroscopy (SERS) [49]. In SERS the strong field enhancement of plasmonic resonances is exploited to enhance Raman signals of molecules bound to or in the vicinity of the surface of a nanostructure. The major advantage of SERS is that it is a label-free technique in which the obtained spectrum yields a molecular footprint containing Raman peaks that are specific to the molecule that is detected. Due to the strong local field enhancements near plasmonic structures the sensitivity can go down to the single-molecule level.

2.5 Spectroscopic ellipsometry

Spectroscopic ellipsometry is a common technique in material sciences which is used to determine the optical properties of transparent layers and thin metallic layers. The angle- and polarization dependent reflection and/or transmission of a layered structure is recorded and fitted to a theoretical model. In that way the thickness, refractive index (permittivity) and roughness of the investigated layer(s) can be deduced. A schematic overview of reflection based ellipsometry is presented in figure 2.26. The polarization of the incident wave is modulated between P and S by a rotating polarizer (section 2.5.3) or a photo-elastic modulator (section 2.5.4). By performing lock-in measurements at the modulation frequency, both the amplitude and phase of the reflected beam are recorded for the two polarization states.

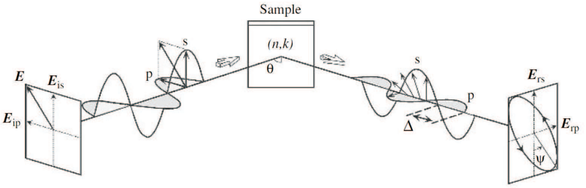

Figure 2.26: *Schematic overview of spectroscopic ellipsometry measurements. A linearly polarized plane wave is converted into an elliptically polarized wave upon reflection from the sample. [50]*

At the interfaces between the different layers in the sample, the reflection for P- and S-polarized waves is determined by the Fresnel reflection coefficients (equations 2.34 and 2.36),which are in general complex numbers. Therefore, upon reflection at each interface, the amplitude and phase of the reflected wave are different for the two polarization states, resulting in an elliptically polarized wave. This explains the name spectroscopic ellipsometry: the polarization ellipse of the sample is measured for different wavelengths, such that the optical properties of the investigated sample can be quantified.

2.5.1 Measured quantities

The polarization ellipse (figure 2.27) of an EM wave can be described in different reference frames, depending on the application. For spectroscopic ellipsometry measurements the polarization state is usually decribed in terms of $\tan\Psi$ and $\cos\Delta$. These numbers represent the amplitude ratio between the reflected P- and S-polarized waves ($\tan\Psi$) and the phase difference (Δ) between them (figure 2.26). The relationship between these two parameters and the sample response is given by the main equation of ellipsometry

$$\rho = \frac{r_p}{r_s} = \frac{\frac{E_{r,p}}{E_{i,p}}}{\frac{E_{r,s}}{E_{i,s}}} = \tan\Psi e^{i\Delta} = \tan\Psi(\cos\Delta + i\sin\Delta) \qquad (2.87)$$

The value of $\tan\Psi$ describes the amplitude ratio between P- and S-polarized waves, while their phase difference Δ determines the polarization state. For positive values of Δ the polarization vector rotates right-handed while for negative values of Δ it rotates left-handed as the wave propagates.

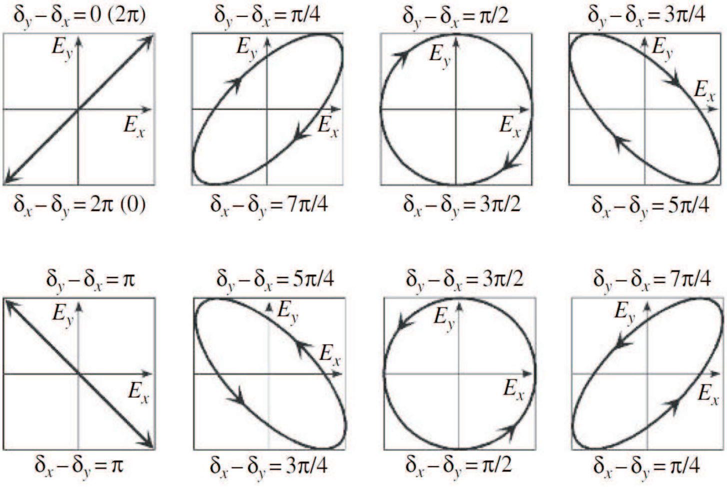
$\delta_y - \delta_x = 0\ (2\pi)$
$\delta_y - \delta_x = \pi/4$
$\delta_y - \delta_x = \pi/2$
$\delta_y - \delta_x = 3\pi/4$
E_y
E_x
$\delta_x - \delta_y = 2\pi\ (0)$
$\delta_x - \delta_y = 7\pi/4$
$\delta_x - \delta_y = 3\pi/2$
$\delta_x - \delta_y = 5\pi/4$
$\delta_y - \delta_x = \pi$
$\delta_y - \delta_x = 5\pi/4$
$\delta_y - \delta_x = 3\pi/2$
$\delta_y - \delta_x = 7\pi/4$
$\delta_x - \delta_y = \pi$
$\delta_x - \delta_y = 3\pi/4$
$\delta_x - \delta_y = \pi/2$
$\delta_x - \delta_y = \pi/4$

Figure 2.27: *The polarization ellipse is confined to the square defined by the electric field magnitude along the X and Y directions, which are equal in this example (*$\tan\Psi = 1$*). For changing values of the phase differences* $\delta_y - \delta_x$ *the wave has a different polarization state. The respective states are: linearly polarized at* 45^o*, elliptically polarized (right), right circularly polarized, elliptically polarized (right), linearly polarized at* -45^o*, elliptically polarized (left), left circularly polarized and elliptically polarized (left). [50]*

An alternative representation of the ellipsometric parameters can be given in terms of the ellipticity $\epsilon = \tan\gamma$ and the rotation angle θ, which are not used that often in terms of spectroscopic ellipsometry. These quantities are mainly used for magneto-optic Kerr effect (MOKE) measurements in which the magnetic properties of a sample are investigated by means of polarized light. The tangent of the ratio between the long and short axis of the polarization ellipse gives the ellipticity ϵ while the orientation of the long axes with respect to the incident wave is given by a rotation angle θ. In MOKE measurements the anisotropy introduced by the external magnetic field is quantified such that switching of the magnetization upon changes in the direction and amplitude of the external magnetic field can be observed. The two representations can be used interchangeably and the main advantage for (ϵ, θ) over (Ψ, Δ) is that the ellipticity ϵ describes the polarization state in the most general way, independent of the frame of reference. The relationships between them [51] are given by equations 2.89 and can be deduced directly from the Stokes parameters. In the remainder of this thesis, we will mainly refer to ellipsometric parameters in terms of (Ψ, Δ).

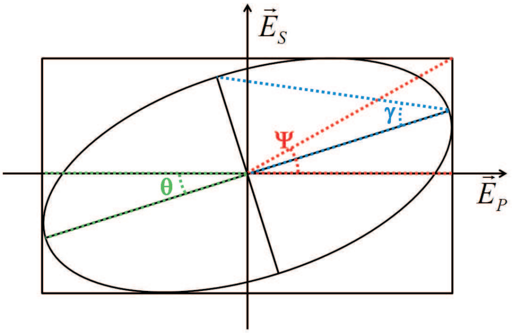

Figure 2.28: *The polarization ellipse with the ellipsometric angles* Ψ, γ *and* θ.

$$\begin{aligned}
\Psi &= \tan^{-1}\sqrt{\frac{1+\tan^2\theta\tan^2\gamma}{\tan^2\theta+\tan^2\gamma}} && \Psi \in <0, \tfrac{\pi}{2}> \\
\Delta &= 2\tan^{-1}\frac{\sqrt{\cos^2 2\gamma\cos^2 2\theta}-\sin^2 2\theta\cos^2 2\gamma}{\sin 2\gamma} && \Delta \in <-\pi, \pi> \\
\theta &= \tan^{-1}\frac{\sin 2\Psi\cos\Delta}{\sqrt{1-\sin^2 2\Psi\sin^2\Delta}-\cos 2\Psi} && \theta \in <\tfrac{-\pi}{2}, \tfrac{\pi}{2}> \\
\gamma &= \frac{1}{2}\tan^{-1}\frac{\sin 2\Psi\sin\Delta}{\sqrt{1-\sin^2 2\Psi\sin^2\Delta}} && \gamma \in <\tfrac{-\pi}{4}, \tfrac{\pi}{4}>
\end{aligned} \tag{2.88}$$

2.5.2 Mathematical description of polarized light

Complex optical systems can be described by means of the Jones and Mueller/Stokes matrix formalism, in which each optical component of the system is described by a characteristic matrix. The total transmission through an optical setup is given by the matrix product of all matrices with the polarization vector of the incident wave. The Jones matrix formalism consists of $2x2$ matrices for optical components and 2-component Jones vectors, while the the Mueller/Stokes formalism consists of $4x4$ Mueller matrices in conjunction with 4-component Stokes vectors. The Jones matrix formalism allows to describe all the polarization states discussed before, but does not allow to describe unpolarized light. The Mueller/Stokes formalism is more advanced and allows to describe any possible (partial) polarization state. For spectroscopic ellipsometry measurements the Jones formalism is sufficient, as only linear, circular and elliptical polarization states are used. We'll briefly introduce the Mueller/Stokes formalism as well, as the four Stokes parameters $S_0 - S_3$ are measured in a spectroscopic ellipsometry measurement.

Jones vectors

In section 2.1.2 we introduced the different polarization states of light, which all can be described by their Jones vector. Let's assume an EM wave which is propagating in the z-direction and which can be written as a superposition of two plane waves oscillating in the x- and y-directions with frequency ω

$$\mathbf{E}(z,t) = \begin{pmatrix} E_{x,0}e^{i(\omega t - k_z z + \delta_x)} \\ E_{y,0}e^{i(\omega t - k_z z + \delta_y)} \end{pmatrix} = e^{i(\omega t - k_z z)} \begin{pmatrix} E_{x,0}e^{i\delta_x} \\ E_{y,0}e^{i\delta_y} \end{pmatrix} \tag{2.89}$$

Usually the term $e^{i(\omega t - \mathbf{k}z)}$ is dropped

$$\mathbf{E}(z,t) = \begin{pmatrix} E_x \\ E_y \end{pmatrix} \tag{2.90}$$

In which E_x and E_y can be written as the product of the amplitude and phase of the electric field along the x- and y-directions

$$\begin{aligned} E_x &= |E_x|e^{i\delta_x} \\ E_y &= |E_y|e^{i\delta_y} \end{aligned} \tag{2.91}$$

The electric field components can be rewritten in function of the phase difference $\delta_x - \delta_y$

$$\begin{aligned} E_x &= E_{x,0}e^{i(\delta_x - \delta_y)} = |E_x|e^{i(\delta_x - \delta_y)} \\ E_y &= E_{y,0} = |E_y| \end{aligned} \tag{2.92}$$

while the total field intensity is given by

$$I = I_x + I_y = E_{x,0}^2 + E_{y,0}^2 = |E_x|^2 + |E_y|^2 = E_x E_x^* + E_y E_y^* \tag{2.93}$$

As we are only interested in the relative phase and amplitude for the different components, the intensity I is usually normalized such that $I = 1$. Therefore we can write the linear polarization states along the x- and y-axis as

$$E_{lin,x} = \begin{pmatrix} 1 \\ 0 \end{pmatrix} \qquad\qquad E_{lin,y} = \begin{pmatrix} 0 \\ 1 \end{pmatrix} \tag{2.94}$$

For any linear polarization state which makes an angle Ψ with the x-axis, the general Jones vector is given by

$$E_{lin,\Psi} = \begin{pmatrix} \sin\Psi \\ \cos\Psi \end{pmatrix} \tag{2.95}$$

For the circular polarization states the phase difference between E_x and E_y is $\pi/2$, from which we can write the normalized Jones vectors as

$$E_{circ,right} = \frac{1}{\sqrt{2}} \begin{pmatrix} 1 \\ i \end{pmatrix} \qquad E_{circ,left} = \frac{1}{\sqrt{2}} \begin{pmatrix} i \\ 1 \end{pmatrix} \tag{2.96}$$

The most general shape of polarization is the elliptical polarization for which the main axis of the polarization ellipse rotated with an angle Ψ with respect to the x-axis, which can be written as

$$E_{ellipt,\Psi} = \begin{pmatrix} \sin\Psi e^{i(\Delta)} \\ \cos\Psi \end{pmatrix} \tag{2.97}$$

Jones matrix

Optical components can be described in terms of their Jones matrix, which characterizes their polarization dependent optical response. In this section we give an overview of the different components which are relevant to describe ellipsometry measurements in the different configurations used throughout this thesis.

Linear polarizers are used in the different types of ellipsometry setups both on the incident side as polarizer (P) and at the detection side as analyzer (A). A linear polarizer with the its transmission axis along the x-direction is described by

$$P(0^o) = A(0^o) = \begin{pmatrix} 1 & 0 \\ 0 & 0 \end{pmatrix} \tag{2.98}$$

For a polarizer under an arbitrary angle ϕ with respect to the x-axis, the resulting matrix can be calculated by using the rotation matrix $R(\alpha)$.

$$R(\phi) = \begin{pmatrix} \cos\phi & -\sin\phi \\ \sin\phi & \cos\phi \end{pmatrix} \tag{2.99}$$

If a complex optical system such as an ellipsometry setup is described, different rotation matrices have to be introduced in order to describe the overall optical response of the setup, as the different components are usually rotated with respect to the optical axes of the previous component.

The response of a sample can be described by the complex reflection and transmission parameters given by the Fresnel equations, which are related to each other by the ellipsometric angles Ψ and Δ that appear in the sample matrix S

$$S = \begin{pmatrix} \sin\Psi e^{i\Delta} & 0 \\ 0 & \cos\Psi \end{pmatrix} \tag{2.100}$$

This matrix can be deduced immediately from the definitions of $\tan\Psi$ and Δ, if we define the x-direction as the P-axis and the y-direction as the S-axis in figure 2.26:

$$\tan\Psi = \frac{\sin\Psi}{\cos\Psi} = \frac{|r_p|}{|r_s|} \tag{2.101}$$

The phase difference between the P- and S-polarized waves is defined as $\Delta = \delta_x - \delta_y = \delta_p - \delta_s$ as introduced by equation 2.93. As an example we show the full description of figure 2.26 in Jones matrices

$$\begin{pmatrix} E_{r,p} \\ E_{r,s} \end{pmatrix} = \begin{pmatrix} \sin\Psi e^{i\Delta} & 0 \\ 0 & \cos\Psi \end{pmatrix} \begin{pmatrix} E_{i,p} \\ E_{i,s} \end{pmatrix} = \begin{pmatrix} \sin\Psi e^{i\Delta} E_{i,p} \\ \cos\Psi E_{i,s} \end{pmatrix} \tag{2.102}$$

from which we can see that a linearly polarized wave (at 45^o) is converted into an elliptically polarized wave upon reflection from the sample. To measure the phase difference Δ in practical applications, we need to apply a modulation of the polarization, in order to perform lock-in measurements at the modulation frequency ω. Two types of modulation are used most often: a polarizer rotating at a frequency ω (section 2.5.3) or a photo-elastic modulator oscillating at frequency ω (section 2.5.4).

For a rotating linear polarizer, the Jones matrix is expressed as function of the polarizer angle $\alpha = \omega t$ and it is given by the product of $R(\alpha)$ and a linear polarizer matrix (equation 2.99).

A photo-elastic modulator consists of a fused quartz crystal to which two electrodes are connected. An oscillating electric field is applied to these electrodes at $50kHz$, which corresponds to the resonant oscillation frequency of the piezo transducer. The modulation of the crystal introduces stress into the dielectric material which changes the electron density along the stress direction. This effect introduces anisotropy in the crystal, which gives rise to a phase difference between light waves that pass through the crystal with a polarization along or perpendicular to the stress direction. The introduced phase difference is time-dependent and is given by

$$\delta = F\sin(\omega t) \tag{2.103}$$

where $\omega = 2\pi\nu$ with $\nu = 50kHz$. F is the phase amplitude and is proportional to V/λ with V the applied voltage to the crystal and λ the wavelength of the incident light. In a spectroscopic ellipsometry measurement δ is kept constant for different wavelengths by adjusting the applied voltage to the wavelength. The Jones matrix of a PEM is given by

$$\begin{pmatrix} 1 & 0 \\ 0 & e^{i\delta} \end{pmatrix} \tag{2.104}$$

Stokes parameters

Although the Jones formalism provides a very elegant means to describe polarized light, it does not provide the possibility to define partially polarized or unpolarized light. These polarization states can be described by means of Stokes parameters ($S_0 - S_3$), which make up a 4-component vector. Similar to the Jones matrices defined before, Mueller matrices can be used to describe any optical component and in that way to fully describe an optical setup. For the systems used in this thesis we can describe all properties in terms of Jones matrices, so therefore we only introduce the Stokes parameters here, as they are the parameters that come out of an ellipsometry measurement. If we consider waves with a polarization vector along the x- and y-direction, the corresponding Stokes vectors are given by

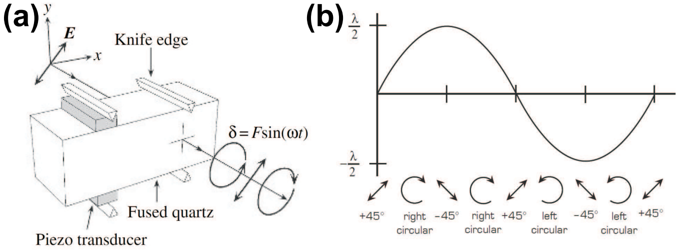
(a)
y
E
x
Knife edge
δ = Fsin(ωt)
Fused quartz
Piezo transducer
(b)
λ/2
−λ/2
+45°
right circular
−45°
right circular
+45°
left circular
−45°
left circular
+45°

Figure 2.29: *(a) Schematic overview of a PEM. (b) Illustration of the polarization states during one modulation cycle with the peak retardation $\lambda/2$.*

$$\begin{aligned} S_0 &= I_x + I_y \\ S_1 &= I_x - I_y \\ S_2 &= I_{+45^o} - I_{-45^o} \\ S_3 &= I_{circ,right} - I_{circ,left} \end{aligned} \tag{2.105}$$

The S_0 parameter described the total light intensity, while the $S_1 - S_3$ parameters describe the polarization state in terms of the differences between all possible linear and circular polarization states. By writing the different Stokes parameters in terms of the electric field values, we can relate them to the ellipsometric parameters (Ψ, Δ) and (ϵ, μ).

$$S_0 = I_x + I_y = E_{x,0}^2 + E_{y,0}^2 = E_x E_x^* + E_y E_y^* \tag{2.106}$$

$$S_1 = I_x - I_y = E_{x,0}^2 - E_{y,0}^2 = E_x E_x^* - E_y E_y^* \tag{2.107}$$

For the S_2 parameter we use a rotation of the x- and y-directions over -45^o

$$\begin{pmatrix} E_{-45^o} \\ E_{+45^o} \end{pmatrix} = \begin{pmatrix} \cos -45^o & \sin -45^o \\ -\sin -45^o & \cos -45^o \end{pmatrix} \begin{pmatrix} E_x \\ E_y \end{pmatrix} = \frac{1}{\sqrt{2}} \begin{pmatrix} E_x - E_y \\ E_x + E_y \end{pmatrix} \tag{2.108}$$

From which we can derive S_2

$$\begin{aligned} S_2 &= E_{+45^o} E_{+45^o}^* - E_{-45^o} E_{-45^o}^* \\ &= \frac{1}{2}[(E_x + E_y)(E_x^* + E_y^*) - (E_x - E_y)(E_x^* - E_y^*)] \\ &= E_x E_y^* + E_x^* E_y \end{aligned} \tag{2.109}$$

For S_3 we can make a similar derivation as for S_2 where we rewrite $E_{circ,left}$ and $E_{circ,right}$ in function of E_x and E_y

$$\begin{pmatrix} E_{circ,left} \\ E_{circ,right} \end{pmatrix} = \frac{1}{\sqrt{2}} \begin{pmatrix} 1 & i \\ 1 & -i \end{pmatrix} \begin{pmatrix} E_x \\ E_y \end{pmatrix} = \frac{1}{\sqrt{2}} \begin{pmatrix} E_x + iE_y \\ E_x - iE_y \end{pmatrix} \tag{2.110}$$

From which we obtain S_3

$$\begin{aligned} S_3 &= E_{circ,right}E^*_{circ,right} - E_{circ,left}E^*_{circ,left} \\ &= \frac{1}{2}[(E_x - iE_y)(E^*_x + iE^*_y) - (E_x + iE_y)(E^*_x - iE^*_y)] \\ &= i(E_xE^*_y - E^*_xE_y) \end{aligned} \tag{2.111}$$

Now we can relate the Stokes parameters to the ellipsometric angles (Ψ, Δ). For S_0 we start from equation 2.107 and we see from the main equation of ellipsometry (2.88) and figure 2.28 that we obtain a normalized vector with magnitude 1.

$$S_0 = E^2_{x,0} + E^2_{y,0} = E_xE^*_x + E_yE^*_y = \sin^2\Psi + \cos^2\Psi = 1 \tag{2.112}$$

Similarly for S_1 we obtain

$$S_1 = E^2_{x,0} - E^2_{y,0} = E_xE^*_x - E_yE^*_y = \sin^2\Psi - \cos^2\Psi = -\cos 2\Psi \tag{2.113}$$

For S_2 we start from equation 2.110 and we use that $(E_xE^*_y)^* = E^*_xE_y$ such that S_2 can be rewritten to

$$S_2 = 2Re(E_xE^*_y) = 2Re(E^*_xE_y) \tag{2.114}$$

For complex numbers C we can write $Re(C) = Re(C^*)$ and $Im(C) = -Im(C^*)$. From equation 2.93 we can write $E^*_x = E_{x,0}e^{-i(\delta_x - \delta_y)}$ and $E_y = E_{y,0}$ which yields

$$\begin{aligned} S_2 &= 2E_{x,0}E_{y,0}Re(e^{-i(\delta_x - \delta_y)}) \\ &= 2\sin\Psi\cos\Psi\cos(\delta_x - \delta_y) \\ &= 2\sin\Psi\cos\Psi\cos\Delta \\ &= \sin 2\Psi\cos\Delta \end{aligned} \tag{2.115}$$

Using $Im(C) = \frac{C+C^*}{2i}$ we obtain S_3 from equation 2.112

$$\begin{aligned} S_3 &= -Im(E_xE^*_y) = Im(E^*_xE_y) \\ &= 2E_{x,0}E_{y,0}Im(e^{-i(\delta_x - \delta_y)}) \\ &= 2\sin\Psi\cos\Psi\sin(\delta_x - \delta_y) \\ &= 2\sin\Psi\cos\Psi\sin\Delta \\ &= \sin 2\Psi\sin\Delta \end{aligned} \tag{2.116}$$

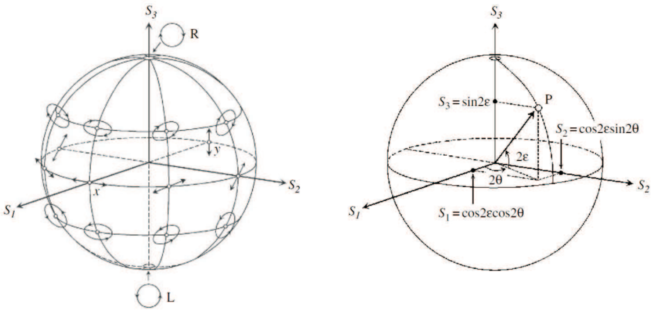

Figure 2.30: *The Poincaré sphere as a representation of various polarization states and the ellipsometric angles (ϵ, θ) [50]*

Any polarization state can be described by a point on the Poincaré sphere (figure 2.30), which is a graphical illustration based on the Stokes parameters. The S_0 parameter gives the intensity of the light which corresponds to the radius of the sphere, while $S_1 - S_3$ are the coordinate axes for the construction of the sphere. The point P on the sphere corresponding to a certain polarization state is constructed by using the Stokes parameters and the corresponding angles of 2ϵ and 2θ give the polar coordinates of the point P (equation 2.118). If we consider the Poincaré sphere as a globe then the equator corresponds to linear polarization states and the poles represent circular polarization states. A polarization state in between those corresponds to elliptical polarization and in the northern hemisphere it rotates right while in the southern hemisphere it rotates left.

$$\begin{aligned} S_1 &= \cos 2\epsilon \cos 2\theta \\ S_2 &= \cos 2\epsilon \sin 2\theta \\ S_3 &= \sin 2\epsilon \end{aligned} \tag{2.117}$$

2.5.3 Rotating analyzer/polarizer ellipsometry

In a rotating polarizer ellipsometry setup either the polarizer (P) or the analyzer (A) (figure 2.31) can be rotating in order to modulate the signal and extract the phase difference Δ between P- and S-polarized waves. Here we consider the case where the analyzer is rotating at an angular frequency ω such that the rotation angle is given by $\phi_A = \omega t$.

The transmission through the setup can then be described by Jones matrices

$$L_{out} = AR(\phi_A)SR(-\phi_P)PL_{in} \tag{2.118}$$

In this configuration L_{out} represents the detected signal of the photodetector along the polarization axis (ϕ_A) of the analyzer (A) , while L_{in} represents the incident

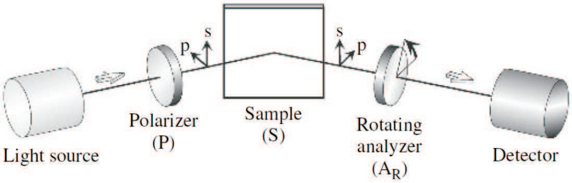

Figure 2.31: *Schematic overview of a rotating analyzer ellipsometry setup. [50]*

wave with polarization along the polarization axis (ϕ_P) of the polarizer (P). This representation is used because the Jones formalism doesn't allow to describe the unpolarized light source, but the transmitted light after the polarizer (P) contains only linearly polarized light along the polarization axis of P. Similarly, the photodetector will only detect linearly polarized waves with the polarization along the axis of A. With respect to the coordinate system of $(E_{i,p}, E_{i,s})$ we should formally write the Jones matrices $R(-\phi_P)PR(\phi_P)$ and $R(-\phi_A)AR(\phi_A)$ for the polarizer and analyzer respectively. Due to the definitions of L_{out} and L_{in} we can drop the terms $R(\phi_P)$ and $R(-\phi_A)$, which results in the overall matrix formulation for the setup

$$\begin{pmatrix} E_A \\ 0 \end{pmatrix} = \begin{pmatrix} 1 & 0 \\ 0 & 0 \end{pmatrix} \begin{pmatrix} \cos\phi_A & \sin\phi_A \\ -\sin\phi_A & \cos\phi_A \end{pmatrix} \begin{pmatrix} \sin\Psi e^{i\Delta} & 0 \\ 0 & \cos\Psi \end{pmatrix} \begin{pmatrix} \cos\phi_P & -\sin\phi_P \\ \sin\phi_P & \cos\phi_P \end{pmatrix} \begin{pmatrix} 1 & 0 \\ 0 & 0 \end{pmatrix} \begin{pmatrix} 1 \\ 0 \end{pmatrix} \tag{2.119}$$

In typical ellipsometry measurements the polarizer on the incident side is set at 45^o and in that case the matrix expression can be simplified to

$$\begin{pmatrix} E_A \\ 0 \end{pmatrix} = \frac{1}{\sqrt{2}} \begin{pmatrix} 1 & 0 \\ 0 & 0 \end{pmatrix} \begin{pmatrix} \cos\phi_A & \sin\phi_A \\ -\sin\phi_A & \cos\phi_A \end{pmatrix} \begin{pmatrix} \sin\Psi e^{i\Delta} \\ \cos\Psi \end{pmatrix} \tag{2.120}$$

From which we obtain the expression for E_A (we drop the constant $1/\sqrt{2}$)

$$E_A = \cos\phi_A \sin\Psi e^{i\Delta} + \sin\phi_A \cos\Psi \tag{2.121}$$

The normalized relative light intensity measured by the detector is obtained using equation 2.94 and dropping the constant factor of $1/2$

$$\begin{aligned} I &= |E_A|^2 \\ &= I_0(1 - \cos 2\Psi \cos 2\phi_A + \sin 2\Psi \cos\Delta \sin 2\phi_A \\ &= I_0(1 + S_1 \cos 2\phi_A + S_2 \sin 2\phi_A) \end{aligned} \tag{2.122}$$

In which I_0 is the normalized intensity of the incident beam. Moreover, it is important to note that the modulation of the intensity of the transmitted light varies

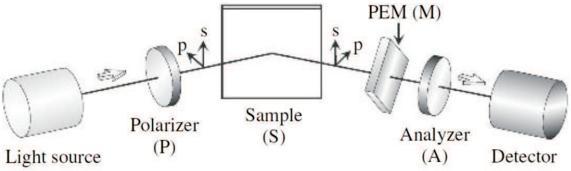

Figure 2.32: *Schematic overview of a PEM-based ellipsometry setup. [50]*

as a function of $2A$ as a rotation of the analyzer of 180^o yields the same transmitted intensity. By substituting $\phi_A = \omega t$ in the expression above, we obtain the time-dependent transmitted intensity.

$$I = I_0(1 + S_1 \cos 2\omega t + S_2 \sin 2\omega t) \tag{2.123}$$

So far we considered the case where the polarizer angle P was fixed at 45^o, which was the configuration used for all ellipsometry experiments described in this thesis. Depending on the sample structure under investigation, it can be useful to set different polarizer angles to improve the signal-to-noise ratio. The measured signal will also be time dependent and the Fourier components α and β can be deduced by plugging in the correct angle for P in equation 2.220. In their most general form, the normalized Fourier coefficients can be written as

$$\begin{aligned} S_1 &= \frac{\cos 2\phi_P - \cos 2\Psi}{1-\cos 2\phi_P \cos 2\Psi} = \frac{\tan^2\Psi - \tan^2\phi_P}{\tan^2\Psi - \tan^2\phi_P} \\ S_2 &= \frac{\sin 2\Psi \cos\Delta \sin 2\phi_P}{1-\cos 2\phi_P \cos 2\Psi} = \frac{2\tan\Psi\cos\Delta\tan\phi_P}{\tan^2\Psi - \tan^2\phi_P} \end{aligned} \tag{2.124}$$

These normalized Fourier coefficients are measured during an ellipsometry measurement and the ellipsometric angles Ψ and Δ are calculated from

$$\begin{aligned} \tan\Psi &= \sqrt{\frac{1+S_1}{1-S_1}} \\ \cos\Delta &= \frac{S_2}{\sqrt{1-S_1^2}} \end{aligned} \tag{2.125}$$

A rotating polarizer ellipsometer is mathematically equivalent to the rotating analyzer ellipsometer, and the ellipsometric angles are obtained by replacing $\tan\phi_P$ by $\tan\phi_A$ in the equations above.

2.5.4 Photo-Elastic Modulator (PEM) based ellipsometry

In PEM-based ellipsometry a photo-elastic modulator is used to modulate the polarization state of the probing beam. In the original design [52], the modulator was placed behind the sample (figure 2.32), but nowadays the modulator is often placed before the sample for practical reasons.

The polarizer (P) sets the polarization ($\phi_P = 45^o$), after which the beam passes through the PEM (M) which modulates the beam along $\phi_M = 0^o$. After reflection from the sample (S) the beam passes through the analyzer (A) which defines the polarization state ($\phi_A = -45^o$) before the beam enters the detector. The entire setup can be described in terms of Jones matrices

$$L_{out} = AR(\phi_A)SR(-\phi_M)MR(\phi_M)R(-\phi_P)PL_{in} = AR(\phi_A)SR(-\phi_M)MR(\phi_M - \phi_P)PL_{in} \tag{2.126}$$

In which we dropped the terms $R(-\phi_A)$ and $R(\phi_P)$ as the only contributing terms will be polarized along the ϕ_A and ϕ_P polarization directions, and substituted $R(\phi_M)R(-\phi_P)$ by $R(\phi_M - \phi_P)$. We are only interested in the relative intensities, so the terms in $1/\sqrt{2}$ (for $R(\phi_A)$ and $R(\phi_M - \phi_P)$) are dropped in the equation of the Jones matrices

$$\begin{pmatrix} E_A \\ 0 \end{pmatrix} = \begin{pmatrix} 1 & 0 \\ 0 & 0 \end{pmatrix}\begin{pmatrix} 1 & 1 \\ -1 & 1 \end{pmatrix}\begin{pmatrix} \sin\Psi e^{i\Delta} & 0 \\ 0 & \cos\Psi \end{pmatrix}\begin{pmatrix} 1 & 0 \\ 0 & e^{i\delta} \end{pmatrix}\begin{pmatrix} 1 & -1 \\ 1 & 1 \end{pmatrix}\begin{pmatrix} 1 & 0 \\ 0 & 0 \end{pmatrix}\begin{pmatrix} 1 \\ 0 \end{pmatrix} \tag{2.127}$$

The resulting transmission through the setup is given by

$$E_A = \sin\Psi e^{i\Delta} + \cos\Psi e^{i\delta} \tag{2.128}$$

from which we can deduce the intensity

$$\begin{aligned} I &= |E_A|^2 \\ &= I_0(1 + \sin 2\Psi(\cos\Delta\cos\delta + \sin\Delta\sin\delta)) \\ &= I_0(1 + S_2\cos\delta + S_3\sin\delta) \end{aligned} \tag{2.129}$$

If we now introduce the time dependence $\delta = F\sin\omega t$ we obtain the expressions for $\sin\delta$ and $\cos\delta$

$$\begin{aligned} \sin\delta = \sin(F\sin\omega t) = 2\textstyle\sum_{m=0}^{\infty} J_{2m+1}(F)\sin[(2m+1)\omega t] \\ \cos\delta = \cos(F\sin\omega t) = J_0(F) + 2\textstyle\sum_{m=1}^{\infty} J_{2m}(F)\cos[2m\omega t] \end{aligned} \tag{2.130}$$

In which the terms J_m are Bessel functions with respect to F. In PEM-based ellipsometry we measure at the modulation frequency ($50kHz$) and its first harmonic ($100kHz$) and drop the higher order terms

$$\begin{aligned} \sin\delta &= 2J_1(F)\sin\omega t \\ \cos\delta &= J_0(F) + 2J_2(F)\cos 2\omega t \end{aligned} \tag{2.131}$$

The applied voltage to the PEM is adjusted such that the retardation is fixed at $F = 138^o$, which sets the values of the Bessel functions to be $J_0(F) = 0$, $2J_1(F) = 1.04$ and $2J_2(F) = 0.86$. This simplifies the analysis tremendously and allows to write the measured intensity from lock-in measurements at $50kHz$ and $100kHz$ as function of the ellipsometric angles Ψ and Δ

$$I(t) = I_0(1 + \sin 2\Psi \sin \Delta[2J_1(F) \sin \omega t] + \sin 2\Psi \cos \Delta[2J_2(F) \cos 2\omega t]) \tag{2.132}$$

In that way, we obtain the final expressions for Ψ and Δ

$$\begin{aligned} \Psi &= \tfrac{1}{2} \sin^{-1} \sqrt{(2J_1(F) \sin \omega t)^2 + (2J_2(F) \cos 2\omega t)^2} \\ \Delta &= \tan^{-1} \tfrac{2J_1(F) \sin \omega t}{2J_2(F) \cos 2\omega t} \end{aligned} \tag{2.133}$$

2.6 Electromagnetic simulations

Electromagnetic simulations are crucial to the understanding of plasmonic metamaterials and were used in the sample design of all structures described in this thesis. Depending on the type of application, we used two different commercial finite-element simulation packages for solving Maxwell's equations.

2.6.1 Lumerical FDTD

Finite-Difference Time Domain simulations were conducted in Lumerical FDTD [53], which is a commercial time-domain finite element solver for Maxwell's equations. The sample structures are defined in 2 or 3 dimensions in the simulation area and the optical properties of the materials are set in terms of the frequency dependent values of the permittivity. A rectangular mesh is defined to divide the structure into discrete cells for which Maxwell's equations are solved in the time domain. A pulse containing the frequencies of interest is applied to the structure and its electromagnetic response is calculated as function of time. The simulation continues to run until the electromagnetic fields have converged to values below the predifined shut-off criterion. The electromagnetic fields at a given frequency are obtained by Fourier analysis of the time-dependent solutions. In that way, the spectral response of any given sample structure can be obtained and compared with experimental results.

2.6.2 Comsol multiphysics

The RF-module of Comsol Multiphysics [54] was used for angle and wavelength dependent optical simulations of the spectroscopic ellipsometry parameters of our plasmonic structures. In the RF-module in Comsol the sample structures are defined in 2 or 3 dimensions in the simulation area and the optical properties of the materials are set in terms of the frequency dependent values of the permittivity. A triangular mesh is defined to divide the structure into discrete cells for which Maxwell's equations are solved. For angle-dependent broadband simulations it is necessary to solve Maxwell's equations in the frequency domain in order to fix the incident angle. Broadband simulations in the time domain would not yield correct solutions as the angle of incidence will be slightly different for each frequency contained in the pulse. In order to extract the correct phase information our sample structures are simulated as periodic structures by means of Bloch boundary conditions which ensures that the phase is properly matched at the periodic boundaries of the simulation space.

2.6.3 Comparison of the two solvers

As outlined in the previous sections, different solvers were used throughout this thesis, depending on the specific application. In general Lumerical FDTD performs better in terms of calculation time and memory requirements, which is why it is often the most convenient choice. However, in case of broadband angle-dependent simulations (for example for ellipsometry measurements), we are restricted to the frequency domain in order to fix the incident angle. Here we want to show one example where the two solvers are compared for the same structure at perpendicular incidence, in order to confirm that they are a reliable reference for the experiments performed. We calculated the reflection and transmission spectra of a hexagonal double fishnet metamaterial structure (discussed in more detail in chapter 3) with a pitch of 500 nm and a hole diameter of 250 nm, as described in figure 3.1. For both simulations the materials are defined in terms of their frequency dependent permittivity which was taken from reference [1] for *Au* and as a constant value for SiO_2 ($\epsilon = 1.96 + 0i$).

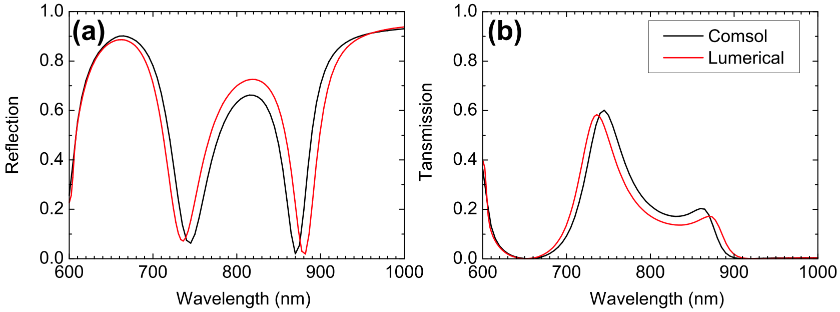

Figure 2.33: *Comparison of simulation results in Lumerical FDTD and Comsol Multiphysics for a hexagonal double fishnet structure. (a) Reflection spectra. (b) Transmission spectra.*

The simulated reflection and transmission spectra for both solvers show good qualitative agreement, which indicates that both solvers provide reliable results for the plasmonic structures investigated in this thesis. The small differences between the obtained solutions can be attributed to different meshing of the structures in both packages. Due to the rectangular shape of the mesh in Lumerical FDTD, we observe staircasing effects at the inclined sidewall angles of the holes, while this effect is much less pronounced for the triangular meshes used in Comsol Multiphysics. The used mesh sizes in this example were larger in Comsol, due to memory and computation time limitations.

Bibliography

[1] P. Johnson and R. Christy, “Optical constants of the noble metals,” *Physical Review B*, vol. 6, no. 12, p. 4370, 1972.

[2] J. D. Jackson, *Classical electrodynamics.* John Wiley and Sons, Inc., 3rd ed., 1999.

[3] I. Freestone, N. Meeks, M. Sax, and C. Higgitt, “The Lycurgus Cup âĂŞ A Roman Nanotechnology,” *Gold Bulletin*, pp. 270–277, 2007.

[4] G. Mie, “Beiträge zur Optik trüber Medien, speziell kolloidaler Metallösungen,” *Annalen der Physik*, vol. 330, pp. 377–445, 1908.

[5] http://www.britishmuseum.org.

[6] R. Wood, “On a remarkable case of uneven distribution of light in a diffraction grating spectrum,” *Proceedings of the Physical Society of London*, vol. 18, p. 269, 1902.

[7] R. Ritchie, E. Arakawa, J. Cowan, and R. Hamm, “Surface-plasmon resonance effect in grating diffraction,” *Physical Review Letters*, vol. 21, no. 22, pp. 1530–1533, 1968.

[8] D. Pines, “Collective energy losses in solids,” *Reviews of modern physics*, vol. 28, pp. 184–196, 1956.

[9] S. A. Maier, *Plasmonics: Fundamentals and Applications.* Springer-Verlag New York Inc., 2007.

[10] A. V. Zayats, I. I. Smolyaninov, and A. a. Maradudin, “Nano-optics of surface plasmon polaritons,” *Physics Reports*, vol. 408, no. 3-4, pp. 131–314, 2005.

[11] E. Kretschmann and H. Raether, “Radiative decay of non radiative surface plasmons excited by light,” *Zeits. fur Naturf.*, vol. 23A, pp. 2135–6, 1968.

[12] A. Otto, “Excitation of nonradiative surface plasma waves in silver by the method of frustrated total reflection,” *Zeits. fur Phys. A*, vol. 216, pp. 398–410, 2005.

[13] S. Lal, S. Link, and N. Halas, “Nano-optics from sensing to waveguiding,” *Nature photonics*, vol. 1, no. 11, pp. 641–648, 2007.

[14] P. Berini, “Long-range surface plasmon polaritons,” *Advances in Optics and Photonics*, vol. 1, no. 3, p. 484, 2009.

[15] P. Neutens, P. Van Dorpe, I. De Vlaminck, L. Lagae, and G. Borghs, “Electrical detection of confined gap plasmons in metalâĂŞinsulatorâĂŞmetal waveguides,” *Nature photonics*, vol. 3, no. 5, pp. 283–286, 2009.

[16] S. A. Maier, M. L. Brongersma, P. G. Kik, and H. A. Atwater, “Observation of near-field coupling in metal nanoparticle chains using far-field polarization spectroscopy,” *Physical Review B*, vol. 65, p. 193408, 2002.

[17] C. Dahmen, B. Schmidt, and G. von Plessen, “Radiation damping in metal nanoparticle pairs.,” *Nano letters*, vol. 7, pp. 318–22, Feb. 2007.

[18] A. V. Kabashin, S. Patskovsky, and A. N. Grigorenko, “Phase and amplitude sensitivities in surface plasmon resonance bio and chemical sensing.,” *Optics express*, vol. 17, no. 23, pp. 21191–204, 2009.

[19] V. G. Kravets, F. Schedin, A. V. Kabashin, and A. N. Grigorenko, “Sensitivity of collective plasmon modes of gold nanoresonators to local environment,” *Optics letters*, vol. 35, no. 7, pp. 956–958, 2010.

[20] B. Luk’yanchuk, N. I. Zheludev, S. A. Maier, N. J. Halas, P. Nordlander, H. Giessen, and C. T. Chong, “The Fano resonance in plasmonic nanostructures and metamaterials.,” *Nature materials*, vol. 9, no. 9, pp. 707–15, 2010.

[21] N. Verellen, Y. Sonnefraud, H. Sobhani, and F. Hao, “Fano resonances in individual coherent plasmonic nanocavities,” *Nano letters*, vol. 9, no. 4, pp. 1663–1667, 2009.

[22] N. Verellen, P. Van Dorpe, C. Huang, K. Lodewijks, G. A. E. Vandenbosch, L. Lagae, and V. V. Moshchalkov, “Plasmon Line Shaping Using Nanocrosses for High Sensitivity Localized Surface Plasmon Resonance Sensing,” *Nano Letters*, vol. 11, no. 2, p. 110125111509056, 2011.

[23] V. G. Veselago, “The electrodynamics of substances with simulataneously negative values of permittivitty and permeability,” *Soviet Physics Uspekhi*, vol. 10, no. 4, pp. 509–514, 1968.

[24] J. Pendry, “Negative refraction makes a perfect lens,” *Physical review letters*, vol. 85, no. 18, pp. 3966–9, 2000.

[25] R. A. Shelby, D. R. Smith, and S. Schultz, “Experimental verification of a negative index of refraction.,” *Science*, vol. 292, no. 5514, pp. 77–9, 2001.

[26] G. Dolling, C. Enkrich, M. Wegener, C. M. Soukoulis, and S. Linden, "Simultaneous negative phase and group velocity of light in a metamaterial.," *Science (New York, N.Y.)*, vol. 312, no. 5775, pp. 892–4, 2006.

[27] D. Smith, S. Schultz, P. Markoš, and C. Soukoulis, "Determination of effective permittivity and permeability of metamaterials from reflection and transmission coefficients," *Physical Review B*, vol. 65, no. 19, pp. 1–5, 2002.

[28] D. R. Smith, D. C. Vier, T. Koschny, and C. M. Soukoulis, "Electromagnetic parameter retrieval from inhomogeneous metamaterials," *Physical Review E*, vol. 71, no. 3, pp. 1–11, 2005.

[29] J. Pendry, "Calculating photonic band structure," *Journal of Physics: Condensed Matter*, vol. 8, p. 1085, 1996.

[30] S. Linden, C. Enkrich, M. Wegener, J. Zhou, T. Koschny, and C. M. Soukoulis, "Magnetic response of metamaterials at 100 terahertz.," *Science (New York, N.Y.)*, vol. 306, no. 5700, pp. 1351–3, 2004.

[31] C. Enkrich, M. Wegener, S. Linden, S. Burger, L. Zschiedrich, F. Schmidt, J. Zhou, T. Koschny, and C. Soukoulis, "Magnetic Metamaterials at Telecommunication and Visible Frequencies," *Physical Review Letters*, vol. 95, no. 20, pp. 5–8, 2005.

[32] N. Liu, H. Guo, L. Fu, S. Kaiser, H. Schweizer, and H. Giessen, "Three-dimensional photonic metamaterials at optical frequencies.," *Nature materials*, vol. 7, no. 1, pp. 31–7, 2008.

[33] N. Liu, H. Liu, S. Zhu, and H. Giessen, "Stereometamaterials," *Nature photonics*, vol. 3, no. March, pp. 157–162, 2009.

[34] M. W. Klein, C. Enkrich, M. Wegener, C. M. Soukoulis, and S. Linden, "Single-slit split-ring resonators at optical frequencies: limits of size scaling.," *Optics letters*, vol. 31, no. 9, pp. 1259–61, 2006.

[35] J. Zhou, T. Koschny, M. Kafesaki, E. Economou, J. Pendry, and C. Soukoulis, "Saturation of the Magnetic Response of Split-Ring Resonators at Optical Frequencies," *Physical Review Letters*, vol. 95, no. 22, 2005.

[36] V. M. Shalaev, W. Cai, U. K. Chettiar, H.-K. Yuan, A. K. Sarychev, V. P. Drachev, and A. V. Kildishev, "Negative index of refraction in optical metamaterials.," *Optics letters*, vol. 30, no. 24, pp. 3356–8, 2005.

[37] G. Dolling, C. Enkrich, M. Wegener, J. Zhou, C. Soukoulis, and S. Linden, "Cut-wire pairs and plate pairs as magnetic atoms for optical metamaterials," *Optics letters*, vol. 30, no. 23, pp. 3198–3200, 2005.

[38] S. Zhang, W. Fan, N. Panoiu, K. Malloy, R. Osgood, and S. Brueck, “Experimental Demonstration of Near-Infrared Negative-Index Metamaterials,” *Physical Review Letters*, vol. 95, no. 13, pp. 1–4, 2005.

[39] G. Dolling, C. Enkrich, M. Wegener, C. M. Soukoulis, and S. Linden, “Low-loss negative-index metamaterial at telecommunication wavelengths.,” *Optics letters*, vol. 31, no. 12, pp. 1800–2, 2006.

[40] G. Dolling, M. Wegener, C. M. Soukoulis, and S. Linden, “Negative-index metamaterial at 780 nm wavelength.,” *Optics letters*, vol. 32, no. 1, pp. 53–5, 2007.

[41] U. K. Chettiar, A. V. Kildishev, H.-K. Yuan, W. Cai, S. Xiao, V. P. Drachev, and V. M. Shalaev, “Dual-band negative index metamaterial: double negative at 813 nm and single negative at 772 nm.,” *Optics letters*, vol. 32, no. 12, pp. 1671–3, 2007.

[42] J. Valentine, S. Zhang, T. Zentgraf, E. Ulin-Avila, D. a. Genov, G. Bartal, and X. Zhang, “Three-dimensional optical metamaterial with a negative refractive index.,” *Nature*, vol. 455, no. 7211, pp. 376–9, 2008.

[43] C. M. Soukoulis and M. Wegener, “Past achievements and future challenges in the development of three-dimensional photonic metamaterials,” *Nature Photonics*, vol. 5, pp. 523–530, 2011.

[44] http://www.biacore.com.

[45] A. Dmitriev, C. Hägglund, S. Chen, H. Fredriksson, T. Pakizeh, M. Käll, and D. S. Sutherland, “Enhanced nanoplasmonic optical sensors with reduced substrate effect.,” *Nano letters*, vol. 8, no. 11, pp. 3893–8, 2008.

[46] J. Anker, W. Hall, O. Lyandres, N. Shah, J. Zhao, and R. Van Duyne, “Biosensing with plasmonic nanosensors,” *Nature materials*, vol. 7, no. 6, pp. 442–453, 2008.

[47] C. Vericat, M. E. Vela, G. Benitez, P. Carro, and R. C. Salvarezza, “Self-assembled monolayers of thiols and dithiols on gold: new challenges for a well-known system.,” *Chemical Society reviews*, vol. 39, no. 5, pp. 1805–34, 2010.

[48] A. Ulman, “Formation and Structure of Self-Assembled Monolayers.,” *Chemical reviews*, vol. 96, no. 4, pp. 1533–1554, 1996.

[49] G. McNay, D. Eustace, W. E. Smith, K. Faulds, and D. Graham, “Surface-enhanced Raman scattering (SERS) and surface-enhanced resonance Raman scattering (SERRS): a review of applications.,” *Applied spectroscopy*, vol. 65, no. 8, pp. 825–37, 2011.

[50] H. Fujiware, *Spectrocopic Ellipsometry: Principle and Applications*. John Wiley and Sons Ltd., 2006.

[51] H. G. Tompkins and E. A. Irene, *Handbook of Ellipsometry*. William Andrew Publishing, 2005.

[52] S. E. Jasperson, S. N.; Schnatterly, "An improved method for high reflectivity ellipsometry based on a new polarization modulation technique," *Review of Scientific Instruments*, vol. 40, no. 6, pp. 761–767, 1969.

[53] "Lumerical fdtd, http://www.lumerical.com/fdtd."

[54] "Comsol multiphysics 3.5a, rf module, http://www.comsol.com."

Chapter 3

Self-assembled negative index materials

3.1 Introduction

In this chapter we show the experimental use of nanosphere lithography (NSL) for fabricating metamaterials with a negative refractive index in the NIR wavelength range. We investigated a specific implementation of the widely studied double fishnet (DFN) metamaterials, consisting of a gold-silica-gold layer stack perforated by a hexagonal array of round holes. Tuning of the hole diameter allows to tailor these self-assembled materials as single- ($Re(\epsilon) < 0$ and $Re(\mu) > 0$) or double ($Re(\epsilon) < 0$ and $Re(\mu) < 0$) negative metamaterials. We benchmarked our self-assembled metamaterials with electron-beam lithography (EBL) based reference structures. The results presented in this chapter were published in *Applied Physics Letters* in the paper "Self-assembled hexagonal double fishnets as negative index materials" [1].
Since the introduction of NIMs by Veselago [2] and the discovery of the possibility of realizing sub-wavelength resolution for imaging devices based on these metamaterials by Pendry [3], many different designs have been proposed to make the "perfect lens" dream reality. A widely studied geometry in the visible and near-infrared (NIR) wavelength range is the DFN structure [4–8], which consists of a stack of MIM layers perforated by a periodic array of holes. The pioneering work by Dolling et al. [5] demonstrated the reversal of the phase velocity, and more recently, also negative refraction was observed in a multilayer fishnet prism structure [9]. The behavior of these NIMs is governed by a magnetic resonance that is excited in the MIM cavities in between the holes and the negative permittivity (ϵ) of the metal layers [10]. At the magnetic resonance, plasmons are excited on the top- and bottom interface of the insulator layer of the MIM cavities, which give rise to a strong magnetic dipole resonance that lowers the effective permeability (μ) which can even reach negative values. Simultaneously negative values for ϵ and μ give rise to a negative value for

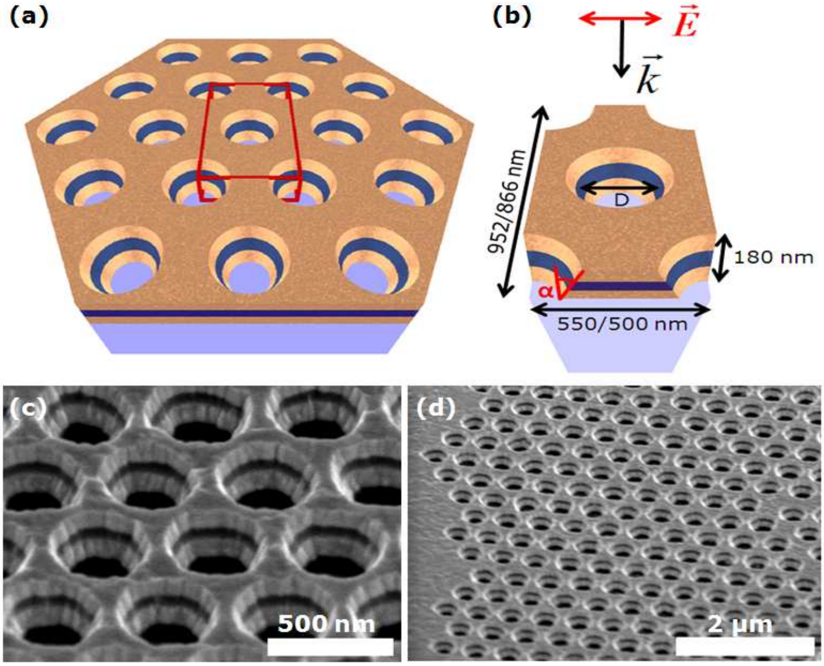

Figure 3.1: *(a) Schematic sample structure. (b) Unit cell for simulations (dimensions for the NSL/EBL samples), D is the diameter and α the $20\,^\circ$ sidewall angle of the holes. Detailed scanning electron microscope picture of the NSL sample (c) and a perfectly ordered domain with some defects (d).*

the refractive index (n). Based on the real parts ($'$) of the effective parameters of the metamaterial, NIMs can be classified as single- or double negative metamaterials (SN-NIMs with $\epsilon' < 0$ and $\mu' > 0$ while $n' < 0$ and DN-NIMs with $\epsilon' < 0$ and $\mu' < 0$ while $n' < 0$). The figure of merit (FOM) for NIMs is defined as the amplitude ratio between the real ($'$) and imaginary ($''$) part of the refractive index ($FOM = |n'/n''|$). Depending on the single- or double negative nature of the NIM, low (SN) or high (DN) values of the FOM are observed. A major drawback of most structures reported to date is that the fabrication involves expensive and low-throughput lithography steps such as EBL or focussed ion beam milling, which limits the potential usage of these metamaterials in large-scale applications.

Here we show that we can circumvent this limitation by using nanosphere lithography (NSL), which allows to create large-area DFN metamaterials consisting of a MIM layer stack perforated by a hexagonal array of holes. The hole pattern is generated using a self-assembled close packed monolayer of 550 nm polystyrene (PS) beads. The pitch of the holes can be tuned by the bead size, while their diameter can be tuned by the bead shrinking step, which allows us to create both SN- and DN-NIMs. Moreover, our fabrication procedure based on ion beam etching (IBE) enables an increase of the overall layer thickness of the NIM, which paves the way to multiple functional layers. The sample geometry is illustrated in figure 3.1. The structure consists of a $Au - SiO_2 - Au$ MIM stack $(60 - 60 - 60nm)$ perforated with a hexagonal array of round holes on top of a glass substrate.

3.2 Sample fabrication

Both our NSL and EBL based samples were fabricated by means of ion beam etching (IBE) through the MIM layer stack, but the definition of the pattern in the e-beam resist layer is done differently. Both fabrication protocols are outlined in the following sections.

3.2.1 Self-assembly samples

Processing steps

The sample fabrication steps for the NSL based samples are outlined in figure 3.2. We start from a glass substrate which is cleaned using H_2SO_4/H_2O_2 3 : 1 for 15 minutes, followed by an oxygen plasma treatment (a). The $Au(60nm)$, $SiO_2(60nm)$ and $Au(60nm)$ MIM layers are sputter deposited onto the subtrate (b). The MET-2D [11] e-beam resist is spin coated at 1300 rpm for 45 seconds and subsequently baked at 120^oC in nitrogen environment for 30 minutes (c). The resist layer is covered by sputter deposition with $10nm$ Au which serves as a protection layer during the PS bead shrinking process (d). The PS beads are deposited by means of spin-coating, which allows to control the self-assembly process. We start from a 0.5% solution of PS beads in water and spin at 300 rpm for 5 minutes, followed by a spinning step at 2000 rpm for 30 seconds to remove the remaining solution from the substrate. The resulting sample structure is covered by a close-packed hexagonal monolayer of PS beads (e). The bead positions are fixed by applying a short annealing step (100^oC for 1 minute) and subsequently they are shrunk using an oxygen plasma treatment. The duration of the etch determines the final bead size and thus the dimensions of the holes in the final sample structure (f). A $5nmTi$ mask is evaporated on top in order to invert the pattern defined by the PS beads (g). The beads are lifted off by dissolving them in toluene (h). The Ti layer now serves as a hard mark for and IBE step that transfers the hole pattern into the Au protection layer (i). Subsequently the hole pattern is transferred into the resist layer by an inductively coupled oxygen plasma etch (j) and into the MIM layer by IBE (k). The remaining resist layer is removed by oxygen plasma treatement (l). The final sample structure consists of a hexagonal lattice of holes with a diameter of 270 nm and a pitch of 550 nm (initial bead diameter).

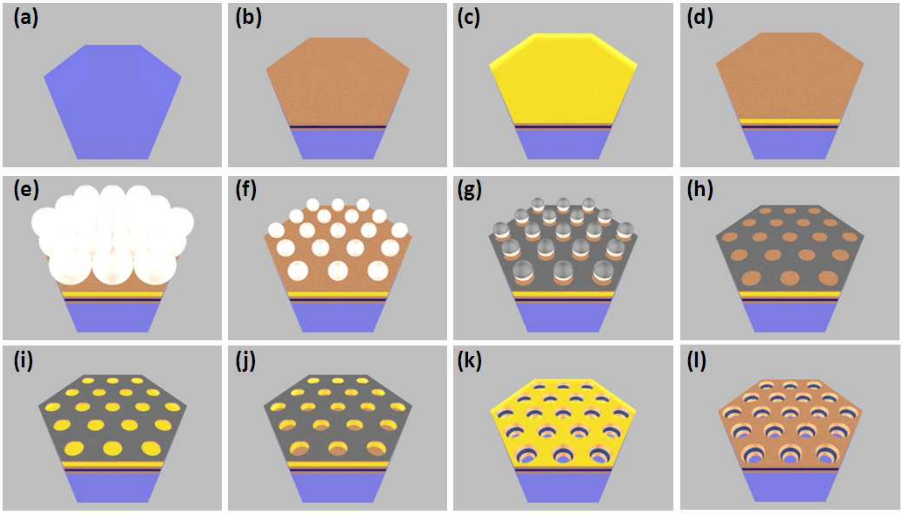

Figure 3.2: *Schematic overview of all the processing steps for the self-assembly samples*

Self assembly of PS beads

The self-assembled hexagonal close-packed monolayers of PS beads were obtained by spin-coating. The spinning speed can be adjusted to control the evaporation rate of the bead solution, which allows us to gradually grow larger monolayers with a single lattice orientation. The self-assembly is governed by the "coffee stain effect" [12, 13], which results in a ring of deposited solid materials as a droplet of liquid containing solid particles is gradually evaporating. When a droplet is formed on a substrate the contact line between the droplet and the substrate can get pinned due to surface roughness or corrugations. If the droplet is pinned and the evaporation process continues over the entire interface between the droplet and the surroundings then the contact line can only maintain its position if a flow of solution from the bulk of the droplet towards the edge is present. This flow will drag any solids (in our case PS beads) dissolved in the fluid along, and deposit them near to the contact line of the droplet. Depending on the shape of the droplet and the evaporation rate of the fluid this effect allows to create monolayers or multilayers of close packed beads (figure 3.3(a)). In our experiments we put a droplet of 0.5% solution of 550 nm PS beads to our substrate, after which the spinning is started at a slow but constant rate. A spot in the center of the substrate will will dry quickly while the droplet gets pinned at a certain distance from the center of rotation, determined by the spinner rotation speed (figure 3.3(b)). The coffee stain effect now results in a stable flow towards the ring of beads that is formed near the contact line of the droplet, which will gradually grow

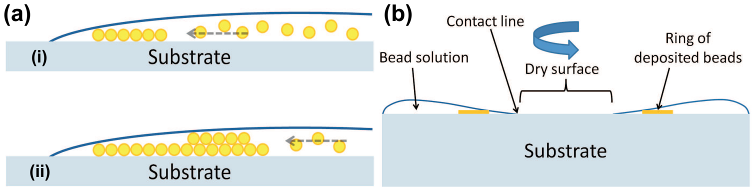

Figure 3.3: *Schematic illustration of the formation of a self-assembled monolayer of PS beads. (a) Coffee-stain effect. (b) Coffee-stain effect for spin-coating.*

into a 2D assembly of hexagonal close packed PS beads.

The resulting DFN sample structures contain large areas up to 100 x 100 μm^2 that show a single lattice orientation and a small number of defects. The total sample areas covered by monolayers of beads (with variable lattice orientations) extend up to milimeter scales. Typical SEM pictures of our samples are shown in figure 3.4 (a), in which we can see some different types of defects (e.g. line defects and missing holes). The inset of panel (a) shows a fast-fourier transform of the SEM picture which illustrates the good quality of the hexagonal lattice structure, while in panel (b) a periodic array of PS beads is shown after the shrinking step.

3.2.2 E-beam samples

The EBL samples were fabricated as benchmark structures for the NSL samples and were designed with a slightly smaller pitch of 500*nm*. The hole sizes were varied between 150*nm* and 300*nm*. The processing steps are identical to those for NSL samples, except for the fact that the NSL steps (d to j in figure 3.2) are replaced by e-beam writing of the pattern and subsequent development of the MET-2D resist.

3.3 Optical characterization

The optical response of the DFN samples was characterized by transmission and reflection measurements on a home-built setup. A Fianium supercontinuum white light source [14] equiped with an acousto-optical tunable filter (AOTF) was used to perform a spectral scan over the wavelength range of interest. The signals were recorded with a silicon detector and were normalized with respect to the reference signal from a glass slide (transmission) and a thick gold layer (reflection).

3.3.1 NSL samples

An overview of the optical response of the self-assembled hexagonal DFN is given in Figure 3.5. The measured and simulated transmission and reflection data (panel

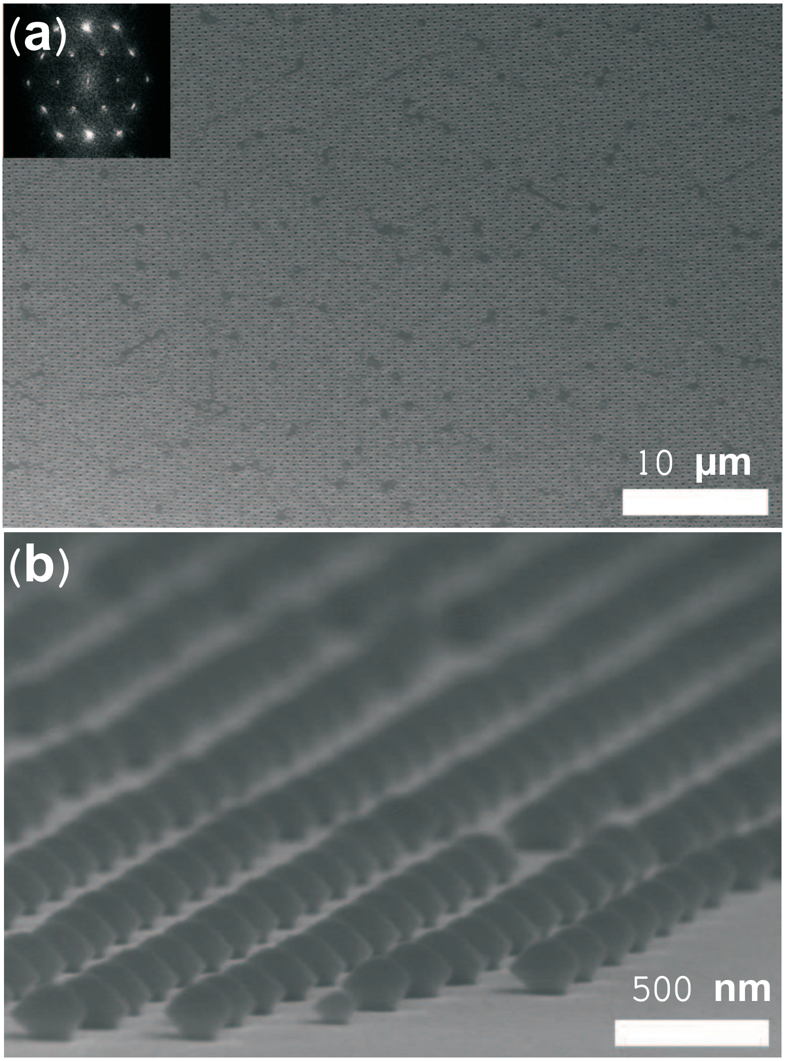

Figure 3.4: *SEM pictures of the sample structures. (a) Large area of DFN sample showing single lattice orientation. (b) Side-view of an array of beads after self assembly and shrinking.*

a) show two pronounced resonances which exhibit good qualitative agreement. The corresponding magnetic field intensity plots (panel b and d) and charge density plots (panel c and e) provide good insight in the nature of these modes. The magnetic field intensity plots show the out-of-plane field component in a cross section of the MIM layer stack. This perpendicular component is a good measure for the excitation of surface plasmons, and illustrates how the first mode at 825 nm (panel b) is confined at the interface between the bottom Au layer and the substrate, while the second mode at 980 nm (panel d) is confined on the top and bottom interfaces of the SiO_2 layer. The corresponding charge density plots show that for the first mode (panel c) parallel and for the second mode (panel e) anti-parallel displacement currents are excited in the Au layers of the MIM cavity. The second mode clearly shows a strong magnetic resonance (panel d) where an out-of-phase magnetic dipole (with respect to the incident plane wave) is excited in the SiO_2 of the MIM cavity, and that gives rise to a strong decrease of the effective μ' of the metamaterial. In combination with the negative ϵ' of the Au layers, this results in a negative value for n'.

The effective material parameters extracted from simulations are summarized in panels f and g (for details see section 3.3.3 and 2.3.2). We first carried out the extraction with the bulk properties of Au [15] and then gradually increased the ϵ'' (up to 3 times the bulk value), to compensate for fabrication imperfections and interface roughness. When increasing ϵ'' of the Au layers, all resonances are damped (decreased amplitude) and broadened while maintaining their spectral position. This damping is also reflected in the extracted effective parameters, which show a decrease in the resonance amplitude as ϵ'' of the Au layers is increased. Smaller absolute values for n' and larger values for n'' are obtained, resulting in a decrease of the FOM (panel f). The resonances in the effective ϵ' and μ', are also decreased in amplitude (panel g). When comparing the measured spectra with simulation data, we clearly observe that for the first resonance, the bulk damping coefficients give us the best fit, which can be explained by its nature. The mode is dominated by the bottom hole cavity and plasmons excited at the interface between the substrate and the bottom Au layer (panel b). Since the substrate roughness is much smaller than the roughness of the sputtered MIM layers, we don't expect much additional damping on top of the bulk material properties [16]. For the magnetic resonance on the other hand, we see more damping in the measurement than for the simulation with the bulk Au parameters (1X). When increasing ϵ'' (2X and 3X) in the simulations, we clearly see the modes becoming less pronounced, which is most apparent in the transmission spectrum near the magnetic resonance. The step-like behavior is observed in all simulations, but the sharp edge that is observed for the bulk ϵ'' becomes less steep as the damping is increased. Therefore, the step-like behavior in the transmission spectrum is a good measure to determine the importance of damping, by fitting the measured spectrum to the simulated spectra with different values of the ϵ''. In practice, we search for qualitative correspondence of the shape of the magnetic resonance to determine the most appropriate damping. Based on experimental results for various hole sizes, we suggest that doubling the ϵ'' of the Au layers is sufficient

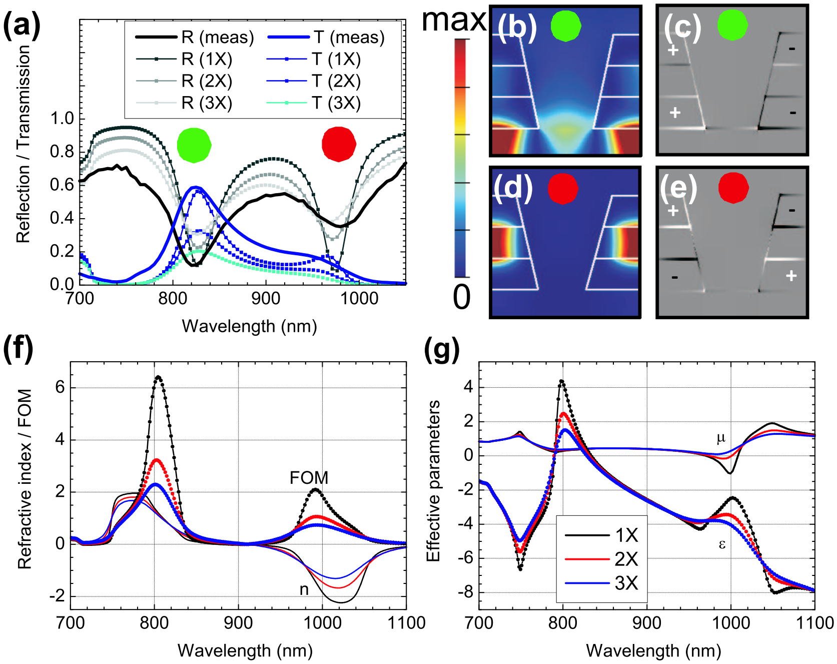

Figure 3.5: *Measurements and simulations for a self-assembled hexagonal DFN. (a) Measured (full lines) and simulated (dotted lines) reflection and transmission spectra with different damping.* $(1, 2, 3X$ *= number of times the bulk imaginary* ϵ *of Au). (b) and (d) Show the magnetic field intensity plot at the 825 and 980 nm resonance respectively. (c) and (e) Show the charge density plot at the 825 and 980 nm resonance respectively. (f) Simulated real part of n and the FOM for different damping in the Au layers. (g) Simulated effective parameters:* ϵ' *and* μ' *for different damping in the Au layers.*

to account for the increased damping due to surface roughness and the nanoscale dimensions of the metamaterial. Again, the increased damping can be understood from the nature of the resonance. At the magnetic resonance, plasmons are excited on the top and bottom of the SiO_2 spacer, which are more prone to surface roughness, as these are created by sputter deposition [16].

3.3.2 EBL samples

An overview of the measured and simulated transmission and reflection spectra is presented in figure 3.6 for a batch of hexagonal DFNs, fabricated by EBL, with $150nm \leq D \leq 300nm$ and a pitch of 500 nm. The measured spectra show good agreement to the simulated spectra, in which bulk material parameters were used. For all samples, the two main modes of the structure can be clearly observed, and show the expected wavelength shifts with respect to the diameter. The first resonance between 750 nm to 800 nm shows a red-shift with increasing diameter, which is related to the cut-off of the hole transmission. As the hole size is decreased, the resulting decrease in transmission is smaller for shorter than for longer wavelengths, due to the non-linear dependence of the transmission beyond the cut-off frequency of the hole waveguide [17]. The second mode between 900 to 950 nm shows a blue-shift with increasing diameter. As this mode is related to the excitation of plasmons [10] on the interfaces of the SiO_2 layer, the blue shift with increasing diameter can be attributed to decreasing MIM cavity length.

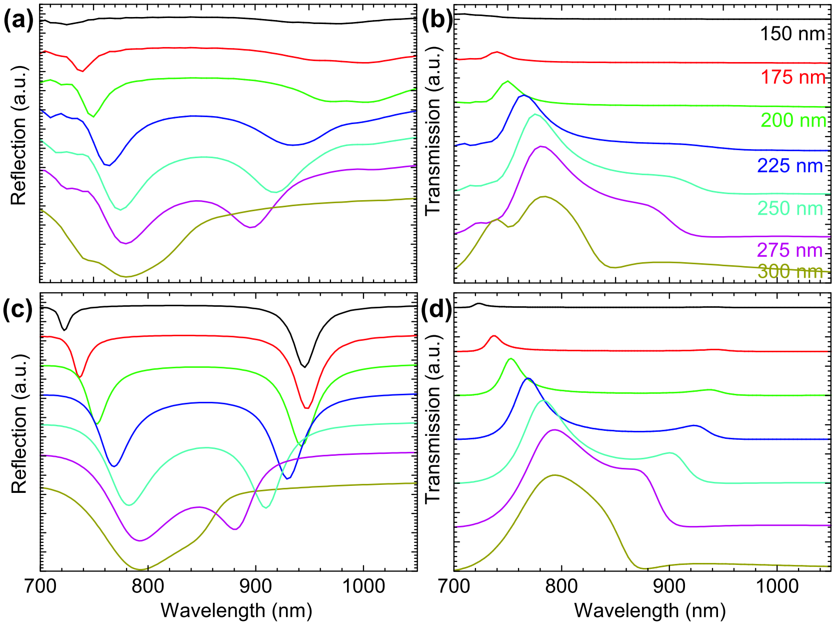

Figure 3.6: *Reflection and transmission spectra for EBL based hexagonal DFNs with* $150nm \leq D \leq 300nm$*. Measured reflection (a) and transmission (b). Simulated reflection (c) and transmission (d).*

All samples shown in figure 3.6 exhibit negative values for n' around the magnetic resonance. The strength of the magnetic resonance is different for the various hole sizes, and the strongest resonance is observed for a diameter of 250 nm, which is the only sample that exhibits DN behavior (using double ϵ'').

When we compare the measured spectra for NSL samples (figure 3.5 (a)) and EBL samples (figure 3.6 (a and b)), we observe some minor differences. Both sample types show broadening of the measured resonances with respect to the simulated spectra, but the broadening is more pronounced for NSL samples (Q-factor of about 15 versus 20 for EBL). This can be attributed to line defects and missing holes, but also to size variations in the PS beads and imperfect hole shapes due to the shrinking step.

3.3.3 Simulations and effective parameter retrieval

The optical response of our samples was modeled using finite-difference time domain simulations [18]. A rectangular unit cell with periodic boundary conditions was used (figure 3.1 (a and b)). The complex fields on the top and bottom surface of the MIM trilayer structure were averaged over the unit cell (homogenization) in order to extract the effective material parameters, taking into account the bianisotropy (sidewall angle of holes) of the samples (see section 2.3.2). In that way, the complex effective parameters (n, Z, ϵ and μ) and the FOM were calculated. Figure 3.7 shows an overview of the effective parameters for a hexagonal double fishnet sample with a 250 nm hole diameter and a pitch of 500 nm. The imaginary part of the permittivity of Au was taken twice the bulk value [15]. Panel a provides an overview of the far-field reflection and transmission data for both sides of incidence. Clearly the transmission through the fishnet layers is identical for both propagation directions, while the reflection spectra show a significant difference. The extracted values for the refractive index (panel b) and FOM (panel c) show the different values for top incidence (black), bottom incidence (red) and the effective value (blue) for the bianisotropic case. For the impedance (panel d), the values obtained without bianisotropy correction for top incidence (black full line) and bottom incidence (red full line) clearly coincide with the bianisotropy-corrected values calculated for top incidence (black dots) and bottom incidence (red dots). Using these 2 values for the impedance together with the bianisotropy-corrected extracted refractive index, results in the effective permittivity (panel e) and permeability (panel f) for the bianisotropic samples, which are slightly different from the isotropic case. In panels e and f, the full lines correspond to the isotropic case, dotted lines correspond to the bianisotropic case while black corresponds to the top incidence cases and red to the bottom incidence cases.

3.4 Conclusions

We have shown the feasibility to use NSL for the fabrication of large area metamaterials that exhibit a negative value of the refractive index in the NIR wavelength range. We compared the NSL-based samples with EBL-based reference samples which indicated that the self-assembled samples show similar performance. Depending on the hole diameter, the metamaterials can be tuned to be single- or double-negative in nature. Moreover, we have shown that the damping of the resonances due to the nanoscale structure and fabrication imperfections seems to be smaller compared to earlier works, and should in our case only be taken twice as large as the bulk permittivity for Au in order to allow extraction of effective material parameters.

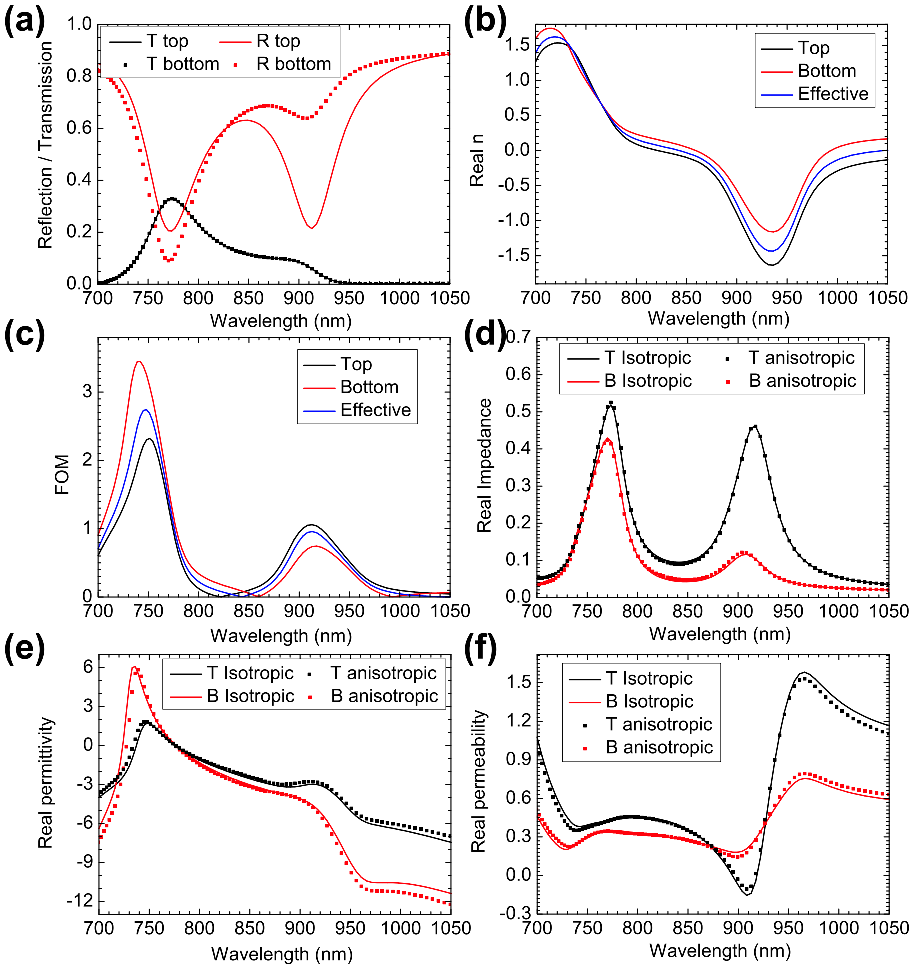

Figure 3.7: *Overview of the extracted effective material parameters without and with bi-anisotropy correction.*

Bibliography

[1] K. Lodewijks, N. Verellen, W. Van Roy, V. Moshchalkov, G. Borghs, and P. Van Dorpe, "Self-assembled hexagonal double fishnets as negative index materials," *Applied Physics Letters*, vol. 98, no. 9, p. 091101, 2011.

[2] V. G. Veselago, "The electrodynamics of substances with simulataneously negative values of permittivitty and permeability," *Soviet Physics Uspekhi*, vol. 10, no. 4, pp. 509–514, 1968.

[3] J. Pendry, "Negative refraction makes a perfect lens," *Physical review letters*, vol. 85, no. 18, pp. 3966–9, 2000.

[4] G. Dolling, C. Enkrich, M. Wegener, C. M. Soukoulis, and S. Linden, "Low-loss negative-index metamaterial at telecommunication wavelengths.," *Optics letters*, vol. 31, no. 12, pp. 1800–2, 2006.

[5] G. Dolling, C. Enkrich, M. Wegener, C. M. Soukoulis, and S. Linden, "Simultaneous negative phase and group velocity of light in a metamaterial.," *Science*, vol. 312, no. 5775, pp. 892–4, 2006.

[6] G. Dolling, M. Wegener, C. M. Soukoulis, and S. Linden, "Negative-index metamaterial at 780 nm wavelength.," *Optics letters*, vol. 32, no. 1, pp. 53–5, 2007.

[7] U. K. Chettiar, A. V. Kildishev, H.-K. Yuan, W. Cai, S. Xiao, V. P. Drachev, and V. M. Shalaev, "Dual-band negative index metamaterial: double negative at 813 nm and single negative at 772 nm.," *Optics letters*, vol. 32, no. 12, pp. 1671–3, 2007.

[8] S. Xiao, U. K. Chettiar, A. V. Kildishev, V. P. Drachev, and V. M. Shalaev, "Yellow-light negative-index metamaterials.," *Optics letters*, vol. 34, no. 22, pp. 3478–80, 2009.

[9] J. Valentine, S. Zhang, T. Zentgraf, E. Ulin-Avila, D. A. Genov, G. Bartal, and X. Zhang, "Three-dimensional optical metamaterial with a negative refractive index.," *Nature*, vol. 455, no. 7211, pp. 376–9, 2008.

[10] A. Mary, S. Rodrigo, F. Garcia-Vidal, and L. Martin-Moreno, "Theory of Negative-Refractive-Index Response of Double-Fishnet Structures," *Physical Review Letters*, vol. 101, no. 10, pp. 2–5, 2008.

[11] "Met-2d (xp5271i), dow corning corporation, www.dowcorning.com."

[12] R. Deegan, O. Bakajin, and T. Dupont, "Capillary flow as the cause of ring stains from dried liquid drops," *Nature*, vol. 389, no. 6653, pp. 827–829, 1997.

[13] T. P. Bigioni, X.-M. Lin, T. T. Nguyen, E. I. Corwin, T. A. Witten, and H. M. Jaeger, "Kinetically driven self assembly of highly ordered nanoparticle monolayers.," *Nature materials*, vol. 5, no. 4, pp. 265–70, 2006.

[14] "Fianium sc-450, http://www.fianium.com."

[15] P. Johnson and R. Christy, "Optical constants of the noble metals," *Physical Review B*, vol. 6, no. 12, p. 4370, 1972.

[16] P. Nagpal, N. C. Lindquist, S.-H. Oh, and D. J. Norris, "Ultrasmooth patterned metals for plasmonics and metamaterials.," *Science (New York, N.Y.)*, vol. 325, no. 5940, pp. 594–7, 2009.

[17] K. L. van der Molen, F. B. Segerink, N. F. van Hulst, and L. Kuipers, "Influence of hole size on the extraordinary transmission through subwavelength hole arrays," *Applied Physics Letters*, vol. 85, no. 19, p. 4316, 2004.

[18] "Lumerical fdtd, http://www.lumerical.com/fdtd."

Chapter 4

Phase-sensitive measurements of LSPRs for improved sensing applications

4.1 Introduction

In this chapter we investigate the phase of localized surface plasmon resonances for sensing applications. In many of the existing applications only the intensity of the reflected or transmitted signals is taken into account, while the phase information is ignored. At the center frequency of a (localized) surface plasmon resonance, the electron cloud makes the transition between in- and out-of-phase oscillation with respect to the incident wave. Here we show that this information can experimentally be extracted by performing phase-sensitive measurements, which result in linewidths that are almost one order of magnitude smaller than those for intensity based measurements. As this phase change is an intrinsic property of a plasmon resonance, this opens up many possibilities for boosting the figure of merit (FOM) of refractive index sensing by taking into account the phase of the plasmon resonance. We experimentally investigated this for two model systems: randomly distributed gold nanodisks and gold nanorings on top of a continuous gold layer and a dielectric spacer and observed FOM values up to 8.3 and 16.5 for the respective nanoparticles. The results presented in this chapter were published in *Nano Letters* in the paper "Boosting the Figure-Of-Merit of LSPR-Based Refractive Index Sensing by Phase-Sensitive Measurements" [1].

The collective oscillations of the free electrons in noble metals have been studied extensively over the past decades for a wide variety of applications. Both propagating surface plasmon polariton (SPP) and localized surface plasmon resonance (LSPR) modes posess very interesting properties, with applications in sensing (refractive index sensing [2–7], SERS [8]), metamaterials [9], waveguiding [10, 11] and enhanced coupling to active semiconductor components (e.g. photovoltaic cells [12], SPASERs [13, 14]). Refractive index sensing is by far the most studied application and allows label-free and real-time detection of changes in the dielectric environment of the plasmonic nanostructures. Moreover, by functionalizing the nanostructures, the sensors can be made specific to a particular molecule. In former works, research groups have followed various paths in order to optimize the nanostructure designs such that higher sensitivities, figures of merit and lower detection limits (DLs) can be achieved. Plasmon resonances are extremely sensitive to the refractive index of the surrounding medium. With increasing values of the refractive index the LSPR shows a red shift, and the magnitude of this shift divided by the change in refractive index is defined as the sensitivity ($d\lambda/dn$). The figure of merit of a plasmon resonance is given by the ratio between the sensitivity and the width of the resonance peak ($FOM = (d\lambda/dn)/fwhm$), and high values of the FOM are an indication for good sensor performance. For structures with increased FOMs, the DLs (smallest refractive index change which can be measured) can be reduced. Recently a lot of progress has been made in line width tuning (Fano resonances, sub-radiance) in order to obtain higher FOMs [2, 3, 15–19].

In any resonant system, a pronounced transition from in- to out-of-phase oscillation is observed around the center frequency of the resonance with respect to the driving force. This is also the case for (localized) surface plasmon resonances, where the electron cloud makes the transition between in- and out-of-phase oscillation with respect to the incident wave [19]. Also for conventional SPR sensing, it was shown that these phase changes can be probed by phase sensitive measurements, which show a much smaller spectral/angular footprint compared to their intensity based counterparts [4, 5]. Here we show that using standard spectroscopic ellipsometry measurements, we can measure similar phase jumps around the center frequency of localized surface plasmon resonances. For our two model systems, we investigated the angle- and polarization dependent reflection spectra and the phase difference between P- and S-polarized waves, using lock-in measurements.

4.2 Sample fabrication

The gold nanoparticles were fabricated by nanosphere lithography (NSL) using a self-assembled monolayer of randomly distributed polystyrene (PS) beads. The formation of the bead monolayer is based on the protocol described in reference [20].

4.2.1 Self-assembled monolayers of PS beads

The substrates are treated with an oxygen plasma in order to make the surface hydrophilic. A droplet of 0.2% wt polydiallyldimethylammonium (PDDA) solution is applied on the surface for 30 seconds after which the sample is rinsed under a water flow for 30 seconds and dried under a nitrogen flow. A self-assembled monolayer

(SAM) of PDDA is left on the substrate, which results in a positively charged surface. Subsequently a droplet of 0.2% wt solution of PS beads functionalized with sulfate groups is applied on the surface for 2 minutes after which the sample is rinsed under a water flow for 30 seconds and dried under a nitrogen flow. The negative charges on the sulfate groups results in electrostatic repulsion between the PS beads while they are attracted to the positively charged substrate. As a result the beads form a monolayer on the substrate with a fixed average inter-particle distance (center-to-center) which is about 2.5 times the PS bead diameter.

4.2.2 Gold nanorings

The gold nanorings are illustrated in figure 4.1 and have an inner diameter of 100 nm, an outer diameter of 150 nm and a height of 60 nm. The average interparticle distance (center-to-center) is 250 nm.

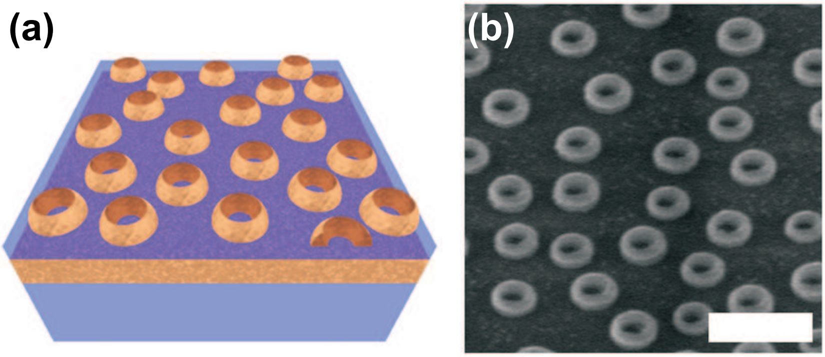

Figure 4.1: *(a) Schematic sample structure structure for a* $1\mu m^2$ *sample area of gold nanorings. (b) Side view SEM picture. Scale bar 500 nm.*

The sample fabrication steps for the nanoring samples are outlined in figure 4.2. We start from a glass substrate which is cleaned using H_2SO_4/H_2O_2 3 : 1 for 15 minutes, followed by an oxygen plasma treatment (a). The $Au(100nm)$ and $SiO_2(50nm)$ layers are sputter deposited onto the subtrate (b). The SAM layer of 100 nm PS beads is deposited according to the procedure described in section 4.2.1 (c). The beads are covered with a 30 nm Au layer by sputter deposition (d). An ion beam etching step is applied in order to open up the top aperture of the rings and to remove the gold in between the particles (e). As a final step the PS beads are etched in oxygen plasma (f).

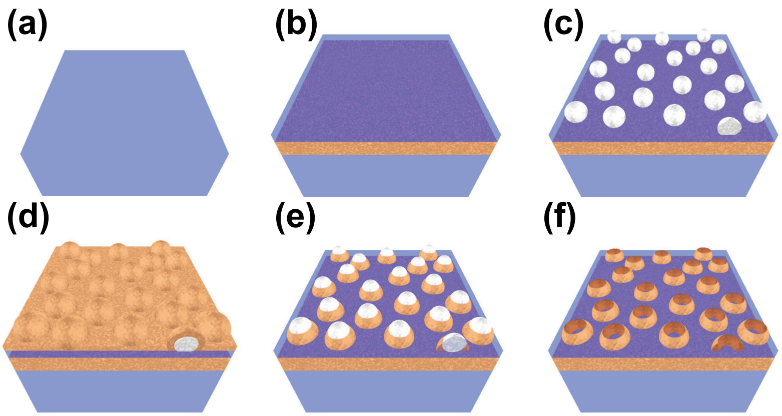

Figure 4.2: *Fabrication protocol of gold nanorings.*

4.2.3 Gold nanodisks

The gold nanorings are illustrated in figure 4.3 and have a diameter of 140 nm and a height of 60 nm. The average interparticle distance (center-to-center) is 350 nm.

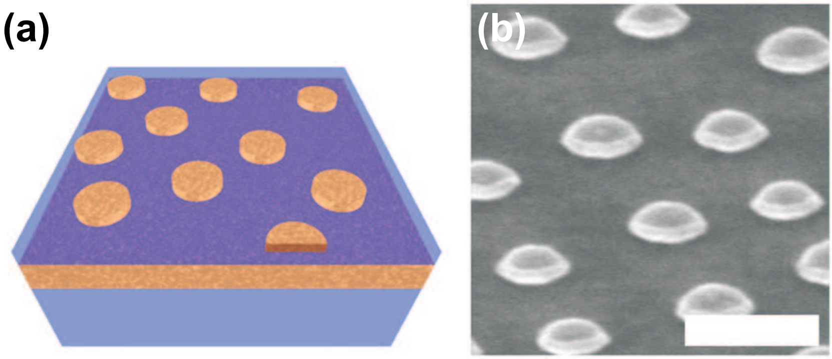

Figure 4.3: *(a) Schematic sample structure structure for a* $1\mu m^2$ *sample area of gold nanodisks. (b) Side view SEM picture. Scale bar 500 nm.*

The sample fabrication steps for the nanodisk samples are outlined in figure 4.4. We start from a glass substrate which is cleaned using H_2SO_4/H_2O_2 3 : 1

for 15 minutes, followed by an oxygen plasma treatment (a). The $Au(100nm)$ and $SiO_2(50nm)$ layers are sputter deposited onto the subtrate (b). A 200 nm PMMA e-beam resist layer is spincoated on top (c). The SAM layer of 140 nm PS beads is deposited according to the procedure described in section 4.2.1 (d). A 10 nm Au layer is evaporated on top in order to create a shadow mask of holes (e). The beads are removed by tape stripping (f). The hole pattern is transfered into the PMMA layer by oxygen plasma etching (g). 30 nm of Au is evaporated forming disks in the holes (h). The PMMA layer is lifted off leaving the disk particles on the substrate (i).

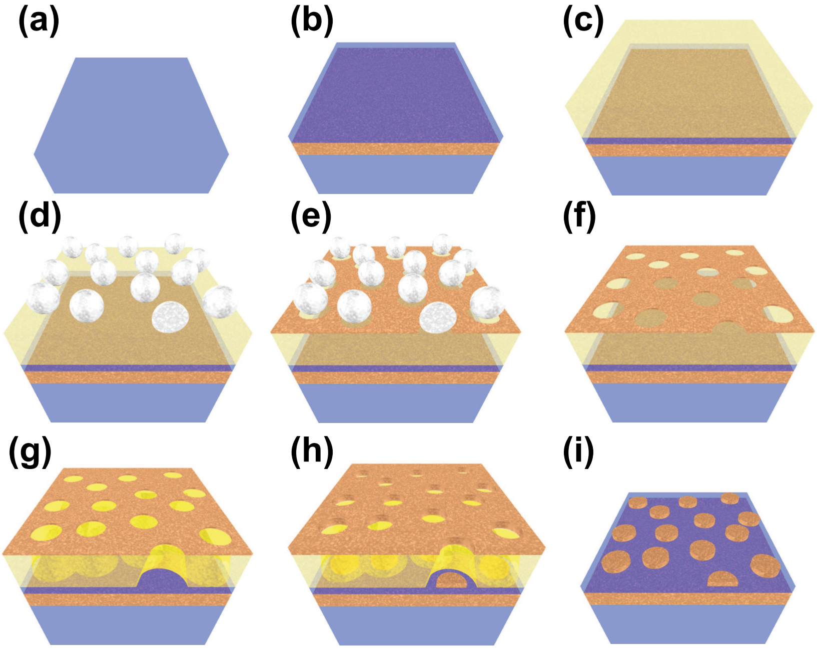

Figure 4.4: *Fabrication protocol of gold nanodisks.*

4.3 Results and discussion

We investigated localized surface plasmon resonances in randomly distributed gold nanoparticles on top of a continuous gold layer and a dielectric spacer by spectroscopic ellipsometry. By scanning the angle of incidence, the electric dipole resonances in the nanoparticles become spectrally detuned for both polarization states. Both for P- and S-polarized waves, the electric dipole (figure 4.5 c and f) in the nanoparticle couples to an electric quadrupole (figure 4.5 a, b, e) in the combined nanoparticle/gold film complex, which gives rise to an induced magnetic dipole perpendicular (figure 4.5 a, d, g) to the electric dipole in the nanoparticle.

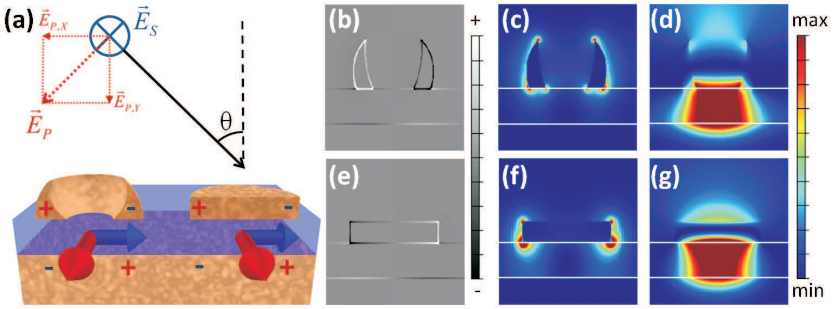

Figure 4.5: *Simulation overview of the plasmonic modes for the respective nanoparticles. (a) Schematic overview of the polarization states and quadrupole charge distribution for P-polarized waves. The 3D arrows indicate the magnetic dipole for P (red) and S (blue). (b and e) Charge distribution at the electric dipole resonance for rings and disks. The electric dipole couples to a quadrupole mode in the combined nanoparticle/gold film complex. (c and f) Electric field intensity at the electric dipole resonance for rings and disks. (d and g) Induced magnetic dipole at the electric dipole resonance for rings and disks.*

4.3.1 Optical characterization

The angle dependent spectroscopic ellipsometry measurements were performed using a commercial GESP5 [21] ellipsometer and a home-built setup based on a photoelastic modulator (PEM) [22]. For the GESP5 setup, the polarization of the incident beam is modulated between P and S by a rotating polarizer, while for the PEM-based setup, the polarization is modulated between linear and left- and right- circular polarization states. Both measurement setups have different signal-to-noise ratios in different spectral ranges, so depending on the spectral position of the LSPR we choose the setup that performs best. All spectroscopic ellipsometry measurements shown here were performed with the GESP5 setup, except for the refractive index sensing measurements on gold rings which were performed on the home-built PEM-based setup.

The phase information is extracted by performing lock-in measurements at the modulation frequency. The measured quantities tan(Ψ) and cos(Δ) are related by the main equation of ellipsometry:

$$\begin{aligned} \rho = \frac{R_P}{R_S} &= \tan(\Psi)\exp(i\Delta) \\ &= \tan(\Psi)(\cos(\Delta) + i\sin(\Delta)) \end{aligned} \tag{4.1}$$

and represent the amplitude reflection ratio between P and S (tan(Ψ)) and the phase difference between the reflected signals Δ for the 2 polarizations (reflected in the cos(Δ) value). In that way, the angle dependence of the plasmon resonances and the extremely narrow phase changes at their central frequency could be probed experimentally. By properly designing the nanoparticle shape and density, the interparticle coupling can be tuned resulting in two spectrally slightly detuned resonances for P- and S-polarized incident light. An overview of the angle dependent measurements on the nanorings is given in figure 4.6. Panels a and b show the intensity based reflection spectra for P- and S-polarized incident waves, while panels c and d show the reflection ratio tan(Ψ) and the phase difference cos(Δ) between the two polarization states. With increasing incident angle, the P-resonance shows a blue shift, while the S-resonance shows a red shift. These resonance shifts are reflected in the phase sensitive ellipsometry measurements, in which at the center frequency of the plasmon resonances a minimum and maximum in the reflection ratio (panel c), and a pronounced phase difference between P and S (panel d) is observed.

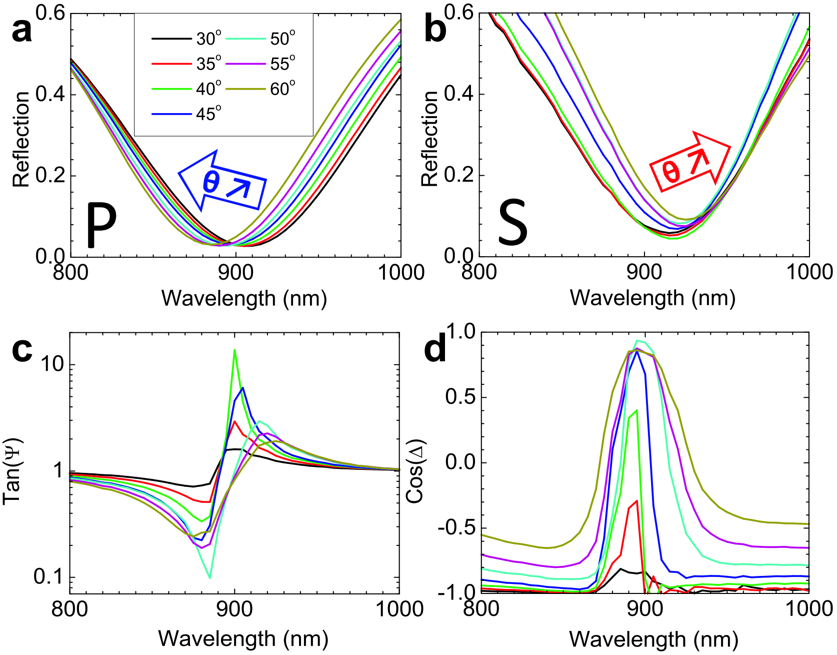

Figure 4.6: *Angle dependent measurement data for gold nanorings. (a) and (b) Measured intensity based reflection spectra for P- and S-polarizations. (c) Measured values of* tan(Ψ)*, the amplitude reflection ratio between P- and S-polarizations. (d) Measured values of* cos(Δ)*, with* Δ *the phase difference between both polarization states.*

Similar measurements were performed for gold nanodisks, which have comparable sizes to the rings, but are less densely packed due to different fabrication parameters. An overview of the angle dependent measurements for both polarizations is given in figure 4.7. Both for P- (panel a) and S-polarized (panel b) waves, the electric dipole resonances are blue shifted compared to the nanorings. With increasing angle of incidence, for the P-polarization, a minor blue shift is observed, while the S-resonance shows a pronounced red shift. Both resonances show much more spectral overlap compared to the nanorings, which results in a totally different behavior in their reflection ratio tan(Ψ) (panel c). For small angles of incidence we observe a maximum in the reflection ratio at shorter wavelengths, while at larger angles of incidence the S-resonance shifts to longer wavelengths with respect to the P-resonance, resulting in similar spectra as for gold nanorings. If we take a closer look at the phase difference between P and S (panel d), we observe again two phase jumps, one for each polarization state, which are smaller in magnitude compared to the nanorings. These smaller phase jumps can be attributed to the increased spectral overlap for the two polarization states, which results in a smaller overall phase difference.

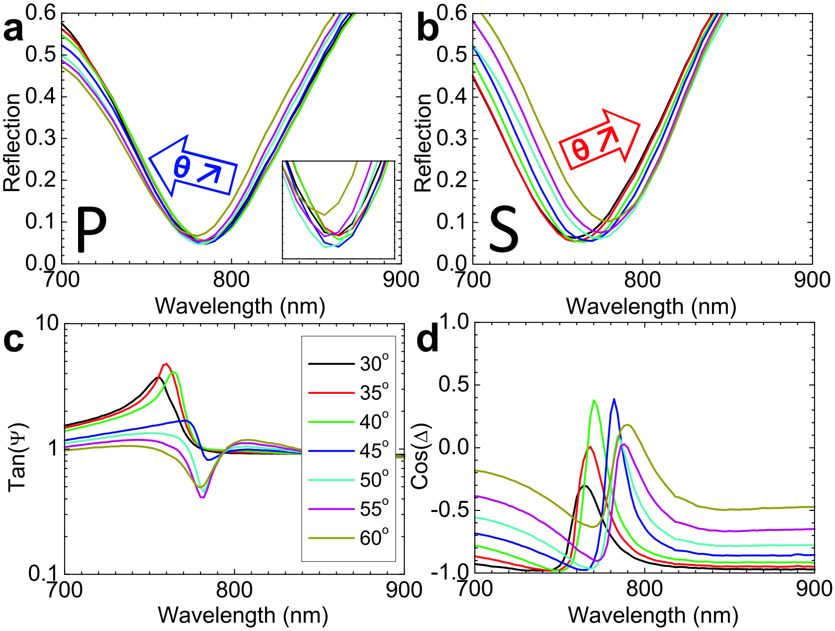

Figure 4.7: *Angle dependent measurements on gold nanodisks. Reflection spectra for P- (a) and S-polarization (b). (c) Reflection ratio* tan(Ψ)*. (d) Phase difference* cos(Δ).

4.3.2 Simulations of ellipsometric parameters

The angle- and polarization dependent optical response of the nanoring samples was simulated using Comsol multiphysics [23]. An overview of the simulated spectra is given in figure 4.8. The different spectra were calculated for a square lattice of rings with a pitch of 250 nm (matched to the experimental average inter-particle distance). By using periodic (Bloch) boundary conditions and scanning all the angles involved for both polarizations, the angle dependent reflection and the ellipsometric parameters were extracted. The reflected waves for P- and S-polarized waves were recorded and their electric and magnetic fields were averaged out over one unit cell, allowing to extract the amplitude and phase in order to evaluate the values of $\tan(\Psi)$ and $\cos(\Delta)$. We used a periodic particle arrangement in order to take into account the interactions between the neighboring particles, as these determine the spectral shifts of the modes for P and S with changing angles of incidence. Simulations on single particles would not include these interactions, and finite element simulations on a random particle distribution were not possible due to computational limitations. A nice qualitative agreement is obtained, where the P-resonance and S-resonances show the blue shift (panel a) and red shift (panel b) respectively, similar to the experimental data. Contrary to the measured data, the minimum of the reflection dip shows a decrease with increasing angle of incidence. This behavior can be attributed to the random particle distribution in our samples, that gives rise to inhomogeneous broadening, which is most pronounced for large angles of incidence due to increasing spot sizes. This explains why the maxima and minima in the reflection ratio ($\tan(\Psi)$) are not observed at the largest angle of incidence in the experimental spectra, contrary to the simulated data (panel c). Interestingly, if we compare the magnitude of the phase difference between P and S, we clearly observe that the largest phase changes are observed at the maxima and minima in the reflection ratio, which occur around 45^o in the experiments (figure 4.6(d)), and at 75^o in simulations (figure 4.8(d)).

Note that we didn't show similar simulations for the disks, as simulations with larger pitch (350 nm) also show grating SPP modes on the bottom gold layer, which are not present in our random samples. We will discuss periodic disk arrays and the associated grating modes in detail in chapter 5.

4.3.3 Inter-particle coupling mechanism

For the two nanoparticle geometries, we have illustrated that we can clearly identify the phase changes at the LSPR frequency for the different polarization states. Now we want to take a closer look at the plasmon modes involved and the dominating inter-particle coupling mechanism. For both polarization states an electric dipole is excited in the nanoparticle (figure 4.5 c and f), which shows a very broad linewidth (around 140 nm for rings and 100 nm for disks). This electric dipole resonance couples directly (P-polarization) or capacitively (S-polarization) to an electric quadrupole mode in the combined nanoparticle/gold film complex (figure 4.5 b and e). The electric quadrupole mode also results in an induced magnetic dipole moment (figure

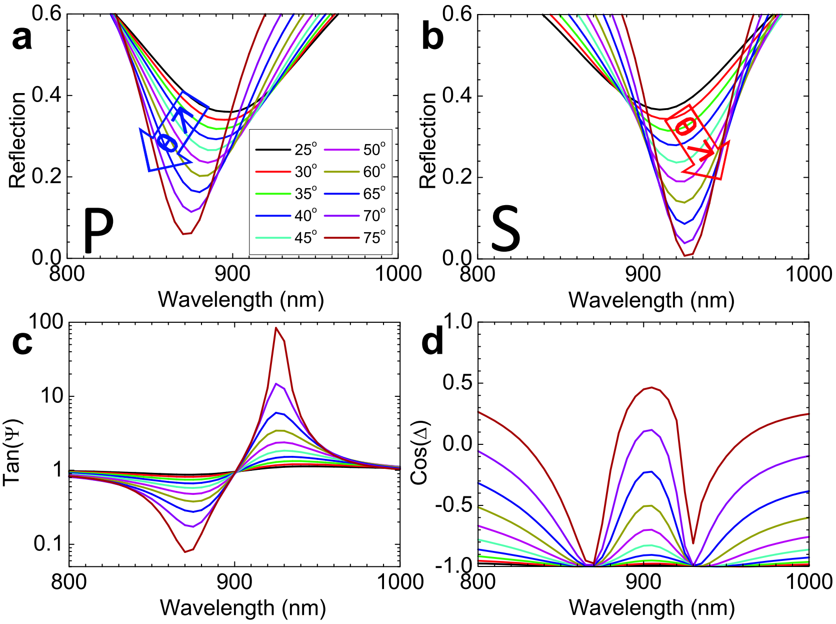

Figure 4.8: *Angle dependent simulation data for a periodic array of gold nanorings. (a) and (b) Simulated intensity based reflection spectra for P- and S-polarizations. (c) Simulated values of* $\tan(\Psi)$*, the reflection ratio between P- and S-polarizations. (d) Simulated values of* $\cos(\Delta)$*, with* Δ *the phase difference between both polarization states.*

4.5 d and g), which is aligned perpendicular to the electric dipole in the nanoparticles. By varying the angle of incidence and the polarization, the phase retardation is scanned, resulting in different coupling efficiencies to the plasmon modes and differences in the inter-particle coupling strength, which is reflected in spectral shifts of the plasmon resonances [24]. The inter-particle coupling is mediated by electric dipole/quadrupole coupling and magnetic dipole coupling, both in the longitudinal and transversal direction. If the scattered fields of the nanoparticle are in phase (out of phase) with the incident wave in the neighboring particles, the local resonance will be enhanced (opposed) and show a blue (red) shift. We investigated the inter-particle coupling by numerical simulations on 1D linear arrays of the respective nanoparticles and were able to identify the dominating interparticle coupling mechanisms for the different polarization states. For this study in Lumerical FDTD [25] we used perpendicular incidence and varied the pitch, such that the excitation efficiency would be similar for the LSPR modes, but the inter-particle coupling would be different. An overview of the simulations is given in figure 4.9. The periodic 1D particle array is constructed by using periodic boundary conditions in the horizontal direction and perfectly matched layers in the vertical direction (located far from the particle array). The extracted spectral positions for the electric dipole resonances are shown in panel b and show qualitative agreement with the experimental shifts for rings (figure 4.6) and disks (figure 4.7).

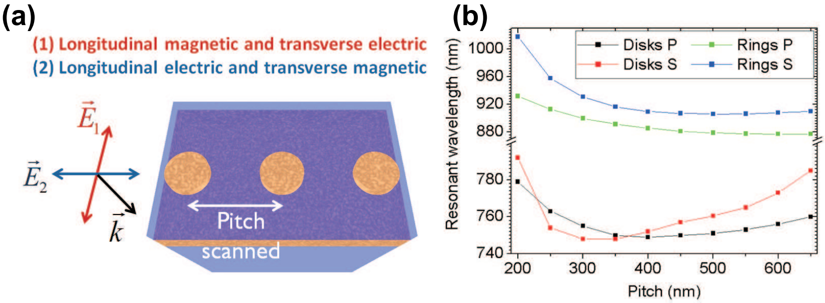

Figure 4.9: *(a) Overview of the simulation structure and polarization states for the mode coupling studies in 1D linear arrays of disks and rings. (b) The resonant wavelengths are extracted as function of the pitch for both nanoparticles. Coupling mechanism (1) dominates the coupling for S-polarized waves, while mechanism (2) dominates for P-polarized waves in angle dependent measurements.*

For P-polarized excitation, the coupling is dominated by longitudinal magnetic coupling and transverse electric coupling, while for the S-polarized excitation the coupling is dominated by longitudinal electric coupling and transverse magnetic coupling.

4.3.4 Refractive index sensing

The samples were mounted in a flowcell to perform bulk refractive index sensing measurements with different concentrations of glycerol in water. An overview of these measurements is presented in figure 4.10. In panel a, the linewidth reduction for the phase-sensitive measurements with respect to the intensity-based reflection measurements is clearly illustrated for nanorings in air. At the dip of the LSPR for both polarization states, a narrow phase change is observed in $cos(\Delta)$. Panel b shows the wavelength shift as function of increasing glycerol concentrations in water. Here we used an incident angle of 70^o, such that the incident angle at the sample/solution interface matches the 45^o incident angle of the reference measurement in air. As expected, with increasing refractive index, we observe a red-shift of the resonance positions for both polarization states.

Different plasmon modes are excited for P- and S-polarization, which show different sensitivities to the refractive index. Moreover, depending on the spectral position of both resonances and their spectral overlap, the shape of the $cos(\Delta)$ signals can change dramatically for the different nanoparticles. This effect is clearly observed

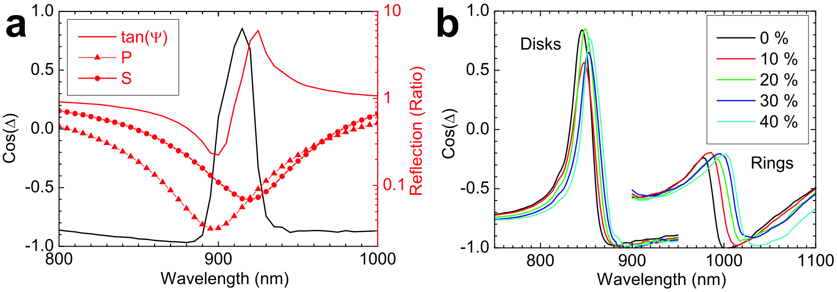

Figure 4.10: *Refractive index sensing measurements on gold nanodisks and nanorings for* 45^o *incidence. (a) Comparison of phase-sensitive measurements (black) and intensity based measurements (red) on gold nanorings in air, illustrating a dramatic line width reduction in the phase-difference between P and S. (b) Refractive index sensing measurements on disks and disks with variable concentrations of glycerol in water.*

when comparing the spectra for disks and rings in air and in solution. If the plasmon modes for P and S show a lot of spectral overlap, the maximum phase difference between the 2 modes will be reduced significantly. We clearly observe this reduction for the rings the sensing solution (panel b) and the disks in air (figure 4.7), where the overlap of the modes is the largest. This implies that for the gold rings the sensitivity of the P-mode is much larger than for the S-mode, as they are separated by about 30 nm in air, while in the sensing solutions they clearly show spectral overlap. In order to calculate the figure of merit of the 2 model systems, we calculated the sensitivities for the combined phase-sensitive $cos(\Delta)$ signals of the P- and S-modes and compared these with the amplitude based reflection data. In the overview presented in table 4.1, we can clearly see that the phase sensitive measurements show much narrower line widths compared to their intensity-based counterparts. Due to this dramatic decrease in the spectral footprint, the FOM could be boosted 3.9 and 6.1 times up to 8.3 and 16.5 for nanodisks and nanorings respectively. For the samples presented here, we didn't optimize the structures in order to reach the smallest possible line widths. This implies that there is still a lot of room for improvement in the sample design. The effects of inhomogeneous broadening can be largely suppressed by studying periodic arrays. Moreover, by looking at asymmetric particles the resonances for P and S can be spectrally detuned and in that way one could easily fit the linewiths of a single resonance instead of the combined line width as we did in this work. Here we mainly focused on proof-of-principle and therefore we restricted our measurements to bulk changes in the refractive index. For structures similar to the ones described here, we expect the decay length for the field enhancements to be several tens of nanometers [6], which implies that these samples could also be applied for biological sensing using antibody/antigen interactions, where the improved FOM could result in lower detection limits.

Table 4.1: *Comparison between intensity- and phase-sensitive reflection measurements on gold nanodisks and nanorings at an incidence angle of* 45^o.

	Disks	Rings
$d\lambda/dn$ (nm/RIU)	208	380
FWHM reflection (nm)	98	139
FOM reflection	2.1	2.7
FWHM $cos(\Delta)$ (nm)	25	23
FOM $cos(\Delta)$	8.3	16.5
FOM increase ratio	3.9	6.1

4.4 Conclusions

We have shown that the FOM for reflection based refractive index sensing can be largely increased by measuring the phase of the reflected beam instead of its intensity only. Around the center frequency of the LSPR, the electron cloud makes the transition of in- to out-of-phase oscillation with respect to the driving field, which is an intrinsic property of a plasmon resonance. This phase difference shows a much smaller spectral footprint than the intensity based reflection measurements, resulting in much narrower line widths and largely increased values of the FOM. For the nanoparticles investigated in this work, we managed to increase the FOM up to 6 times for intrinsically broad dipole resonances.

Bibliography

[1] K. Lodewijks, W. Van Roy, G. Borghs, L. Lagae, and P. Van Dorpe, "Boosting the Figure-Of-Merit of LSPR-Based Refractive Index Sensing by Phase-Sensitive Measurements," *Nano Letters*, vol. 12, pp. 1655–1659, 2012.

[2] F. Hao, P. Nordlander, Y. Sonnefraud, P. Van Dorpe, and S. a. Maier, "Tunability of subradiant dipolar and fano-type plasmon resonances in metallic ring/disk cavities: implications for nanoscale optical sensing.," *ACS nano*, vol. 3, no. 3, pp. 643–52, 2009.

[3] N. Verellen, P. Van Dorpe, C. Huang, K. Lodewijks, G. a. E. Vandenbosch, L. Lagae, and V. V. Moshchalkov, "Plasmon Line Shaping Using Nanocrosses for High Sensitivity Localized Surface Plasmon Resonance Sensing," *Nano Letters*, vol. 11, no. 2, p. 110125111509056, 2011.

[4] A. Kabashin and P. Nikitin, "Surface plasmon resonance interferometer for bio- and chemical-sensors," *Optics communications*, vol. 150, no. 1-6, pp. 5–8, 1998.

[5] A. V. Kabashin, S. Patskovsky, and A. N. Grigorenko, "Phase and amplitude sensitivities in surface plasmon resonance bio and chemical sensing.," *Optics express*, vol. 17, no. 23, pp. 21191–204, 2009.

[6] S. Chen, M. Svedendahl, M. Käll, L. Gunnarsson, and a. Dmitriev, "Ultrahigh sensitivity made simple: nanoplasmonic label-free biosensing with an extremely low limit-of-detection for bacterial and cancer diagnostics.," *Nanotechnology*, vol. 20, no. 43, p. 434015, 2009.

[7] J. Anker, W. Hall, O. Lyandres, N. Shah, J. Zhao, and R. Van Duyne, "Biosensing with plasmonic nanosensors," *Nature materials*, vol. 7, no. 6, pp. 442–453, 2008.

[8] J. Ye, M. Shioi, K. Lodewijks, L. Lagae, T. Kawamura, and P. Van Dorpe, "Tuning plasmonic interaction between gold nanorings and a gold film for surface enhanced Raman scattering," *Applied Physics Letters*, vol. 97, no. 16, p. 163106, 2010.

[9] K. Lodewijks, N. Verellen, W. Van Roy, V. Moshchalkov, G. Borghs, and P. Van Dorpe, “Self-assembled hexagonal double fishnets as negative index materials,” *Applied Physics Letters*, vol. 98, no. 9, p. 091101, 2011.

[10] P. Neutens, P. Van Dorpe, I. De Vlaminck, L. Lagae, and G. Borghs, “Electrical detection of confined gap plasmons in metalâĂŞinsulatorâĂŞmetal waveguides,” *Nature photonics*, vol. 3, no. 5, pp. 283–286, 2009.

[11] P. Neutens, L. Lagae, G. Borghs, and P. Van Dorpe, “Electrical excitation of confined surface plasmon polaritons in metallic slot waveguides.,” *Nano letters*, vol. 10, no. 4, pp. 1429–32, 2010.

[12] H. A. Atwater and A. Polman, “Plasmonics for improved photovoltaic devices.,” *Nature materials*, vol. 9, no. 3, pp. 205–13, 2010.

[13] N. I. Zheludev, S. L. Prosvirnin, N. Papasimakis, and V. a. Fedotov, “Lasing spaser,” *Nature Photonics*, vol. 2, no. 6, pp. 351–354, 2008.

[14] M. a. Noginov, G. Zhu, a. M. Belgrave, R. Bakker, V. M. Shalaev, E. E. Narimanov, S. Stout, E. Herz, T. Suteewong, and U. Wiesner, “Demonstration of a spaser-based nanolaser.,” *Nature*, vol. 460, no. 7259, pp. 1110–2, 2009.

[15] A. B. Evlyukhin, S. I. Bozhevolnyi, A. Pors, M. G. Nielsen, I. P. Radko, M. Willatzen, and O. Albrektsen, “Detuned Electrical Dipoles for Plasmonic Sensing.,” *Nano letters*, 2010.

[16] F. Hao, Y. Sonnefraud, P. Van Dorpe, S. a. Maier, N. J. Halas, and P. Nordlander, “Symmetry breaking in plasmonic nanocavities: subradiant LSPR sensing and a tunable Fano resonance.,” *Nano letters*, vol. 8, no. 11, pp. 3983–8, 2008.

[17] B. Luk’yanchuk, N. I. Zheludev, S. a. Maier, N. J. Halas, P. Nordlander, H. Giessen, and C. T. Chong, “The Fano resonance in plasmonic nanostructures and metamaterials.,” *Nature materials*, vol. 9, no. 9, pp. 707–15, 2010.

[18] P. Offermans, M. C. Schaafsma, and S. R. K. Rodriguez, “Universal Scaling of the Figure of Merit of Plasmonic Sensors,” *ACS nano*, vol. 5, no. 6, pp. 5151–7, 2011.

[19] V. G. Kravets, F. Schedin, A. V. Kabashin, and A. N. Grigorenko, “Sensitivity of collective plasmon modes of gold nanoresonators to local environment,” *Optics letters*, vol. 35, no. 7, pp. 956–958, 2010.

[20] H. Fredriksson, Y. Alaverdyan, a. Dmitriev, C. Langhammer, D. Sutherland, M. Zäch, and B. Kasemo, “HoleâĂŞMask Colloidal Lithography,” *Advanced Materials*, vol. 19, no. 23, pp. 4297–4302, 2007.

[21] “Gesp 5 ellipsometer, sopralab.”

[22] S. E. Jasperson, S. N.; Schnatterly, “An improved method for high reflectivity ellipsometry based on a new polarization modulation technique,” *Review of Scientific Instruments*, vol. 40, no. 6, pp. 761–767, 1969.

[23] “Comsol multiphysics 3.5a, rf module, http://www.comsol.com.”

[24] A. O. Pinchuk, “Angle dependent collective surface plasmon resonance in an array of silver nanoparticles.,” *The journal of physical chemistry. A*, vol. 113, pp. 4430–6, Apr. 2009.

[25] “Lumerical fdtd, http://www.lumerical.com/fdtd.”

Chapter 5

The interaction of localized and propagating surface plasmons in sensing applications

5.1 Introduction

In this chapter we investigate the interaction of localized (LSPR) and propagating (SPP) plasmon modes for sensing applications. We studied periodic arrays of gold nanodisks on top of a continuous gold layer and a silica spacer, similar to the structures discussed in chapter 4. The periodicity of the sample structure has two key advantages:

(1) The coupling between the LSPR modes in the neighboring particles is the same for all particles in the array, resulting in much narrower line widths for the LSPRs [1].

(2) The periodic particle array acts as a grating which allows for very efficient excitation of SPP modes on the gold layer below.

By properly designing the size and pitch of the gold nanoparticles, the LSPR mode and the SPP mode for the P-polarization can be tuned to be in the same spectral region, resulting in very strong coupling of both modes. We observe pronounced Fano-interference between these 2 modes which show anti-crossing behavior as we scan the angle of incidence. We measured the phase difference between P- and S-polarized waves by spectroscopic ellipsometry and characterized the phase differences in the spectral regions where the SPP and LSPR modes interact strongly. The resulting line widths of the LSPR and SPP modes are strongly reduced compared to random nanoparticle arrays and the resulting FOM values for phase-sensitive measurements reach values ranging from 16 to 58 for the respective plasmon modes.

The investigated sample structures are illustrated in figure 5.1. We studied two

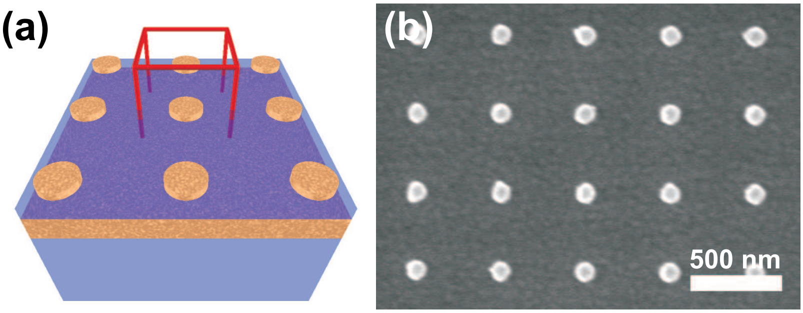

Figure 5.1: *(a) Schematic sample structure for a* $1\mu m^2$ *sample area of periodically arranged gold nanodisks. The red wire box indicates the unit cell used in simulations (b) Top view SEM picture in which the grains of the bottom gold layer are clearly visible.*

sample geometries consisting of a square array of gold nanodisks with a pitch of 400 nm and a disk diameter of 100 nm and 140 nm.

5.2 Sample fabrication

The periodic arrays of gold nanodisks were fabricated by EBL and the processing steps are outlined in figure 5.2. We start from a glass substrate which is cleaned using H_2SO_4/H_2O_2 3 : 1 for 15 minutes, followed by an oxygen plasma treatment (a). The $Au(100nm)$ and $SiO_2(50nm)$ layers are sputter deposited onto the substrate (b). A 200 nm PMMA e-beam resist layer is spin coated on top (c). The disk structures are written in PMMA resist by EBL with diameters of 100 and 140 nm. A periodic array of holes in PMMA is created by development of the resist (d). 30 nm of Au is evaporated forming disks in the holes (e). The PMMA layer is lifted off leaving the array of disk particles on the substrate (f).

After the sample fabrication, the samples were annealed at 400^oC in nitrogen environment in order to obtain recrystallization of the grains. During this process, the grain sizes increase while the number of scattering sites at the boundaries is largely decreased, resulting in major reduction in the damping of the plasmon modes [2]. All plasmon resonances present in our samples show a minor blue shift (about 10 nm), and more pronounced and narrower dips in the reflection spectra after the annealing step. A similar observation is made for the spectroscopic ellipsometry spectra, in which the dips and peaks (in $\tan\Psi$) become more pronounced and narrow, and the measured phase difference (in $\cos\Delta$) at the plasmon resonances is increased and shows a reduction in line width.

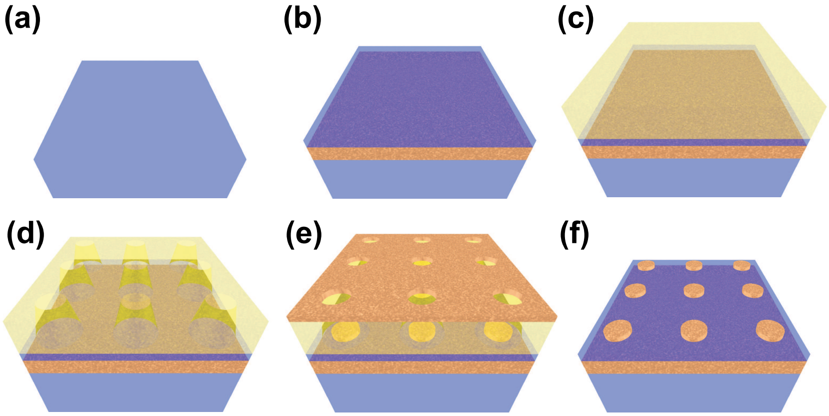

Figure 5.2: *Sample fabrication steps for periodic disk arrays.*

5.3 Results and discussion

5.3.1 Basic optical characterization

Our periodic arrays of gold nanodisks show 3 pronounced plasmon modes that can be used for sensing applications. As in the case of the random disks described in the previous chapter we observe a LSPR in the gold disks for P- (P-LSPR) and S-polarization (S-LSPR). On top of that a propagating SPP mode on top of the bottom gold layer is excited for the P-polarization due to very efficient grating coupling by the disk array. The interaction between these 3 modes can be tuned by changing the disk size and the angle of incidence. Figure 5.3 shows reflection spectra for 100 nm (panel a) and 140 nm (panel b) disk sizes at an incident angle of 45^o. Note that for the S-polarization the SPP grating mode falls outside of the spectral region of interest, so it does not interact with the S-LSPR.

For the 100 nm disks in panel (a) the P-LSPR is observed at 640 nm, while the propagating SPP mode is observed at 760 nm. Both of them are spectrally separated and show a symmetric line shape, indicating that they do not interact strongly. For the S-polarization we only observe a LSPR mode at 670 nm. For the 140 nm disks in panel (b) on the other hand we can clearly observe 2 modes with asymmetric line-shapes for the P-polarization, indicating strong Fano interference [3] between the localized and the propagating mode. In this case we observe the SPP mode at 705 nm and the P-LSPR mode at 795 nm, meaning their spectral positions are switched. For the S-polarization we observe the LSPR mode at 760 nm. In the next sections we will discuss these interactions in more detail by investigating the angle dependent reflection spectra and simulations.

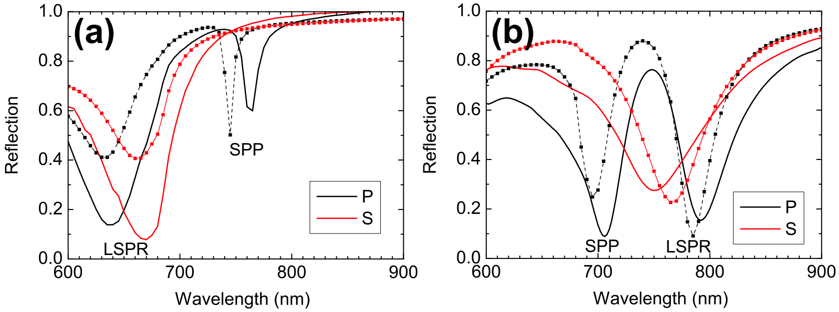

Figure 5.3: *Measured (full lines) and simulated (dotted lines) reflection spectra for P- and S-polarized waves under 45^o incidence. (a) For 100 nm disks the P-LSPR is excited at shorter wavelengths than the SPP mode. (b) For 140 nm disks the SPP mode is excited at shorter wavelengths than the P-LSPR mode. Due to the coupling of the SPP and P-LSPR mode, the line shapes are highly asymmetric.*

SPP grating mode

In this section we want to look in more detail to the behavior of the SPP grating modes in periodic nanodisk samples. We first focus our attention to 100 nm disks, where the SPP mode occurs at longer wavelengths than the LSPR mode, as illustrated in figure 5.3 (a). We performed angle and polarization dependent measurements and simulations [4], of which the overview is presented in figure 5.4.

For the P-polarization we clearly observe two pronounced reflection bands in the measurements (panel a) and simulations (panel b) which exhibit nice qualitative agreement. The lower broad reflection band corresponds to the P-LSPR, which shows a minor red shift with increasing angle of incidence. The upper narrow reflection band corresponds to the propagating SPP mode which is excited on the top of the continuous gold layer and shows a pronounced red shift with increasing angle of incidence. For the S-polarization we only observe one broad reflection band for the LSPR which also shows a very minor red shift with increasing angle of incidence.

The grating SPP mode shows a red shift with increasing angle of incidence, which has been reported before for plasmonic grating structures [5]. The structure reported here differs from a conventional plasmon grating, as we have a periodic array of gold disks on top of a continuous gold layer and a dielectric spacer. The grating of nanoparticles allows for very efficient excitation of propagating SPP plasmon modes on the continuous gold layer. For perpendicular incidence only one grating peak is observed, which corresponds to the excitation of propagating plasmons that travel both to the left and to the right. If the angle of incidence is increased the grating mode splits up in two diffracted peaks, as illustrated in the schematic overview in figure 5.5. These modes are the $\nu = +1$ diffracted grating mode (right) and $\nu = -1$ diffracted grating mode (left) which can be described by the grating formula

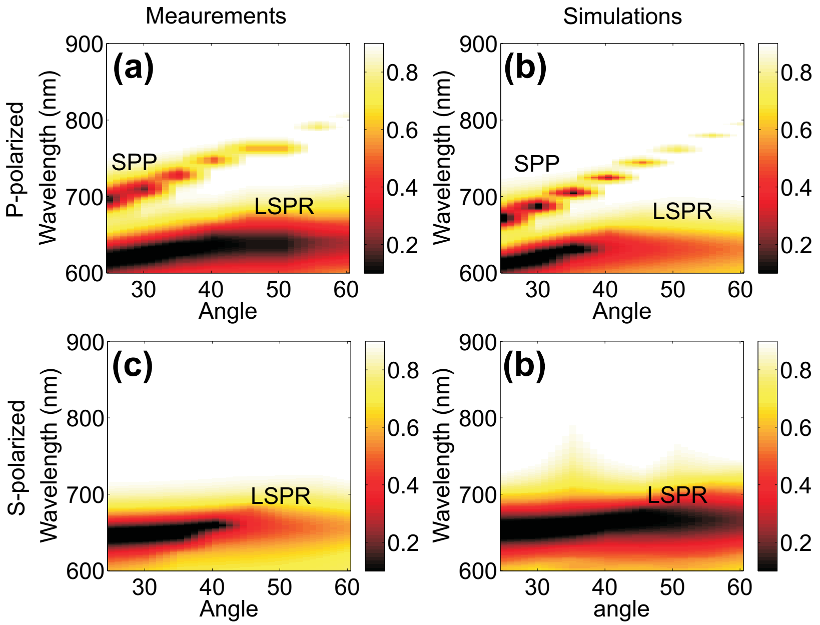

Figure 5.4: *Intensity plots for angle dependent reflection measurements and simulations on 100 nm disks in air. (a) Measured spectra for P-polarization. (b) Simulated spectra for P-polarization. (c) Measured spectra for S-polarization. (d) Simulated spectra for S-polarization.*

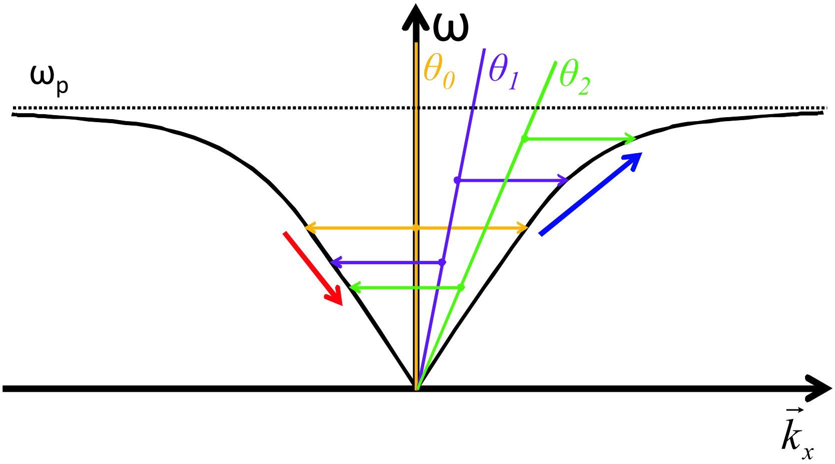

Figure 5.5: *Schematic overview of the plasmon dispersion curve and grating coupling of plasmons to the +1 (right) and -1 (left) order. For increasing values of the angle of incidence θ the light lines depict the x-component of the wave-vector, while the colored arrows indicate the grating wave vector, which has the same magnitude for all incident angles.*

$$k_{SPP} = k \sin\theta \pm \nu \frac{2\pi}{a} \tag{5.1}$$

in which a depicts the pitch of the grating.

With increasing angle of incidence we observe a blue shift for the +1 and a red shift for the −1 diffracted grating order. The grating mode we observe in our measurements corresponds to the latter mode. These shifts can be understood by looking at the waveguided modes which are excited at the respective resonances. For the lower energy (−1 diffraction) mode the Poynting vector of the excited SPP wave is anti-parallel with the in-plane wave vector of the incident wave, while for the higher energy (+1 diffraction) mode the Poynting vector of the excited SPP mode is parallel with the in-plane wave vector of the incident wave. Therefore, with increasing angle of incidence, the incident wave will provide additional momentum to the higher energy grating mode, resulting in a blue shift. For the lower energy mode however, with increasing angle the additional momentum from the incident wave will reduce the total energy of the mode which travels anti-parallel to the incident wave, resulting in a red shift. This explains the red shift with increasing angle of incidence for the SPP mode in figure 5.4. We don't observe the higher energy mode for a pitch of 400 nm in the measurements and simulations, due to the fact that at wavelengths below

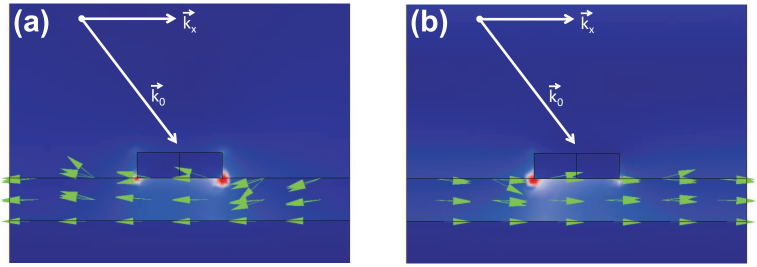

Figure 5.6: *Color plots of the time averaged energy flow for 100 nm disks. The incident wave is propagating to the right. (a) At the SPP mode at 690 nm the Poynting vector (green arrows) is anti-parallel to the in-plane wave vector of the incident wave. (b) Away from the plasmon resonances at 800 nm the Poynting vector (green arrows) is parallel to the in-plane wave vector of the incident wave.*

600 nm the reflection spectra are dominated by inter-band transitions of the gold.

In figure 5.6 an overview is presented of the simulated power flow at the SPP mode for an angle of incidence of 30^o. In case of 100 nm nanodisks with a pitch of 400 nm, the power flow at the grating SPP mode is anti-parallel with the in-plane component of the incident wave vector for all angles of incidence. In simulations with increased pitch, we clearly observe that the SPP grating mode splits up in two propagating modes for non-perpendicular incidence. With increasing angles of incidence, these 2 components show opposite shifts as expected. The Poynting vector plots at both grating modes clearly indicate that the excited SPPs of the blue (red) shifting mode travel parallel (anti-parallel) to the in-plane component of the incident wave.

Fano interference between localized and propagating plasmon modes

Now that we understand the behavior of the non-interacting propagating SPP mode, we want to investigate how it couples with the localized resonance in the nanoparticles. To that extent, we fabricated gold disks with a 140 nm diameter, of which the localized resonance is shifted to longer wavelengths. An overview of the angle and polarization dependent reflection measurements and simulations is provided in figure 5.7, which show good qualitative matching. We can clearly observe that the spectral positions of the P-LSPR and SPP mode have switched compared to the 100 nm disk case.

As in the previous section, we observe again 2 reflection bands for the P-polarization and one reflection band for the S-LSPR. In P-polarization the lower narrow band now corresponds to the SPP mode, while the upper broad band corresponds to the LSPR mode. It is clear that also in this case the SPP mode shows a red shift with increasing angle of incidence, but we see that it starts to interfere strongly with the localized

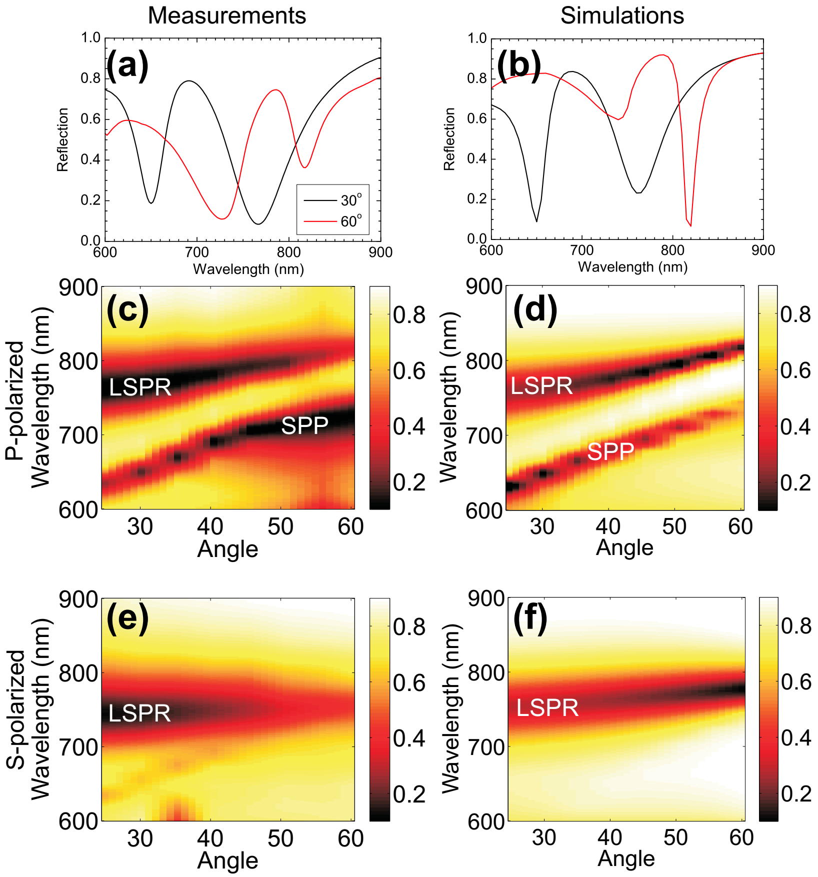

Figure 5.7: *Reflection spectra and intensity plots for angle dependent measurements and simulations on periodic arrays of 140 nm disks in air. (a) Measured spectra for P-polarization in case of weak coupling (30^o) and strong coupling (60^o). (b) Simulated spectra for P-polarization in case of weak coupling (30^o) and strong coupling (60^o). (c) Measured mode plot for P-polarization. (d) Simulated mode plot for P-polarization. (e) Measured mode plot for S-polarization. (f) Simulated mode plot for S-polarization.*

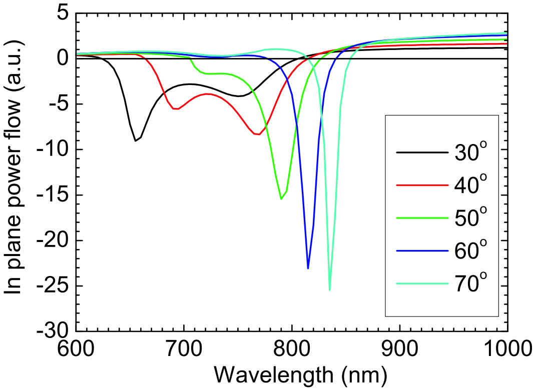

Figure 5.8: *Extracted in plane power flow for 140 nm disks. Positive (negative) values represent energy flow (anti-) parallel with the in-plane component of the incident wave vector.*

modes when the angle of incidence exceeds 45^o. As a result, the red shift of the SPP grating mode is decreased and it shows pronounced broadening. The LSPR on the other hand shows a severe decrease in line width and increased red shift due to anti-crossing [6, 7] behavior of the two plasmon modes. If we look at the extracted power flow for different angles of incidence in figure 5.8, we can clearly see that the power flow is anti-parallel with the in-plane wave vector of the incident wave at the P-LSPR and the SPP mode (and even for the intermediate wavelengths for small angles of incidence). For angles above 50^o we see that the power flow at the SPP mode decreases and even reverses its direction due to the pronounced interaction with the P-LSPR. At that point, the mode even starts to blue shift when we increase the angle of incidence further.

If we compare the mode plots of figure 5.7 with those for randomly distributed gold nanodisks from the previous chapter in figure 5.9, we can see that the strong interaction between the P-LSPR and the SPP mode influences the spectral position of the P-LSPR significantly, while for the S-LSPR we don't observe any changes as it is not interacting with any other plasmon modes.

As a next step, we repeated the angle dependent reflection measurements on the same sample in water, of which the mode plots are given in figure 5.10. As the different plasmon modes for P- and S-polarization have different sensitivities to the refractive index, we observe some pronounced changes in their interaction.

Upon exposure to water, the P-LSPR and SPP mode switch their spectral positions and the P-LSPR occurs at shorter wavelengths than the SPP mode. Now we observe similar anti-crossing behavior for the P-LSPR and SPP resonances for small angles of incidence, where it is clear that the P-LSPR is pushed to even higher energies than for the measurements in air due to the pronounced coupling between the LSPR and

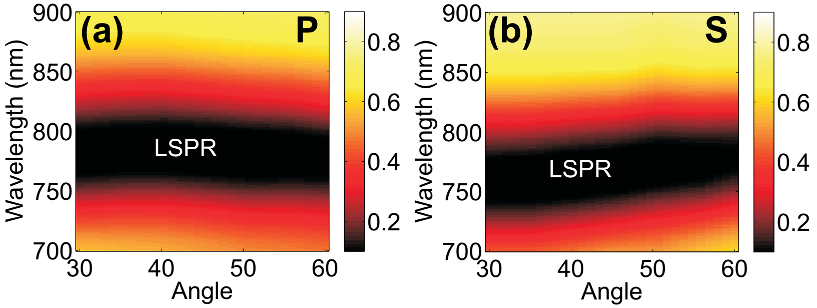

Figure 5.9: *Intensity plots for angle dependent reflection measurements on randomly distributed 140 nm disks in air. (a) Measured spectra for P-polarization. (b) Measured spectra for S-polarization.*

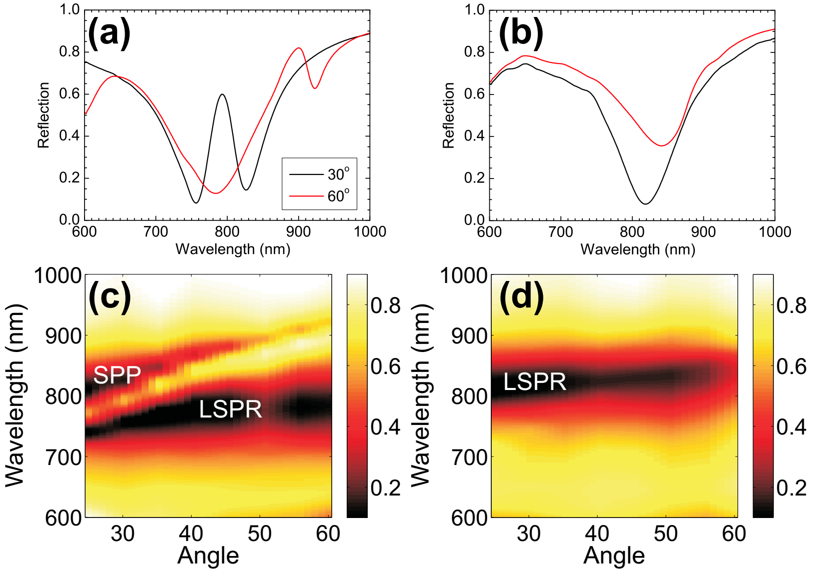

Figure 5.10: *Reflection spectra and intensity plots for angle dependent measurements on periodic arrays of 140 nm disks in water. (a) Measured spectra for P-polarization in case of strong coupling (30^o) and weak coupling (60^o). (b) Measured spectra for S-polarization. (c) Measured mode plot for P-polarization. (d) Measured mode plot for S-polarization.*

the SPP resonance. The spectral response due to the interaction of both modes is similar to the one observed for large angles of incidence in air: the SPP mode shows pronounced broadening while the P-LSPR mode shows a severe reduction in line width for the smallest angles of incidence. With increasing angles of incidence, the SPP mode shows the expected red shift, opening up spectral space for the LSPR mode to show the same trend. As a result of the spectral separation of both modes with increasing angles of incidence, the line width of the P-LSPR is broadened while it narrows for the SPP mode. Note that even for large angles of incidence, the resonance position of the P-LSPR does not shift beyond its resonance position in air, implying it is still interacting with the SPP mode which prevents the P-LSPR to shift to its natural resonance position.

5.3.2 Phase-sensitive spectroscopic ellipsometry

In the previous chapter, we already showed that we can pick up the phase difference between the reflected signals for P- and S-polarized waves in spectroscopic ellipsometry measurements, and that pronounced phase differences are observed at the center frequency of the LSPR [8, 9]. Similar measurements were already reported for propagating SPP modes in SPR based sensing [10, 11]. Here we show that we can measure both of them in the same sample structures in which the P-LSPR and SPP modes are strongly interacting. As such, we can investigate the phase differences at the Fano resonance between the localized and propagating modes.

Figure 5.11 shows the spectroscopic ellipsometry measurements and simulations for 100 nm disks in air. In the $\tan\Psi$ (panel a and c) value we observe for increasing wavelengths a first dip for the P-LSPR, a peak for the S-LSPR and a second dip for the SPP mode which shows a pronounced shift with the incident angle. As there is no pronounced interaction between the different plasmon modes, and they are all spectrally separated, we observe 3 pronounced phase differences in the $\cos\Delta$ value (panel b and d), one for every plasmon resonance. The two LSPRs show the most pronounced phase difference, while the SPP grating mode only shows a very small phase difference. Similar to the observations for random particle arrays (chapter 4) we see that the largest phase differences are observed around the minima and maxima of the $\tan\Psi$ value, which are most pronounced for the LSPRs.

Figure 5.12 shows the spectroscopic ellipsometry measurements for 140 nm disks in air. As outlined in the previous section, the spectral position of the LSPR and the SPP mode in the P-polarization are switched with respect to the 100 nm disks. The increased interaction between these 2 modes results in asymmetric line shapes and larger phase differences at the center frequency of the different plasmon modes.

In the $\tan\Psi$ value (panel c) we observe for increasing wavelengths a first dip for the grating SPP mode, a peak for the S-LSPR and a second dip for the P-LSPR. The SPP mode shows a much more pronounced resonance dip (for small angles of incidence) compared to the 100 nm disks, and the resulting phase change (panel d) is also more pronounced. The second phase change can be attributed to the S-LSPR

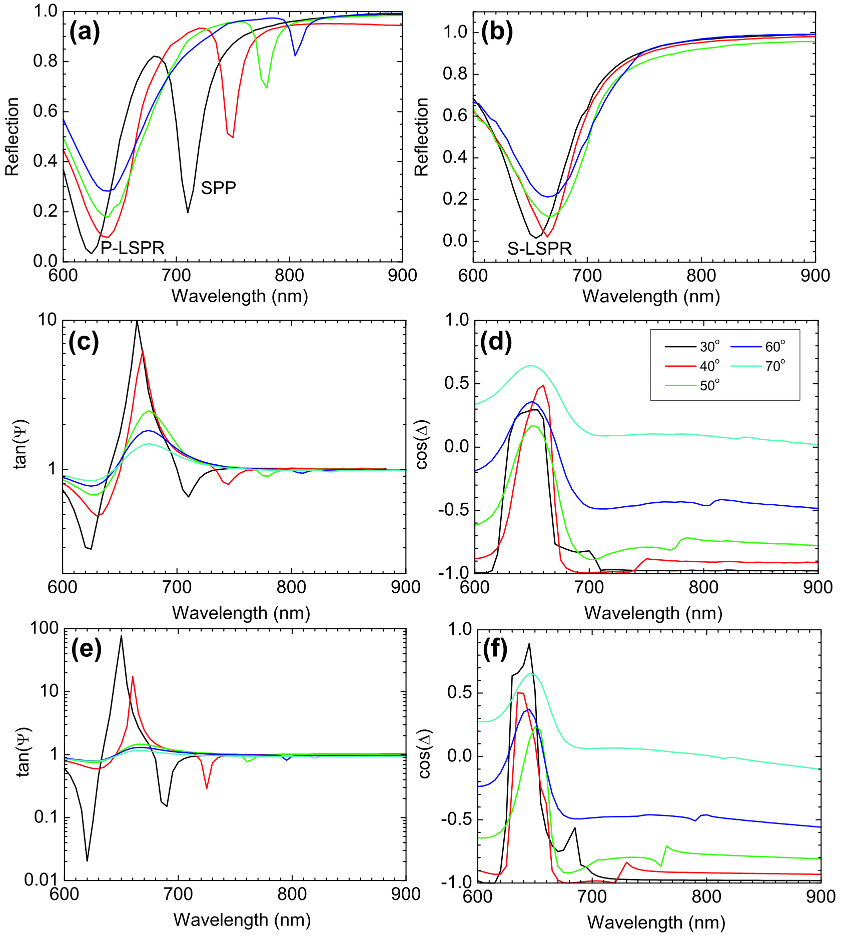

Figure 5.11: *Ellipsometry measurements and simulations for periodic arrays of 100 nm gold nanodisks. (a) Measured reflection spectra in P-polarization. (b) Measured reflection spectra in S-polarizations. (c) Measured reflection ratio* $\tan\Psi$*. (d) Measured phase difference between P- and S-polarization* $\cos\Delta$*. (e) Simulated values of* $\tan\Psi$*. (f) Simulated values of* $\cos\Delta$*.*

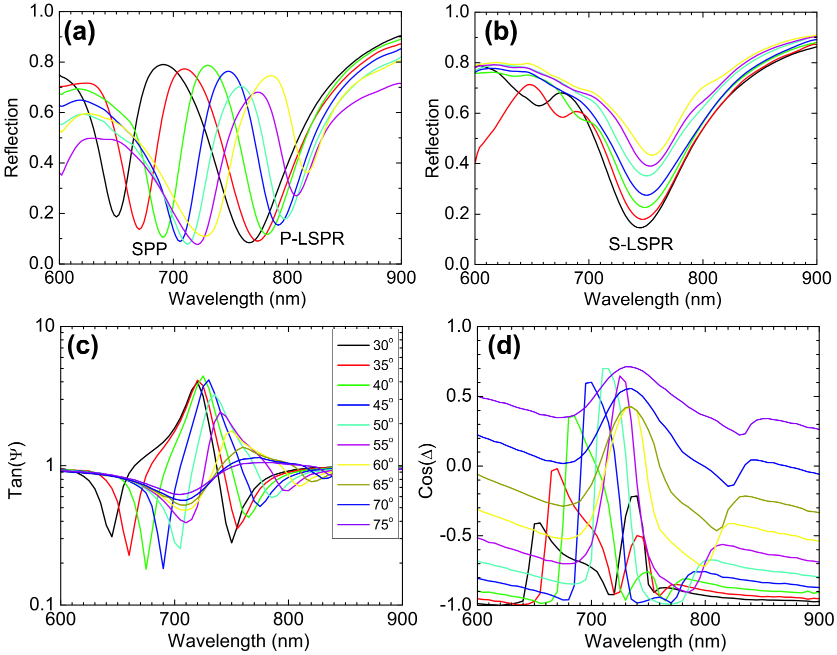

Figure 5.12: *Ellipsometry measurements on periodic arrays of 140 nm gold nanodisks. (a) Measured reflection spectra in P-polarization. (b) Measured reflection spectra in S-polarization. (c) Reflection ratio* $\tan\Psi$*. (d) Phase difference between P- and S-polarization* $\cos\Delta$.

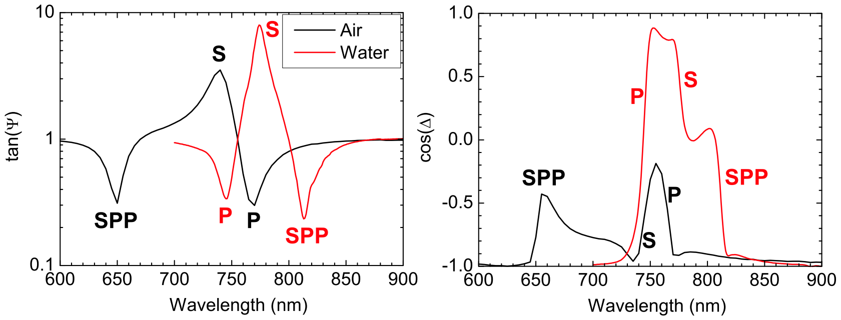

Figure 5.13: *Comparison of the spectroscopic ellipsometry measurements in air and water for 140 nm disks at an angle incidence of* 30^o*. P and S indicate the LSPR mode for the respective polarization state, while SPP refers to the propagating mode in P-polarization. (a) Measured* $\tan\Psi$ *values. (b) Measured* $\cos\Delta$ *values.*

while the smaller phase change at longer wavelengths is due to the P-LSPR. For large angles of incidence ($\theta > 50^o$), the grating SPP mode does not shift to longer wavelengths any more and even shows a minor blue shift for angles beyond 70^o, due to the coupling with the P-LSPR mode.

If we compare the reflection plots for the 140 nm disks in air (figure 5.7) and water (figure 5.10), we observe the switching of the spectral positions of the SPP mode and the P-LSPR mode and an increased spectral overlap of these 2 modes in water. The strong interaction between these modes results in completely different ellipsometry spectra in the two media, as illustrated in figure 5.13. Although the spectral overlap of the different plasmon modes is increased, we observe a larger phase difference in the $\cos\Delta$ value (panel b) for all resonances, which can be attributed to strong Fano-interference between the P-LSPR and SPP mode. The line widths of the phase sensitive signals show pronounced narrowing compared to the random particle distributions in the previous chapter, due to a decrease of the effects of inhomogeneous broadening.

5.3.3 Refractive index sensing

The extremely narrow line widths observed in phase sensitive spectroscopic ellipsometry measurements allow us to perform refractive index sensing measurements with largely increased values of the FOM and potentially much lower detection limits. We performed bulk refractive index sensing measurements (figure 5.13 a and b) in a flow cell by pumping solutions of glycerol in water with variable concentrations over our 140 nm disk sample and quantified the sensitivities and the FOM for the different plasmonic modes. In a second step we functionalized the sample with a carboxylated self-assembled monolayer (SAM) (C11-chain with COOH functional group, length 2

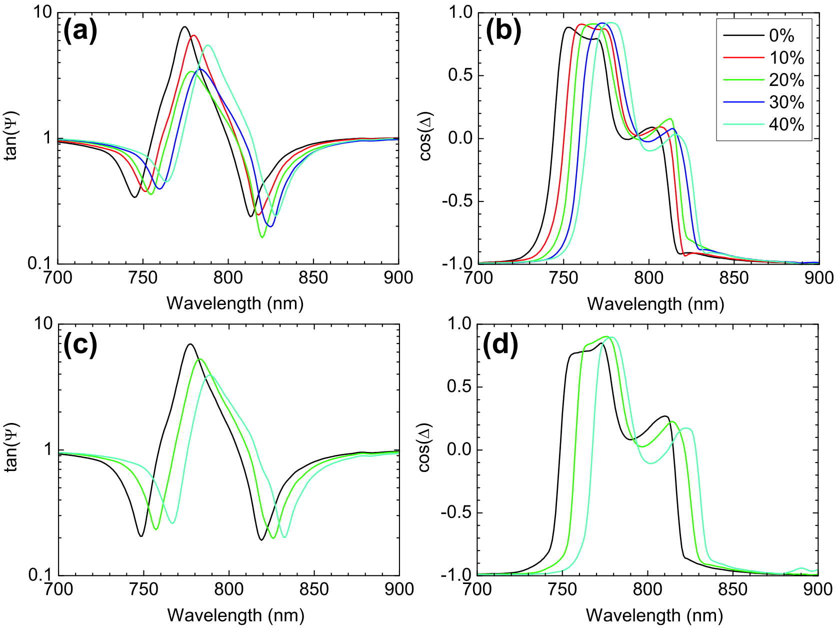

Figure 5.14: *Refractive index sensing measurements for different concentrations of glycerol in water with an incident angle of* 30^o*. (a) and (b) Measured ellipsometry parameters for cleaned gold nanodisk samples. (c) and (d) Measured ellipsometry parameters for gold nanodisks functionalized with a self-assembled monolayer.*

nm) and repeated the glycerol tests (panel c and d). In that way we can quantify the difference between local sensing (in close proximity of the nanostructures) and bulk sensing.

As expected, we observe a red shift for all the plasmon resonances with increasing values of the refractive index. The spectra for the sample with and without SAM are very similar, although all resonances show an additional red shift after functionalization. For the LSPRs we observe a red shift of 4 and 5 nm for the S- and P-polarization respectively and 6 nm for the SPP mode. An overview of the fitted resonance positions of the different modes is given in figure 5.15, together with linear fits to determine the sensitivity.

Clearly we observe a decrease in the sensitivity for the S-LSPR after functionalization with a SAM and similar sensitivities for the P-LSPR and SPP grating mode. The decrease in sensitivity for the S-LSPR can be attributed to the fact that the bulk is shielded from the surface of the nanoparticles where the highest electric field enhancements are observed. As the typical decay lengths for the LSPRs are in the order of a few tens of nanometers [12], we would expect a similar result for the P-

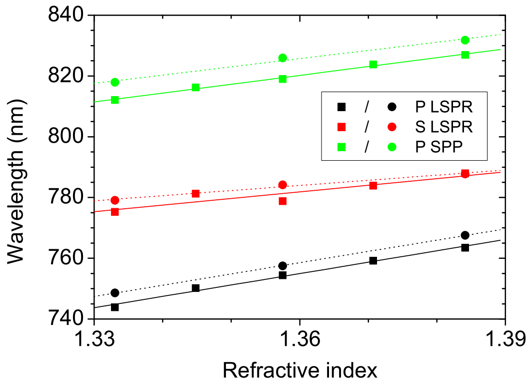

Figure 5.15: *Extracted resonance positions and fitting curves for the sensitivity in glycerol sensing measurements. The square symbols and full lines are the data for the cleaned nanodisk samples while the round symbols and dashed lines are the data for the sample functionalized with a SAM.*

Table 5.1: *Comparison of the sensitivities and FOMs for sensing measurement with and without SAM functionalization at an incidence angle of* 30^o.

	Without SAM			With SAM		
Mode	P-LSPR	S-LSPR	SPP	P-LSPR	S-LSPR	SPP
$d\lambda/dn$ (nm/RIU)	375	218	291	371	169	271
FWHM (nm)	7	9	5	7	10	5
FOM	54	24	58	53	17	54

LSPR. If we compare the fits for the LSPR in S- and P-polarization, this is clearly not the case.

From the overview in table 5.1, we see that also for the SPP mode and the P-LSPR mode the sensitivity is slightly reduced. Surprisingly, the sensitivity for the P-LSPR mode turns out to be higher than the one for the SPP mode and even twice as large as the sensitivity for the S-LSPR. If we compare the sensitivity with the values obtained for random nanoparticle distribution in the previous chapter, this turns out to be a very unusual result. We would expect the sensitivity of the two LSPR modes to be similar to the ones for the random particles, but we only observe this for the S-LSPR. Moreover we would expect that the sensitivity of the SPP mode would be the largest, as the decay length for a propagating mode is much longer than for a localized mode. In fact, the sensitivity for the SPP mode would be much larger than the one for the P-LSPR if the two modes wouldn't show any pronounced coupling. If we compare the spectra in air and water, we notice that the SPP-mode shifted beyond the P-LSPR mode in water, which already indicates that the SPP mode shows a higher sensitivity to the refractive index. On top of that, for the measurements in water (figure 2.10) we observe anti-crossing behavior between the P-LSPR and SPP mode, which causes the P-LSPR to be blue shifted with respect to its spectral position in air. When the refractive index of the surroundings is increased, the SPP mode shifts to longer wavelengths and thus away from the P-LSPR mode, allowing this one to also shift closer to its natural resonance position. Therefore we observe a much larger sensitivity for the P-LSPR in the periodic array than for random nanoparticle distributions. This type of Fano-interference could therefore also be exploited to boost the refractive index sensitivity of LSPR modes.

5.4 Conclusions

We have shown that the interaction between localized and propagating plasmon resonances in periodic arrays of gold nanoparticles on top of a silica spacer and a continuous gold layer can be used to tune the sensing performance. By adjusting the size of the nanoparticles and the pitch it is possible to tailor the optical response in such a way that the localized and propagating modes can be excited in a small spectral window. The Fano-interference between these 2 modes results in more pronounced phase differences with reduced line widths, making them very interesting for refractive index sensing applications. The sensitivity of the LSPR can be enhanced when it interacts with the SPP mode and can reach values which are twice as large as those for the non-interacting mode. The resulting line widths are in the range between 5 and 10 nm and the FOM values reach values in between 17 and 58 for the different plasmon modes.

Bibliography

[1] A. I. Kuznetsov, A. B. Evlyukhin, M. R. Gonçalves, C. Reinhardt, A. Koroleva, M. L. Arnedillo, R. Kiyan, O. Marti, and B. N. Chichkov, "Laser fabrication of large-scale nanoparticle arrays for sensing applications.," *ACS nano*, vol. 5, no. 6, pp. 4843–9, 2011.

[2] K.-P. Chen, V. P. Drachev, J. D. Borneman, A. V. Kildishev, and V. M. Shalaev, "Drude relaxation rate in grained gold nanoantennas.," *Nano letters*, vol. 10, no. 3, pp. 916–22, 2010.

[3] B. Luk'yanchuk, N. I. Zheludev, S. A. Maier, N. J. Halas, P. Nordlander, H. Giessen, and C. T. Chong, "The Fano resonance in plasmonic nanostructures and metamaterials.," *Nature materials*, vol. 9, no. 9, pp. 707–15, 2010.

[4] "Comsol multiphysics 3.5a, rf module, http://www.comsol.com."

[5] C. Maxime, "Surface plasmon polaritons in sub-wavelength metallic gratings studied by higher-order angle-resolved spectroscopy," *The European Physical Journal Applied Physics*, vol. 48, no. 1, p. 10901, 2009.

[6] W. Barnes, T. Preist, S. Kitson, and J. Sambles, "Physical origin of photonic energy gaps in the propagation of surface plasmons on gratings.," *Physical review. B, Condensed matter*, vol. 54, no. 9, pp. 6227–6244, 1996.

[7] Z. Chen, I. R. Hooper, and J. R. Sambles, "Coupled surface plasmons on thin silver gratings," *Journal of Optics A: Pure and Applied Optics*, vol. 10, no. 1, p. 015007, 2008.

[8] V. G. Kravets, F. Schedin, A. V. Kabashin, and A. N. Grigorenko, "Sensitivity of collective plasmon modes of gold nanoresonators to local environment," *Optics letters*, vol. 35, no. 7, pp. 956–958, 2010.

[9] K. Lodewijks, W. Van Roy, G. Borghs, L. Lagae, and P. Van Dorpe, "Boosting the Figure-Of-Merit of LSPR-Based Refractive Index Sensing by Phase-Sensitive Measurements," *Nano Letters*, vol. 12, pp. 1655–1659, 2012.

[10] A. Kabashin and P. Nikitin, “Surface plasmon resonance interferometer for bio- and chemical-sensors,” *Optics communications*, vol. 150, no. 1-6, pp. 5–8, 1998.

[11] A. V. Kabashin, S. Patskovsky, and A. N. Grigorenko, “Phase and amplitude sensitivities in surface plasmon resonance bio and chemical sensing.,” *Optics express*, vol. 17, no. 23, pp. 21191–204, 2009.

[12] S. Chen, M. Svedendahl, M. Käll, L. Gunnarsson, and a. Dmitriev, “Ultrahigh sensitivity made simple: nanoplasmonic label-free biosensing with an extremely low limit-of-detection for bacterial and cancer diagnostics.,” *Nanotechnology*, vol. 20, no. 43, p. 434015, 2009.

Chapter 6

Conclusions and Outlook

Although the field of metamaterials dates back only to the year 2000, it has grown tremendously over the past decade. Metamaterials are man-made artificial materials of which the optical properties can be engineered to generate the desired response to an incident electromagnetic wave. They consist of sub-wavelength sized structures which can be thought of as the atoms in conventional materials. The collective response of a randomly or periodically ordered ensemble of such meta-atoms defines the properties of the metamaterial, which can be described in terms of effective material parameters such as the permittivity, permeability, refractive index and impedance. These effective material parameters can be tailored at will to obtain the desired optical response, resulting in an improved control over the propagation of electromagnetic waves. This paves the way for many exciting applications such as negative refractive index materials, invisibility cloaking, advanced electromagnetic coatings for active semiconductor devices, integrated optical chips and interconnects, polarization rotation devices, slow light applications, novel biological and chemical sensors and many more.

In this thesis we focused on optical metamaterials in the visible and near-infrared wavelength range for sensing applications. The meta-atoms of the investigated samples are plasmonic resonators which we manufactured in bio-compatible materials such as gold and silica. The structures were fabricated by means of self-assembly processes such as nanosphere lithography (bottom-up) and conventional electron beam lithography (top-down).

In chapter 3 we proved the feasibility to fabricate a self-assembled version of the widely studied double fishnet metamaterial which exhibits a negative refractive index in the near-infrared wavelength range. A self-assembled monolayer of polystyrene beads was used to define a hexagonal pattern of round holes in the gold-silica-gold MIM layer stack. The obtained sample structures covered areas up to several several hundreds of square microns with single lattice orientation and up to square millimeter scales with multiple lattice orientations. The number of defects was small, resulting in similar performance as the electron beam lithography based reference samples.

In chapter 4 we showed that a self-assembled metamaterial of randomly distributed plasmonic gold nanoparticles on top of a continuous gold layer and a thin silica spacer serves as an excellent substrate for refractive index sensing. We performed angle dependent spectroscopic ellipsometry measurements in which the polarization state of the incident wave was modulated between P- and S-polarization, such that we could measure the phase difference between both reflected waves by lock-in measurements. The electric dipole resonances in the gold nanoparticles become spectrally detuned as we scan the angle of incidence, which allows us to detect the phase difference at the center frequency of both localized surface plasmon resonances. At the center frequency, the electron cloud makes the transition from in- to out-of-phase oscillation with respect to the incident wave, which happens in a very narrow spectral region. As this phase change is an intrinsic property of any given plasmon resonance, phase-sensitive measurements provide a powerful tool to study the fundamental properties of plasmon resonances. The resulting line widths could be reduced with a factor 4 to 6, resulting a major boost of the Figure-Of-Merit for refractive index sensing which could allow to reduce the detection limit significantly. For the two model systems of gold nanodisks and nanorings the obtained values for the FOM reached values as high as 8 and 16, for intrinsically broad dipole plasmon resonances.

In Chapter 5 we extended the concepts developed in chapter 4 to periodically ordered arrays of plasmonic resonators in the same sample configuration. Due to the periodicity of the samples, the effects of inhomogeneous broadening of the LSPRs are severely reduced, resulting in much more narrow line widths and improved FOMs for refractive index sensing. On top of that, the periodic array of gold nanodisks acts as a very efficient grating for the excitation of propagating SPPs on the gold layer below. These propagating SPP modes interact strongly with the LSPRs in the nanoparticles, giving rise to strong Fano-interference which results in very asymmetric line shapes for the interacting plasmon modes. By properly tuning the particle size and the pitch of the nanodisk arrays, the interaction between these modes can be tuned, and we observe anti-crossing behavior of the propagating and localized modes as we scan the angle of incidence. We observe larger phase differences at the center frequencies of the interacting plasmon modes with largely reduced line widths, which are applied for refractive index sensing. We clearly showed that in case of strong interaction between the SPP and LSPR mode, the sensitivity of the localized mode can be enhanced to almost twice the value of the non-interacting mode, providing an extra degree of freedom to optimize plasmonic structures for refractive index sensing. The FOM for the non-interacting LSPRs was improved up to 3 times the value of randomly distributed nanoparticles, reaching values up to 24. For the interacting SPP and LSPR modes the sensitivity was greatly enhanced while the line could be reduced severely, resulting in FOM values up to 54 and 56 for the respective modes.

To summarize, we have shown that high quality plasmonic metamaterials can be fabricated by self-assembly based bottom-up fabrications methods. The self-assembled samples perform very similar to reference structures based on conventional e-beam lithography. We have shown that spectroscopic ellipsometry is a very powerful tool to measure the phase differences at the center frequency of localized and propagating plasmon resonances. As we are measuring the transition from in- to out-of-phase oscillation of the electron cloud - an intrinsic property of any plasmon mode that occurs in a very narrow spectral region - the resulting line widths are severely reduced, giving rise to a major boost of the FOM for refractive index sensing. Furthermore we proved that we can push the FOM to higher values by properly designing periodic arrays of plasmonic nanostructures in which propagating SPP and localized LSPR modes show pronounced Fano interference. The strong interaction between these modes allows to enhance the refractive index sensitivity of localized plasmon modes significantly.

In the field of metamaterials many challenges are still ahead of us. While the field started out in the quest for its “holy grail”, negative refractive index materials (NIMs) and perfect lenses, nowadays it extends far beyond that. Although NIMs are very interesting from the fundamental point of view, their real-life application in microscopy or lithography is not straightforward, as the increased resolution is limited to the near field of the NIM.

We have provided proof-of-principle for several novel concepts in plasmonic metamaterials for refractive index based sensing. These concepts can serve as a toolbox for the future design of bio-chemical sensors with superior performance to the currently available platforms. In this work we mainly focused on the optimization of the sample performance which can be quantified by the FOM. In practical applications this is of course not the only parameter to be considered, as the detection limit also depends strongly on the signal-to-noise ratio and the quality of the interfacing with the analyte molecules. Therefore in a next step, the applicability of the developed concepts should be further assessed by chemical and biological functionalization of the substrates in order to quantify the sensitivity and the attainable detection limits in a real-life application. On the sample design side there is still room for improvement as there are many different parameters to tailor the plasmonic response and to fine tune the interaction between the different plasmon modes. Due to their small dimensions, plasmonic metamaterial sensors offer great potential for fully integrated lab-on-chip sensing platforms, as both light sources and semiconductor detectors can be integrated on-chip and interface with the plasmonic structures, while the data processing can be integrated through regular CMOS designs.

We expect that spectroscopic ellipsometry will have a significant influence on research in metamaterials and plasmonics in the coming years, as it is a commercially available non-destructive measurement method which can probe the phase information of localized and propagating plasmon modes, providing deeper insight in their nature. Another closely related technique has attracted more and more attention from the plasmonic community recently, which is the magneto-optical Kerr effect (MOKE). The technique is commonly used for the characterization of the magnetic properties of thin layers, but obviously plasmons also interact strongly with magnetic fields, which implies that magnetic fields could be used as an additional degree of freedom in the design of magneto-plasmonic applications. It was already shown that symmetrical non-magnetic gold nanoparticles also show magneto-optical activity when exposed to magnetic fields, and by introducing symmetry breaking such effects could be greatly enhanced. These effects are studied in the field of chiral metamaterials, where the plasmonic structures are designed in such a way that they can convert the polarization of an incident wave into the desired state, which is a crucial step on the path towards fully integrated optical chips.

And as we wind on down the road
Our shadows taller than our soul
There walks a lady we all know
Who shines white light and wants to show
How everything still turns to gold
And if you listen very hard
The tune will come to you at last
When all are one and one is all
To be a rock and not to roll...

- Jimmy Page -